Diffraction Studies of Ordered Phases and Phase Transitions

Kjær, Kristian

Publication date:
1984

Document Version
Publisher's PDF, also known as Version of record

RISØ

Risø-R-506

Diffraction Studies of Ordered Phases and Phase Transitions

K. Kjær

Risø National Laboratory, DK-4000 Roskilde, Denmark
August 1984

RISØ-R-506

DIFFRACTION STUDIES OF ORDERED PHASES AND PHASE TRANSITIONS:

A synchrotron x-ray scattering study of monolayers of CF_4 adsorbed on graphite

and

A neutron scattering study of the diluted uniaxial dipolar coupled ferromagnets $LiTb_{.3}Y_{.7}F_4$ and $LiHo_{.3}Y_{.7}F_4$

K. Kjær

Abstract. Two investigations are reported here. First, monolayers of CF_4 physisorbed on the (001) face of graphite have been studied by means of x-ray diffraction experiments carried out at the electron storage ring DORIS in HAMBURG. The exfoliated graphite substrate UCAR-ZYX was used in order to obtain a large area for adsorption and hence a large sample. Four two-dimensional solid phases of the CF_4 films were seen, including a structure which is 2×2 commensurate relative to the substrate. On compression (by variation of coverage or temperature), this phase transforms to a uniaxially compressed structure ("stripe" phase). Further, at higher coverages a hexagonal structure was seen, incommensurate relative to the substrate, and at low temperatures and coverages, a complicated structure emerged, giving three

(Continued on next page)

August 1984
Risø National Laboratory, DK 4000 Roskilde, Denmark

close diffraction peaks in the powder pattern. Data are presented characterizing the meltings and commensurate to incommensurate transitions.

Complementary to the synchrotron x-ray data, a presentation of the theory of synchrotron radiation is given.

The second investigation was of the ferromagnetic phase transitions in the randomly diluted, dipolar coupled uniaxial ferromagnets $LiTb_{.3}Y_{.7}F_4$ and $LiHo_{.3}Y_{.7}F_4$ by neutron diffraction at the RISØ DR 3 reactor. Crystals were grown, the expected (Scheelite) structure was confirmed and the structural parameters were refined for the Tb compound on the basis of a neutron diffraction structural study. Mounted in a ^3He-^4He dilution refrigerator, the crystals were cooled to their Curie points of 0.49 and 0.36K for the Tb and the Ho compound, respectively. Just above the phase transition, the critical neutron scattering of either crystal exhibits the asymmetry characteristic of a dipolar coupled uniaxial ferromagnet; however, an anomaly appears at low momentum transfers for the Tb compound only. Further, data are presented for the magnetic Bragg scattering of both crystals.

This report has been submitted to Danmarks Tekniske Højskole (The Technical University of Denmark) in partial fulfilment of the requirements for obtaining the degree lic. techn. (Ph.D.).

ISBN 87-550-1016-4
ISSN 0106-2840

Risø Repro 1984

CONTENTS

Page

1. INTRODUCTION

1.1. Motivation

For the order (positional order, magnetic (spin) order etc.) obtained in condensed matter systems, the concept of spatial dimensionality is of considerable importance. In general, this is so because the dimensionality determines the amount of phase space available to long-wavelength, low-energy fluctuations which tend to destroy the order. This was realised by Peierls, Landau and others, who proved that the positional order in a two-dimensional harmonic crystal is unstable against destruction by long-wavelength phonons (Ref. 1.1). At the higher dimensionality of three, such a model is stable. This is the general effect: A lowering of the dimensionality eventually destroys the order.

For condensed matter systems of sufficiently high dimensionality to attain long ranged order, the next question concerns the manner in which this order disappears when the temperature is raised, i.e. the nature of the phase transition from the ordered to the disordered state. Here, too, the dimensionality is observed to play an important part: The critical exponents, describing the singular variation of thermodynamic quantities near a phase transition, are observed to depend not on the details of the interactions in the system, but only on its dimensionality and a few other general properties (notably the symmetry of the system) (ref. 1.2).

1.2. Diffraction experiments

X-ray and neutron scattering (or diffraction) experiments are two very useful techniques for investigating questions such as those mentioned above. X-rays are scattered strongly by electrons, and therefore, an x-ray scattering experiment gives the

Fourier-transformed electronic pair correlation function and, by inference, the correlation function of the atoms. Thus, the range and general nature of the positional atomic order can be measured. Thermal neutrons by their interaction with the nuclei can provide the same information, but in addition the neutrons interact with (electronic) magnetic moments, so that the magnetic (spin-) correlation function can be measured.

1.3. Systems

The work reported below has been on two classes of systems which can be thought of as representing opposite extremes of spatial dimensionality (D). Also, the complementary diffraction techniques described above were used. Here, only a brief introduction to each is given, and the details are deferred till later.

Chapter two concerns the low-D limit and describes experiments on monolayers of CF_4 gas physisorbed on the (001) face of a graphite substrate. The layers can be thought of as two-dimensional systems. X-ray diffraction was used to determine the 2D positional order of the CF_4 molecules.

The x-ray source was the electron storage ring DORIS at Deutches Electronen Synchrotron (DESY), Hamburg. (A presentation of the theory of synchrotron x-ray radiation is given in Appendix A of this report).

Chapter three describes magnetic neutron scattering measurements carried out at the RISØ DR 3 reactor. The systems investigated were crystals of the Rare Earth Scheelite family. These are tetragonal crystals containing magnetic Rare Earth ions (formula $LiRF_4$, where R = Rare Earth). When the Rare Earth is Terbium or Holmium, ferromagnetic ordering of the Rare Earth spins occurs at low temperature, due to the magnetic dipolar interaction between the spins. As explained in Chapter three, insofar as the critical phenomena at the ferromagnetic phase transition are concerned, the systems can be thought of as simulating four spatial dimensions! (The systems are at upper marginal dimen-

sionality). In the crystals investigated here, the magnetic ions were randomly diluted by replacement by non-magnetic Yttrium ions, leading to the formulae $LiTb_{.3}Y_{.7}F_4$ and $LiHo_{.3}Y_{.7}F_4$. These systems, then, are random magnets at marginal dimensionality.

References

1.1. See: IMRY, Y. (1978) CRC Crit. Rev. Solid State Mater. Sci. 8, 157-74.
and
VILLAIN, J. (1980) in: "Ordering in strongly fluctuating condensed matter systems. Edited by T. Riste (Plenum Press, New York) p. 222 (Nato Advanced Study Institutes Series: Series B, Physics, 50)
and
NELSON, D.R. and HALPERIN, B.I. (1979). Phys. Rev. B: Condens Matter 19, 2457-84
and
references quoted in these papers.

1.2. See: Phase transitions and critical phenomena (1976). Edited by DOMB, C, and GREEN, M.S. (Academic Press, New York).

2. MONOLAYERS OF CF_4 PHYSISORBED ON GRAPHITE

By means of x-ray diffraction, monolayers of CF_4 physisorbed on the 001 face of graphite were studied. The exfoliated graphite substrate UCAR-ZYX afforded a large total area for adsorption. Use of a diffractometer at the electron storage ring DORIS enabled the collection of a large amount of diffraction data at adequate resolution.

Several two-dimensionally crystalline phases of the CF_4 films were seen, including a commensurate 2 × 2 structure. On variation of temperature or coverage this phase experienced a uniaxial compression, thus transforming to a so-called striped structure. At higher coverages an isotropic, compressed phase was seen, and at low temperature and coverages a complicated structure giving three close diffraction peaks appeared. The characterization of these phases and their meltings and other phase transitions was aided by analyzing the observed diffraction response in terms of simple calculated line shapes.

2.1. Introduction

2.1.1. Theories of two-dimensional systems

Two- (and one-) dimensional condensed matter systems are attractive to thecrists for two reasons: Firstly, they are often easier to handle than their higher-dimensional analogues, and secondly new, exciting phenomena are predicted. A celebrated case in point is the "Ising" model of one-dimensional spins on a square lattice which was solved exactly[2.19], and for which a state of true long-range spin order is found below a second-order transition with non-classical critical exponents.

For other two-dimensional (2D) systems, absence of true long-range order (LRO) is predicted. Most interesting here is the

case of a 2D harmonic solid, for which a state of "quasi LRO" is predicted[2.7], in which the usual Bragg reflections of diffraction experiments i.e. delta function terms in the scattering function $S(Q)$, where $\vec{Q}$ is the scattering vector are replaced by algebraic singularities at low-order reciprocal lattice points,

$$S(\vec{Q}) \propto |\vec{G}_{hk} - \vec{Q}|^{-2+\eta_G} \quad , \quad \eta_G \propto |\vec{G}_{hk}|^2 \ .$$

Other interesting phenomena include second-order melting of this "quasi LRO" solid, and a resulting "hexatic liquid" with exponential decay of positional order, yet still a quasi-long-ranged orientational order[2.7].

2.1.2. Gases physisorbed on the (001) face of graphite

The above-mentioned predictions make real 2D systems very interesting for experiments, although such systems aren't easy to come by. Experimentally accessible systems include single crystal surfaces, thin layers adsorbed there upon, and thin, freely suspended films of liquid crystals.

Among the adsorbate-on-a-substrate systems, gases physisorbed on the (001) face of graphite are quite attractive for a number of reasons. The adsorption potentials for inert gases and among simple molecular gases are of the -100K order of magnitude, allowing reversible ad- and desorption at convenient temperature. Moreover, several exfoliated graphites are available, including Graphoil[2.20] and UCAR-ZYX[2.20]. These offer a large area for adsorption (30, resp. 3 m^2/gram substrate)[2.21]. Their main difference is the size of coherently diffracting 2D crystallites, which is about 110 Å[2.20] for Grafoil and about 1600 Å[2.20,2.5] for ZYX.

An interesting feature of the (exfoliated) graphite substrate is that adsorption takes place layer by layer. This is illustrated (for CF_4) in Fig. 2.1.

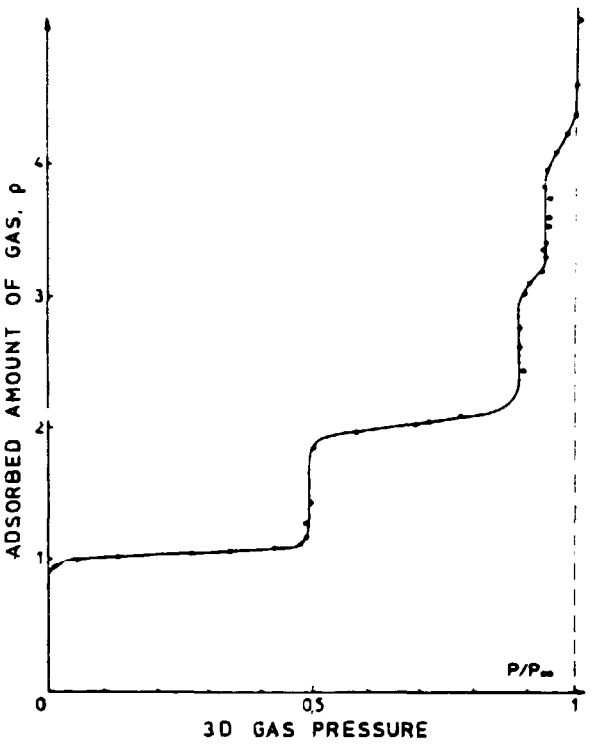

Fig. 2.1. Isotherm of CF_4 adsorbed on exfoliated graphite, reproduced from Ref. 2.17. The graph shows the adsorbed amount of gas ρ versus the equilibrium pressure of the three-dimensional gas phase (normalized by the bulk vapour pressure P_∞), at 77.3 K. The step-like character of the curve reflects the adsorption layer by layer. Four layers can be distinguished here. The amount of gas is given relative to the amount needed to complete the first layer, and the pressure is normalized by the pressure for equilibrium with infinitely many layers, i.e., with bulk CF_4.

This means that by adsorbing the right amount of gas one can prepare a sample consisting of one layer, or a fraction of one complete layer.

The graphite substrate thus makes a two-dimensional experiment possible by confining the adsorbate to a 2D geometry. At the same time, forces from the adsorbate may prejudice the 2D charac-

ter of the adsorbed gas system. Clearly, gas atoms strongly chemisorbed onto specific sites on (say) a metal surface have poor 2D properties, so far as their translational degrees of freedom are concerned. The graphite surface, however, exerts sufficiently weak forces parallel to the surface, that incommensurate 2D solid phases, 2D liquids and 2D dilute gas phases are observed in diffraction experiments on Ar, Kr, Xe, CH_4, N_2 and other gases physisorbed on exfoliated graphite substrates[2.21]. As an added bonus, when the natural lattice constant of the adsorbate comes sufficiently close to a repetition length of the graphite, lock-in or incommensurate-to-commensurate transitions occur.

Hexagonal Incommensurate phases

When the adsorbate's equlibrium lattice constant shows a sufficiently large misfit, relative to that of the substrate, a Hexagonal Incommensurate (HI) solid 2D phase will result. This is the case for Ar[2.1,2.30] and Xe[2.8,2.22], and for Kr[2.23,2.24], CH_4[2.25] and N_2[2.26] at suitable coverages and temperatures. For these not too small misfits, the lateral forces from the substrate will average out. Thus, the HI phases can be considered good approximations to truly 2D solids, so that these phases and their melting transitions can be studied.

Commensurate phases

When the natural lattice constant of the adsorbate is (nearly) commensurate with that of the (001) graphite surface, an epitaxial or commensurate structure will result, in which the adsorbate is in registry with the substrate. Such phases have been observed for Kr[2.27], N_2[2.26] and CH_4[2.25] (the $\sqrt{3} \times \sqrt{3}$ R 30° structure) and for CF_4 (2 × 2 R 0° structure) (Ref. 2.13 and this work). The CF_4 commensurate structure is illustrated in Fig. 2.2.

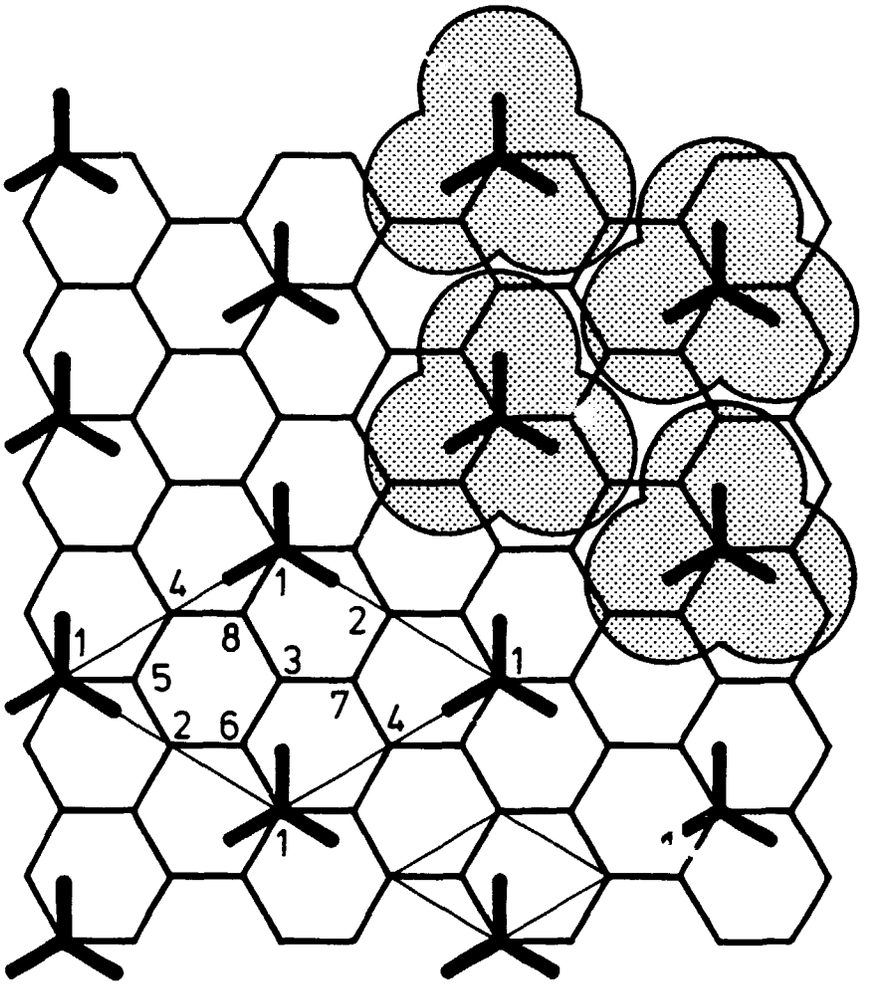

Fig. 2.2. Commensurate 2 × 2 structure as deduced for CF_4 physisorbed on graphite. Every vertex of the hexagon network represents a carbon atom in the top layer of a graphite (001) surface. The clover leaves and the tristars represent the projection of the tetrahedral molecules. Outlined are the unit cells of the 2 × 2 structure and (smaller cell) of the graphite lattice (1 × 1 structure). As shown, there are eight adsorption sites (1-8) within a 2 × 2 unit cell (i.e., eight sublattices).

These commensurate structures will inherit long-range positional order (LRO) from the 3-dimensional substrate and can therefore not be considered as 2D crystals in the sense of having continuous symmetry translational degrees of freedom.

Commensurate to incommensurate transitions

When the adsorbate's natural lattice constant is varied away from the commensurate value (i.e., by variation of coverage or temperature), competing forces will be acting on the adsorbate, namely: 1) the periodic potential from the substrate, which favours a commensurate structure, and 2) the adsorbate-adsorbate interactions, which favour a homogeneous, incommensurate structure. When the latter forces become sufficiently strong, a commensurate-to-incommensurate (C-I) transition will occur. Figure 2.3 depicts (in reciprocal space and for the case of a compressed incommensurate structure) the three "normal modes" of this distortion: An isotropic compression, and uniaxial compressions along two different symmetry axes. The uniaxial modes were not seen in experiments for a long time, but have recently been observed in N_2 layers (Ref. 2.10) and CF_4 layers (this work).

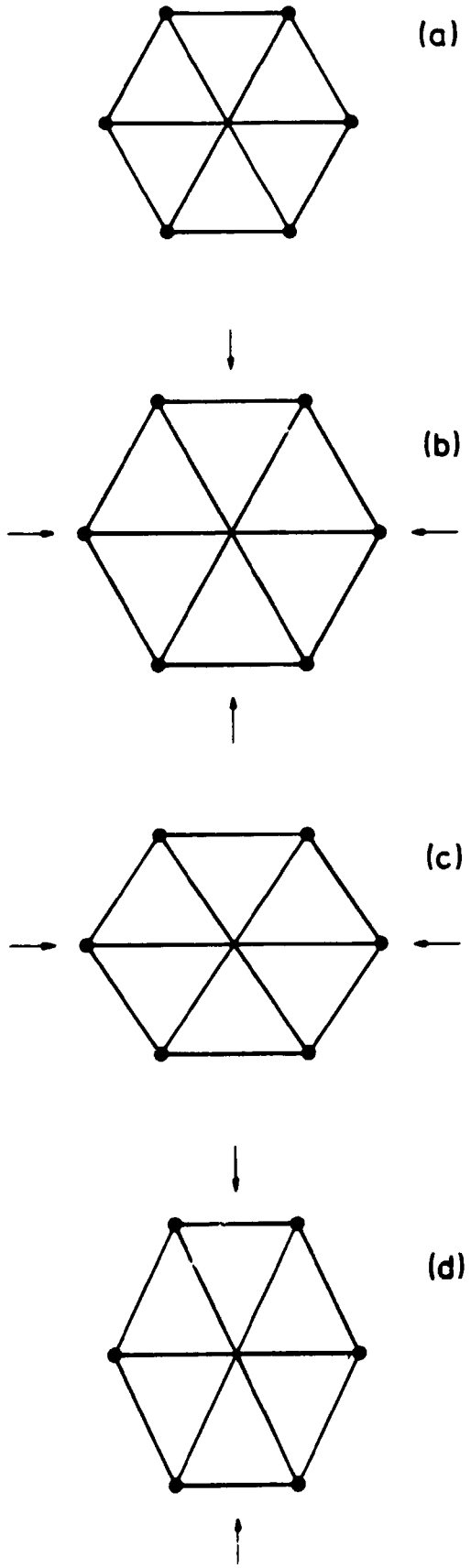
(a)
(b)
(c)
(d)

Fig. 2.3. Reciprocal lattices of commensurate and incommensurate adsorbed structures.

a: Commensurate structure, e.g., 2 × 2 or $\sqrt{3} \times \sqrt{3}$ structure.

b-d: Simple compressed structures, relative to (a).

b: Hexagonal incommensurate structure. Note that all the six low-order reciprocal lattice vectors have the same length.
This type of structure has been observed in layers of Kr, CH_4 and CF_4.

c: Uniaxially compressed structure, as observed in N_2 layers. Four low-order Bragg points are at a scattering angle slightly larger than that for the commensurate structure (a), and the remaining two are four times further away.

d: Uniaxially compressed structure, strain axis 30° from that in (c). (c) and (d) exhaust the uniaxial deformations (along symmetry directions) of a hexagonal structure. In (d), there are two reciprocal lattice vectors orthogonal to the strain direction. Their lengths are therefore unchanged in the compression. The remaining four low-order reciprocal lattice vectors are stretched, however. This type of structure has been observed in CF_4 layers on graphite (this work; "stripe phase").

Domains

In the incommensurate phase, near a C-I transition, the two competing interactions (substrate-adsorbate and adsorbate-adsorbate) will be of comparable strength. To analyze this situation, imagine however that the periodic potential from the substrate is turned off: A homogenous, incommensurate 2D adsorbate crystal will result. When the substrate potential perturbs this equilibrium state, the most economical response will be for the most of the particles to move towards the nearest minimum of the potential, thereby forming domains of locally nearly commensurate structure, while the excess particles (for a denser incommensurate phase) are accommodated in domain walls where the density is substantially higher. At the other end of the scale, i.e. if the periodic potential is assumed to be dominant, perfectly commensurate domains would result separated by walls of very high density. This line of reasoning is illustrated in Fig. 2.8a on page 49 below.

Thus, the concepts of domains and domain walls are central to the physics of C-I transitions[2.7,2.28,2.29].

Further away from the C-I transition, the "domains" will be quite small, and the width of the "domain walls" will extend right through the "domain". Thus, the domain concept loses its significance here, and the substrate potential plays only a minor role in the physics of the incommensurate phase, since it averages out even on a rather fine-grained scale (averaging over few neighbouring particles).

2.1.3. CF_4 physisorbed on graphite

Nitrogen and Argon on graphite were the first systems to be investigated by (neutron) diffraction experiments[2.26,2.30], followed by Kr, Xe and CH_4. These systems all were found to have the $\sqrt{3} \times \sqrt{3}$ commensurate structure, and/or nearby hexagonal incommensurate structures. The discovery (Ref. 2.13) that monolayers of the larger CF_4 molecules have a 2×2 commensurate phase made this system an obvious candidate for one with new

phenomena, and a synchrotron x-ray scattering study was performed. As reported below, this was rewarded by the discovery of a very rich phase diagram, including the first observed uniaxially incommensurate phase (case (d) in Fig. 2.3 above; soon afterwards, the complementary mode of distortion, case (c), was observed to be effective in N_2 monolayers[2.10].

The rest of this chapter is organized as follows: 2.2 reports on the experimental method, results and discussion are in 2.3 which includes two earlier published reports, and 2.4 concludes the chapter on CF_4 monolayers on graphite. Furthermore, Appendix A reviews the theory of synchrotron, wiggler and undulator radiation.

2.2. Experimental procedure

The data were taken with an x-ray diffractometer at the electron storage ring DORIS at DESY, Hamburg. As the properties of synchrotron radiation are reviewed in some detail in Appendix A, it is sufficient to recall here that the electrons, when accelerated in a bending magnet of the storage ring, emit an intense electromagnetic radiation, the spectrum extending well into the x-ray region. The machine parameters were 3.3 GeV and (on average average) 50 mA. With an electron orbit radius of 12.12 m, this yields a critical wave length of 1.88 Å. The diffractometer was situated 20 m from the source. It is shown in Fig. 2.4. At the selected wave length, λ = 1.76 Å, the calculated flux at the entrance slit A1 is about $2 \cdot 10^9$ photons per second per square millimeter per 10^{-4} relative bandwidth $\Delta\lambda/\lambda$.

As described in Refs. 2.1 and 2.2, the slit A1 (4 mm) defines the white beam that impinges on the monochromator, consisting of two parallel Germanium (111) crystals M and M. The crystals were actually offset about 1 millidegree from parallel; this suppresses 3rd and higher orders of the beam while still transmitting most of the 1st-order intensity. After the sample S in the cryostat, the slit A2 (1 mm) and a position-sensitive x-ray detector (PSD) a distance L2 = 550 mm away, define the direction

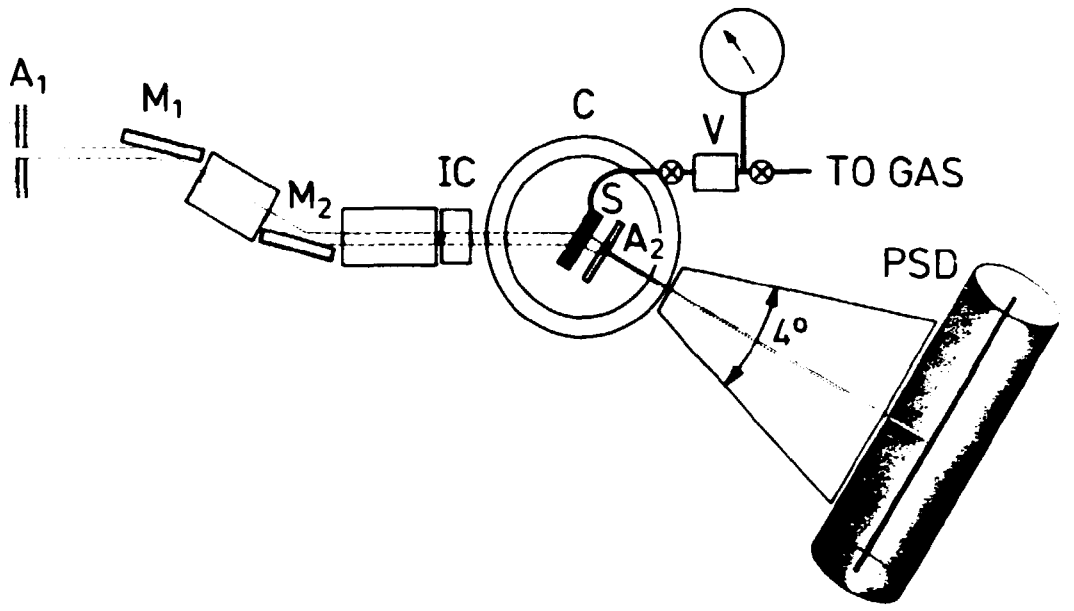

Fig. 2.4. Top view of the x-ray diffractometer.

of scattered rays. The PSD signal was analyzed by a multi-channel analyzer into channels of 0.35 mm each. (It's intrinsic resolution is better than 0.1 mm)

At λ = 1.76 Å, this yields a resolution FWHM ($4\pi \sin\theta/\lambda$) = 0.0064 $Å^{-1}$, in good agreement with observed values. The contribution from the aberrations in the monochromator to this width is negligible. This resolution was chosen to match the coherence length of the ZYX substrate approximately.

The sample cell S has beryllium windows and is mounted in a Displex cooler, C, also with Be windows. Thus, temperatures down to 10 K were accessible. Via a capillary the cell is connected to the gas-handling system which as shown includes a barometer and the standard volume V. Further shown in the figure are evaluated beam tubes and an ionisation chamber used for monitoring the monochromatic beam intensity.

The average (001) direction of the ZYX substrate was vertical, i.e. orthogonal to the scattering plane.

2.3. Results and discussion

This paragraph is organized as follows: First come reprints of the previously published papers: Phys. Rev. B 26, 5168 (1982), which was the first account of this work to appear, and Surf. Sci. 125, 171 (1983), a contribution to the "2nd Trieste International Symposium on the Statistical Mechanics of Adsorption", Trieste, 26-29 July (1982). Then some further analyses follow.

This method of presentation will necessarily result in some repetitions, with which the reader must be asked to bear.

2.3.1. Published papers

PHYSICAL REVIEW B VOLUME 26, NUMBER 9 1 NOVEMBER 1982

Monolayers of CF_4 adsorbed on graphite, studied by synchrotron x-ray diffraction

K. Kjaer, M. Nielsen, and J. Bohr
Risø National Laboratory, DK-4000 Roskilde, Denmark

H. J. Lauter
Institut Laue-Langevin, 156X, 38042 Grenoble Cedex, France

J. P. McTague
Brookhaven National Laboratory, Upton, New York 11973
(Received 6 May 1982)

With synchrotron x-ray diffraction we have measured the phase diagram of CF_4 monolayers adsorbed on the graphite substrate UCAR-ZYX. We have found four two-dimensional crystalline phases including the 2×2 commensurate structure. Between this and the denser incommensurate hexagonal phase we find an axially compressed phase interpreted to be the stripe domain structure. Our data indicate that the order-disorder transition (melting) of the 2×2 commensurate phase as well as melting of the stripe and of the hexagonal incommensurate phases are continuous.

INTRODUCTION

Physisorbed monolayers on graphite of rare-gas atoms or of simple molecules have been studied extensively in recent years with the main purpose of describing the nature of phase transitions in two-dimensional systems. The transitions studied in most detail are melting of the incommensurate free-floating solid [Ar (Ref. 1) and Xe (Ref. 2) monolayers], order-disorder transition (melting) of the commensurate $\sqrt{3}\times\sqrt{3}$ structure [Kr (Ref. 3) and He (Ref. 4) monolayers], and the commensurate-incommensurate (C-I) transition [Kr,[5] H_2, and He (Ref. 6) monolayers]. We report here on diffraction studies on monolayers of CF_4 adsorbed on the graphite substrate UCAR-ZYX.

The CF_4 layers on graphite constitute a fundamentally different system from that of the rare-gas monolayers because of two factors. First, the adsorbed particles are larger and thus commensuration occurs at the 2×2 structure instead of at the denser $\sqrt{3}\times\sqrt{3}$ structure. Second, the preferred adsorption site is assumed to be above the vertex points of the graphite honeycomb structure, which have a symmetry different from that of the center positions taken up by the rare-gas commensurate layers, but similar to that of oxygen atoms chemisorbed on Ni(111) surfaces.[7]

Figure 1 shows the honeycomb structure of the (0002) graphite surface and the CF_4 molecules in the commensurate 2×2 structure. They are shown with a three-fluorine plane parallel to the graphite surface and the projections of the Lennard-Jones spheres of the fluorines are shown shaded. At the temperatures where the 2×2 structure exists, the molecules will have large-amplitude rotational oscillations. In the figure the lowest-energy configura-

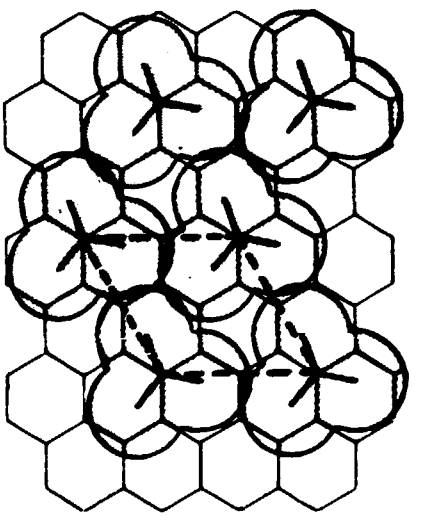

FIG. 1. Schematic arrangement of the CF_4 molecules on the (0002) surface of graphite, in the 2×2 commensurate structure. They are shown by the projection (shaded) of the Lennard-Jones spheres of the fluorines (using the diameter of neon: $2^{1/6}\sigma = 3.17$ Å) assuming that the molecules have a three-fluorine plane parallel to the substrate and are located above the vertex points. Molecules are rotated away from the high-symmetry orientations. Broken line shows the unit cell of the 2×2 structure.

tion is shown as estimated from the potentials of Ref. 8. The molecules are rotated away from a symmetric orientation by the interaction with the substrate. Within the unit cell of the 2×2 structure (Fig. 1), there are four equivalent adsorption sites per molecule and four more sites connected with the former by a 180° rotation. Further, the above-mentioned rotation may be chosen clockwise or counterclockwise. Therefore, the order-disorder transition of the 2×2 structure is different from the three-state Potts transition[4] applying for the $\sqrt{3}\times\sqrt{3}$ phase and is to be described by a Heisenberg model with cubic anisotropy or by an Ising model.[9] For the (C-I) transition between the 2×2 structure and the denser incommensurate hexagonal structure, the different symmetry has the following implication: If a hexagonal structure existed with a layer density a little above the commensurate density, this would give a superstructure of domains[10] in which the domain walls form triangles instead of hexagons as for the slightly incommensurate Kr layers.[11] A triangular superstructure would in the crossing points of the domain walls have six walls meeting, and this would involve a high wall-crossing energy. According to Ref. 12 this favors the alternative domain configuration, the stripe structure, in which the domain walls are parallel lines with no walls crossing. The latter model is found to describe our results, and this is the first observation of the stripe structure in monolayers adsorbed on graphite. The existence of this phase allows us to study the following transitions: commensurate 2×2 to stripe structure, stripe to incommensurate hexagonal structure, and melting of the stripe phase into an isotropic fluid.

The measurements were done with an x-ray spectrometer at the storage ring DORIS at Deutsches Elektronen-Synchrotron (DESY) in Hamburg. The instrument is described in Ref. 13 and consists of a monochromator with two parallel Ge(111) crystals and a position sensitive detector as analyzer. The graphite substrate is a stack of UCAR-ZYX strips contained in an all metal sample cell with Be windows, and the cell was mounted in a Displex cryostat.

PHASE DIAGRAM

The diffraction from the CF_4 monolayers was measured exclusively in the region near the (10) reflection of the 2×2 structure. At the higher-order reflections the intensity was insufficient to obtain useful groups. Data were taken as function of temperature and CF_4 coverage, and Fig. 2 shows the derived phase diagram. At coverage less than 0.79 (we use as unit of coverage the amount of gas which would give one ideal and completed monolayer with the 2×2 structure), we observe triple-point behavior between dilute gas (G), liquid (L), and commensurate 2×2 phase (C). The gas-liquid coexistence line is drawn in accordance with the critical point taken from Ref. 14. With decreasing temperature the coexisting gas plus the 2×2 phase go into the coexisting gas plus stripe (S) phase at 65 K. Below 57 K coexistence between gas and a "three-peak structure" ($3P$) is observed. The nature of this three-peak structure is not interpreted and will not be discussed further here.[15] The stripe structure is observed in a rather broad region around the 2×2 phase, and at higher layer density the hexagonal incommensurate structure (I) was found. The nature of the phase transitions between the different phases is indicated by either single lines (continuous transitions) or by shaded coexistence regions (first-order transitions). However, the phase diagram is tentative and several ambiguities remain. In the diffraction data there is no distinct difference between the

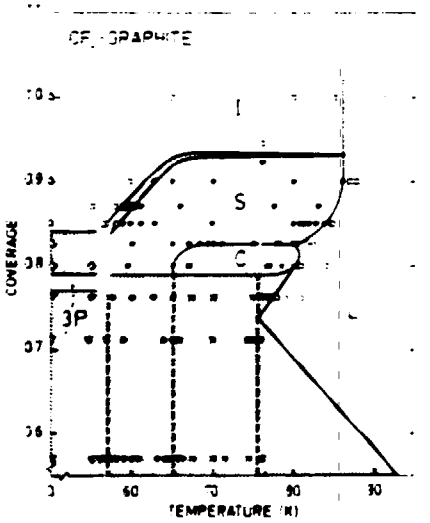

FIG. 2. Phase diagram of CF_4 on (0002) graphite. C, S, I, and $3P$ denote the 2×2 commensurate, stripe, hexagonal incommensurate, and three-peak structures, and L represents a two-dimensional liquid. Full lines indicate phase boundaries and broken lines show transitions of solid phases in coexistence with the dilute-gas phase (not shown in the figure). Coexistence regions are shaded. Points denote diffraction measurements in the following sense: ○, liquid, ×, single 2×2 peak at 1.475 Å^{-1}, ●, two peaks with 1:2 intensity ratio, □ one peak at $Q > 1.475$ Å^{-1}, ▽, three peaks, ◇, four peaks (coexistence of $3P$ and I).

gas plus homogenous solid (say 2×2 phase) and the homogenous solid phases, and thus the corresponding phase lines are uncertain. A very noticeable effect is that the homogenous 2×2 structure is not found at the coverage 1 but rather near 0.8. This must imply that the 2×2 phase contains a high concentration of vacancies or a nonideal behavior of the substrate. The total substrate surface area was determined before and after the measurements by measuring Ar vapor-pressure isotherms at $T=65$ K, and reference to diffraction measurements on Kr monolayers using the same sample cell.[16] The Ar isotherms give a practical check on the area of adsorption on an uncalibrated scale. The absolute scale of the area was determined in more complicated measurements where a series of diffraction scans are measured at low temperature for adsorbed monolayers of Kr with increasing coverage. The sharp onset of the commensurate-to-incommensurate phase transition defines the coverage giving the $\sqrt{3}\times\sqrt{3}$ monolayer.

In the region where three of the phases in Fig. 2, I, S, and $3P$, come together, the phase diagram is not known, but a pronounced first-order transition is observed from $3P$ to I and from I to S.

Figure 3 shows the position of the observed Bragg peaks as function of temperature for three different coverages. The signature of the C phase is a single peak at the position $Q=1.475$ Å^{-1} which is half the (10) reciprocal-lattice vector of the graphite honeycomb structure. The stripe structure is characterized by two peaks, and the distance between them is a measure of the axial compression. Our conjecture that the S phase of Fig. 2 has the stripe structure[12] rests on the following observations: When we move out of the 2×2 region either by decreasing the temperature or by increasing the coverage, we observe that the single (10) reflection of the 2×2 structure splits into a double peak such that the low-Q component remains at the commensurate position $Q=1.475$ Å^{-1}, and the other one moves to slightly higher Q values. There is a constant ratio of 1:2 between the intensity of the two peaks, the low-Q component being the smallest. The distance between the peaks is a continuous function of temperature and coverage. This is explained by an axial compression of the structure or a corresponding expansion of the reciprocal lattice as is shown in the upper part of Fig. 3. The diffraction from an ideal stripe structure comprises extra peaks (satellites) on both sides of the doublet described above. These are due to the periodic density modulation associated with the difference of layer density in the middle of the domains and in the domain walls.[16] However, if the walls are very broad, the satellite intensity is weak. We have not observed any such satellites.

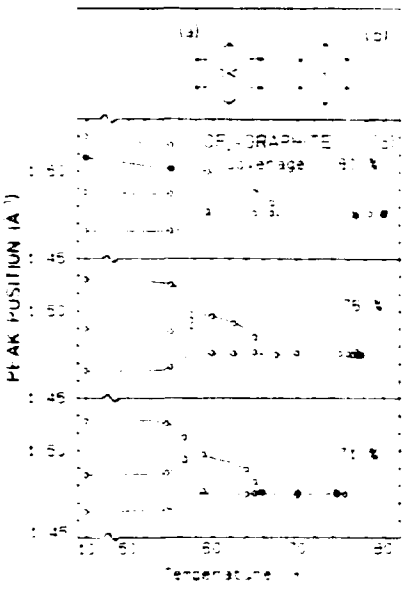

FIG. 3. (a) Points and dashed lines: reciprocal lattice of the uniaxially compressed (stripe) structure. (No satellite reflection points are shown.) Full lines: reciprocal lattice of the 2×2 structure. (b) Reciprocal lattice of the 2×2 structure. (c) Peak positions vs temperature for three different coverages. In the upper panel, the filled circles represent the signal from the I phase coexisting with the three-peak structure. Lines are guides to the eye.

When the temperature is lowered through 57 K at coverages less than 0.76 the double peak of the stripe phase changes into three peaks. Very close to the transition the diffraction response gets broad, and we cannot conclude whether this transition is of first or second order. The positions of the three peaks are $Q=1.465$, 1.486, and 1.518 Å^{-1}, and these as well as the transition temperature are independent of coverage in the solid plus gas coexistence regime. At coverage 0.8 the $3P$ structure coexists with the incommensurate hexagonal phase observed at higher density. The latter component gives a single peak, in the upper panel of Fig. 3 at $Q=1.502-1.508$ Å^{-1}. The nature of the $3P$ phase has recently been discussed on the basis of neutron scattering results,[15] however, more information is needed to conclude on the structure of this phase.

Figure 4 shows the intensity of the (10) Bragg peak of the 2×2 phase at four different coverages. Below the liquid point at the triple-point line, at a coverage 0.74, the intensity of the (10) peak disap-

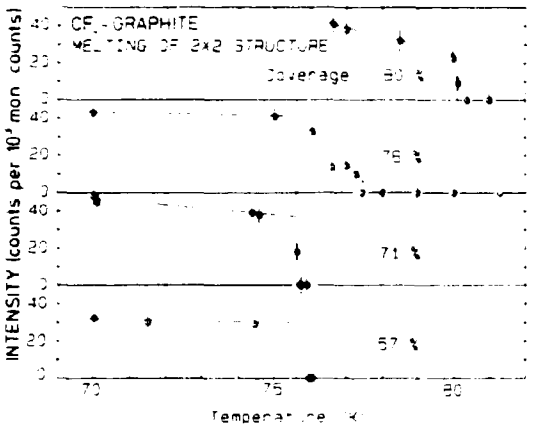

FIG. 4. Peak intensity of the 2×2 reflection at 1.475 $Å^{-1}$ vs temperature at four different coverages. All the diffraction groups represented in the figure had the resolution width of the instrument, corresponding to a coherence length of $L > 1100$ Å. From above, the panels show melting of the homogenous 2×2 phase, "pressure-broadened" decrease of 2×2 intensity due to coexistence with a dense liquid, and (lower two panels) sharp triple-point transition from 2×2 plus dilute-gas coexistence to liquid plus gas coexistence.

pears discontinuously at the triple point. For coverage 0.76 the intensity decreases gradually as we go through the liquid plus solid coexistence region. However, at the triple point there should be an abrupt decrease of intensity as we go from solid plus gas coexistence to solid plus liquid coexistence. Thus the liquid plus solid region of Fig. 2 may be incorrectly indicated, but further measurements are needed to solve this problem. The upper panel of Fig. 4 shows that at coverage 0.80 the 2×2 phase has a very sharp melting transition: The intensity disappears within 0.1 K. This transition is analogous to the melting of the commensurate $\sqrt{3}\times\sqrt{3}$ phase of Kr on graphite described by the three-state Potts model with a continuous transition. For CF_4 monolayers the symmetry is different as discussed above, and it would be of particular interest to study the melting by diffraction in the same detail as has been done for Kr.[3] It should be noted that the phase diagram of Fig. 2 shows that the transition changes over from first order to second order with increasing coverage, and this is analogous to what was found for Kr on graphite[3] and discussed theoretically in Ref. 17.

At higher coverages first the C phase changes into the stripe phase, the melting of which is discussed in the next section, and then the dense incommensurate hexagonal structure is formed. Melting of the latter was studied in a constant coverage scan at $\rho=1.0$. A set of (10) diffraction groups typical for a continuous melting transition was observed. Above the melting temperature T_M the groups broaden. They can be fitted by powder-averaged Lorenzian functions[1,2] with correlation lengths ξ which ideally should diverge at T_M but in practice are limited by finite-size effects. We find that ξ varies from $\xi > 1200$ Å below T_M, a limit set by our instrumental resolution, to $\xi = 170$ Å at 6 K above T_M. This is a much slower variation than observed for Xe and Ar films[2,1] on the same substrate, but more studies are necessary before this can be interpreted.

The phase diagram of CF_4 on graphite has earlier been studied by neutron diffraction.[15] The result was different from ours reported here, due to the lower resolution of the neutron scattering technique. In particular the stripe phase was not seen. Also low-energy electron diffraction measurements have been performed on this system.[18] The 2×2 structure was identified and around 60 K a rotated slightly incommensurate structure was observed. The latter observation is difficult to combine with our interpretation.

PHASE TRANSITIONS INVOLVING THE STRIPE PHASE

Two transitions involving the stripe phase, S in Fig. 2, were studied in detail, namely C to S and S to L. Figure 5 shows some observed diffraction groups near the (10) reflection of the 2×2 structure when we go from C to S by changing temperature at constant coverage near the top of the C-phase region in the phase diagram. In the upper panel, at $T = 80.01$ K, we have the typical single group of the 2×2 structure at $Q = 1.475$ $Å^{-1}$ with the Warren line shape.[6] The full line is the fitted diffraction profile with a Gaussian coherence length[6] of $L = 1100$ Å, which is determined by the spectrometer resolution. Presumably the intrinsic coherence length of the 2×2 structure is longer, and given by the ZYX substrate to be $L \sim 1600$ Å.[13] When we go through the C-to-S transition, the double peak of the S phase develops in a continuous way. Clearly the groups in Fig. 5 at 74.96 or 70 K cannot be constructed as coexistence groups between the upper-panel group and one of the others. The full lines are fitted curves assuming a uniaxial compression of the monolayers in the direction shown in the upper panel of Fig. 3. The integrated intensities of the two peaks have the ratio 1:2. The position of

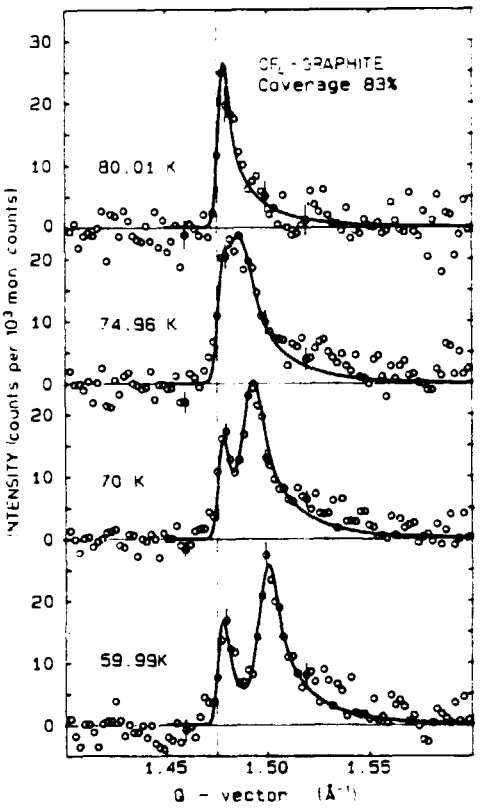

FIG. 5. Measured diffraction intensities (circles) and fitted line shapes (full lines) at constant coverage for four different temperatures. Upper panel: single 2×2 peak of resolution limited coherence length $L=1100$ Å. Lower three panels: double peaks in 1:2 integrated intensity ratio, characteristic of the stripe phase. Left peak has $L_1=1100$ Å and right peak has L_2 (fitted) $=500-600$ Å. Gaussian cross sections have been used in the Warren (Ref. 6) formula for both peaks for simplicity.

the low-Q component is fixed at $Q=1.475$ Å^{-1}, and the high-Q component is shifted outwards according to the increasing compression as T is lowered. For the group at $T=74.96$ K, which is very close to the transition, this shift is $\Delta Q=0.0073$ Å^{-1} corresponding to an axial strain of $\epsilon=0.0066$ or a domain wall separation of 40 lattice distances which is ~200 Å. In the calculation of the curves fitted to the double groups of Fig. 5 we have assumed that the low-Q component has the same Warren line shape as the group of the pure 2×2 structure with $L=1100$ Å. For the high-Q component we also used, for simplicity, the Warren line shape, but let the Gaussian coherence length vary, and best fits were obtained with $L=600$ Å. In fact, different types of line shapes are expected for the two components if the uniaxial compression does not alter the range of coherence of the two-dimensional (2D) crystal in the direction perpendicular to the strain while fluctuations of the local-strain amplitude limit the correlation length in the parallel direction. The statistical accuracy of our data points does not allow a detailed analysis of line shapes, but in principle the groups describe the type of fluctuation existing in the S phase.[19,20]

The phase transition $C\rightarrow S$ was studied in a series of scans for coverages between $\rho=0.57$ and 0.83, and the same behavior as that of Fig. 5 was observed. This also applies for $\rho\lesssim0.79$, where the phase transition occurs with the solid coexisting with a dilute gas. Thus the driving mechanism for this transition is of a different kind from that operative in the commensurate-incommensurate transition of Kr, where a considerable spreading pressure is needed.[13] However, CD_4 monolayers on graphite undergo the transition from $\sqrt{3}\times\sqrt{3}$ to a more dilute incommensurate hexagonal structure at $T\simeq50$ K, also in a phase coexisting with its dilute gas.[21] This transition is thus analogous to the C-to-S transition of the CF_4 layers in the sense that it is the change of the amplitudes of the thermal oscillations of the molecules which drives the change of phase. An important factor must be the molecular rotations, and it would be of particular interest to study this by nuclear magnetic resonance. It should also be noted that the relatively high concentration of vacancies in the solid phases may be an important factor for the transition.

Although the observed diffraction groups near the C-to-S transition rather clearly indicate a continuous phase transition, there can of course be a small not resolved discontinuity of the order parameter in the transition. The separation ΔQ of the two groups of the S phase varies in our data from $\Delta Q=0.03$ Å^{-1} to $\Delta Q=0.006$ Å^{-1}, the smallest value we can resolve. An indication that there may be a small first-order jump is that we saw a small hysteresis when a set of groups like those of Fig. 5 was measured with increasing and decreasing temperature. This could be as large as 1 K but many groups would be needed for a precise determination of the hysteresis. Hysteresis of the C-to-S transition has been discussed theoretically in Ref. 10 and may in fact not *require* a first-order transition.

As shown in Fig. 2 the stripe phase for a range of densities melts into a liquid. This raises the following question: How can the uniaxially compressed S phase transform into an isotropic fluid? Figure 6 shows a constant coverage scan through the melting transition. The general feature seems to be that the double peak of the S phase gradually becomes a single, broad, liquidlike group by both the high- and

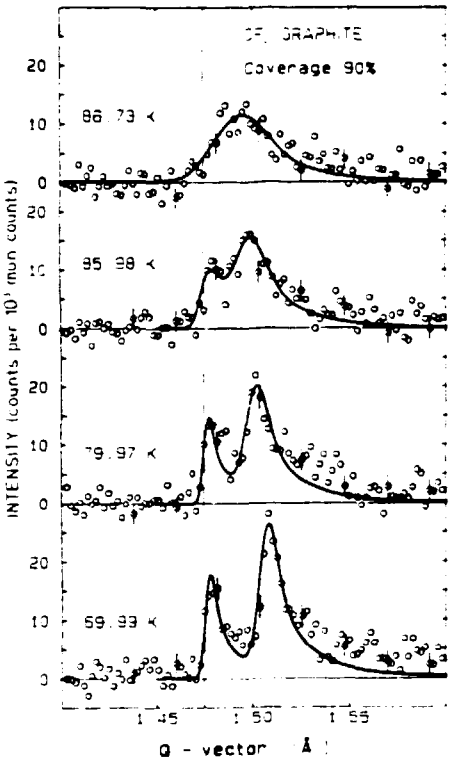

FIG. 6. Constant coverage scan through the melting transition of the stripe phase. Circles: measured intensities. Lines: fitted curves. Upper panel: single broad peak fitted by a Gaussian Warren line shape ($L=200$ Å). (Alternative line shape discussed in text.) Second panel: double peak fitted by two Warren line shapes of coherence lengths $L_1=600$ and $L_2=350$ Å, in 1:2 intensity ratio. Lower two panels: double peak fitted by Gaussian Warren line shapes in 1:2 intensity ratio. Left peak has $L_1=1100$ Å (resolution limited), and right peak has L_2 (fitted) = 500–600 Å.

the low-Q component being broader and broader through the transition. However, the scatter of the data points of the $T=85.98$ K group does not allow a definitive conclusion in this regard. The change of the splitting ΔQ is only a minor effect. The full lines in Fig. 6 show the fitted groups where we again have used Gaussian structure factors in the Warren-line-shape formula for simplicity. As discussed above, the low-Q component of the double group is insensitive to fluctuations in the lattice parameter in the direction of the uniaxial compression, and a correct line-shape calculation should involve an anisotropic and non-Gaussian structure factor around the reciprocal-lattice points of Fig. 3(a). Although the quality of our data does not allow such detailed analysis, they do indicate that when approaching the melting transition, there exist fluctuations in the S phase which change the structure factor in both directions.

We have also fitted the liquidlike scattering profile of the upper panel of Fig. 6, at $T=86.73$ K, to a powder-averaged Lorenzian structure factor.[2] We find that the correlation length is $\xi \simeq 300$ Å, a value similar to what was found in liquid Xe (Ref. 2) and liquid Ar (Ref. 1) near the melting transition between the liquid and an isotropic incommensurate solid with hexagonal structure. As Xe and Ar layers have continuous melting transitions, the intrinsic correlation lengths of the liquids diverge at the melting points, but finite-size effects limit the value and give rise to a "rounding" effect very close to the transition. A value of $\xi=300$ Å is within this rounding regime of the transition. Thus the liquid phase just above the S-to-L melting transition is, within the accuracy of our data, equivalent to the liquid phase of adsorbed Xe or Ar, but it would be of interest to study this with much improved intensity.

Contrary to the two phase transitions described above the transition from stripe to the hexagonal incommensurate phase appeared to be distinctly of first order. In constant coverage scans at $\rho=0.85$ and 0.87 we measured groups in the shaded coexistence region of Fig. 2, which could be constructed as weighted sums of the S- and I-phase signal. We do not have sufficient data to decide whether the coexistence region extends all the way to the melting line as indicated in the tentative phase diagram of Fig. 2. The first order character of the S-to-I transition is theoretically expected.[12]

CONCLUSION

The study of the CF_4 films has shown that they have a rather complicated phase diagram with at least five different phases in the monolayer regime. At present our experimental information about the system is very limited; in particular no measurement or calculation of the rotational state or the position of the adsorbed molecules has been performed. Despite this, diffraction measurements can identify phases already discussed theoretically[12,19] and give important information about the nature of the phase transition between structures with different symmetries. Most significant in our data is the clear evidence that the commensurate-to-incommensurate transtion between the 2×2 structure and the denser hexagonal structure takes place through the intervening uniaxially compressed phase, the stripe domain structure. The C-to-S, the

S-to-L, and the I-to-L transitions are continuous, or at least very weakly of first order if so, whereas S to I and $3P$ to I are of first order. Our diffraction data also give some information about the fluctuations near the continuous phase transitions: It is clear, e.g., that the structure factor near the reciprocal-lattice points of the stripe phase are anisotropic near the C-to-S transition but become more isotropic very near the melting line of the phase diagram. However, a detailed analysis of the functional form of the structure factors requires much higher scattering intensity than was available in our measurements.

ACKNOWLEDGMENTS

The participation of Dr. J. Als-Nielsen in part of the experiment, as well as the invaluable help of our colleagues in the HASYLAB, DESY, Hamburg, is gratefully acknowledged. It is also a pleasure to thank Dr. P. Bak and Dr. E. Riedel for many very fruitful discussions about the interpretation of our data. This work was supported in part by the Danish Natural Science Foundation and by the American National Science Foundation.

[1]J. P. McTague, J. Als-Nielsen, J. Bohr, and M. Nielsen, Phys. Rev. B 25, 7765 (1982).

[2]P. A. Heiney, R. J. Birgeneau, G. S. Brown, P. M. Horn, D. E. Moncton, and P. W. Stephens, Phys. Rev. Lett. 48, 104 (1982); E. M. Hammonds, P. Heiney, P. W. Stephens, R. J. Birgeneau, and P. M. Horn, J. Phys. C 13, L301 (1980).

[3]P. M. Horn, R. J. Birgeneau, P. Heiney, and E. M. Hammonds, Phys. Rev. Lett. 41, 961, (1981); R. J. Birgeneau, G. S. Brown, P. M. Horn, D. E. Moncton, and P. W. Stephens, J. Phys. C 14, L49, (1981).

[4]M. Bretz, Phys. Rev. Lett. 38, 501 (1977).

[5]D. E. Moncton, P. W. Stephens, R. J. Birgeneau, P. M. Horn, and G. S. Brown, Phys. Rev. Lett. 46, 1533 (1981).

[6]M. Nielsen, J. M. McTague, and L. Passell, in *Proceedings of the NATO Advanced Study Institute on Phase Transitions in Surface Films*, edited by J. G. Dash and J. Ruvalds (Plenum, New York, 1980), p. 127.

[7]L. D. Roelofs, A. R. Kortan, T. L. Einstein, and R. L. Park, Phys. Rev. Lett. 46, 1465 (1981); M. Schick, *ibid.* 47, 1347 (1981).

[8]Takako Shinoda, Mol. Cryst. Liq. Cryst. 55, 101 (1979).

[9]E. Riedel and P. Bak (private communication).

[10]P. Bak, in *Solitons and Condensed Matter Physics*, edited by A. R. Bishop and T. Schneider (Springer, Berlin, 1980), p. 216.

[11]The triangular structure of the domain walls follows if the 2×2 structure is slightly compressed isotropically and the adsorbed particles subsequently moved towards the nearest ideal adsorption site. The same procedure applied to the $\sqrt{3}\times\sqrt{3}$ structure results in a honeycomb structure of domain walls.

[12]P. Bak, D. Mukamel, J. Villain, and K. Wentowska, Phys. Rev. B 19, 1610 (1979).

[13]M. Nielsen, J. Als-Nielsen, J. Bohr, and J. P. McTague, Phys. Rev. Lett. 47, 582 (1981).

[14]P. Dolle, M. Matecki, and A. Thomy, Surf. Sci. 91, 271 (1979).

[15]B. Croset, C. Marti, P. Thorel, and H. Lauter (unpublished); H. J. Lauter, B. Croset, C. Marti, P. Thorel, in *Ordering in Two Dimensions*, edited by S. K. Sinha (North-Holland, Amsterdam, 1980), pp. 211–214.

[16]M. Nielsen, J. Als-Nielsen, and J. P. McTague, in *Ordering in Two Dimensions*, edited by S. K. Sinha (North-Holland, Amsterdam, 1980), pp. 135–141.

[17]S. Ostlund and A. N. Berker, Phys. Rev. Lett. 42, 843 (1979).

[18]S. Calisti, Ph.D. thesis, l'Université d'Aix-Marseille II, 1981 (unpublished).

[19]J. Villain, in *Ordering in Strongly Fluctuating Condensed Matter Systems*, edited by T. Riste (Plenum, New York, 1980), p. 221.

[20]V. L. Pokrovsky and A. L. Tapalov, Phys. Rev. Lett. 42, 65 (1979); S. N. Coppersmith, D. S. Fisher, B. I. Halperin, P. A. Lee, and W. F. Brinkman, Phys. Rev. B 25, 349 (1982).

[21]P. Dutta, S. K. Sinha, P. Vora, M. Nielsen, L. Passell, and M. Bretz, in *Ordering in Two Dimensions*, edited by S. K. Sinha (North-Holland, Amsterdam, 1980), pp. 169–174.

Surface Science 125 (1983) 171–180
North-Holland Publishing Company

SYNCHROTRON X-RAY STUDY OF SUB-MONOLAYERS OF CF_4 ON GRAPHITE

K. KJAER, M. NIELSEN and J. BOHR

Risø National Laboratory, DK-4000 Roskilde, Denmark

H.J. LAUTER

Institut Laue-Langevin, 156X, F-38042 Grenoble Cedex, France

and

J.P. McTAGUE

Brookhaven National Laboratory, Upton, Long Island, New York 11973, USA

Received 1 June 1982; accepted for publication 26 July 1982

The quasi-two-dimensional solid and fluid phases of CF_4 physisorbed on the (001) surface of graphite were studied by means of X-ray diffraction at the electron storage ring DORIS, Hamburg. Four crystalline phases were observed, one of which is a registered 2×2 structure. On variation of temperature or coverage, the system experiences a phase transition from the 2×2 structure to a uniaxially compressed or "*stripe*" phase. This is unusual among gas-monolayer systems. Only at higher coverages does an isotropically compressed phase appear. At low temperatures we see a complicated structure giving three closely spaced diffraction peaks. We present diffraction data which characterize the melting of the stripe and the hexagonal incommensurate phases.

1. Introduction

Monolayers of gases adsorbed on graphite are approximately realisations of two-dimensional models of current interest, and, as such, are receiving much interest (see, e.g., refs. [1–6]).

The CF_4 layers are different from the extensively studied rare gas monolayers [1–6] because of two factors. Firstly, the adsorbed particles are larger and thus commensuration occurs at the 2×2 structure instead of at the denser $\sqrt{3} \times \sqrt{3}$ structure. Secondly, assuming that the admolecules have a three-fluorine plane parallel to the substrate, the most plausible adsorption site is above the vertex points of the graphite honeycomb structure, and these have a symmetry different from that of the centre positions taken up by the rare gas commensurate layers [21].

0039-6028/83/0000-0000/$03.00

Concerning the commensurate–incommensurate transition, our results indicate that the (C–I) transition leads from the 2×2 phase to a uniaxially compressed structure in which there must be a superstructure of domains with parallel walls (*stripe structure* [11]). This is the first observation of the stripe structure in monolayers adsorbed on graphite. At higher coverages a hexagonal incommensurate structure is formed. Thus, several new phase transitions may be studied. The choice by the system of this stripe structure may be connected to the symmetry of the adsorption site [21].

2. Experimental technique

The same setup as described in ref. [12] was used. The diffraction data were measured on an X-ray spectrometer installed at the storage ring DORIS at DESY in Hamburg. The monochromator has two parallel Ge(111) crystals. A position sensitive detector is used as analyser. The graphite substrate is a stack of UCAR-ZYX strips contained in an all metal sample cell with Be windows, and the cell was mounted in a Displex cryostat.

3. Phase diagram, stripe phase

Data were taken as function of temperature and CF_4 coverage, and fig. 1 shows the tentative phase diagram. At sub-monolayer coverages a triple point behaviour was observed between dilute gas (G), liquid (L) and commensurate 2×2 phase (C). The gas–liquid coexistence line is drawn in accordance with the critical point taken from ref. [13]. With decreasing temperature the coexisting gas + 2×2 phase go into the coexisting gas + stripe (S) phase at 65 K. Below 57 K coexistence between gas and a "Three-Peak Structure" (3P) is observed. The nature of this "3P Structure" will not be discussed further here [14]. The stripe structure is observed in a rather broad region around the 2×2 phase, and at higher layer density the hexagonal incommensurate structure (I) was found. The nature of the phase transitions between the different phases is indicated by either single lines (continuous transitions) or by shaded coexistence regions (first order transitions). The unit of coverage (ρ) is the amount of gas which would compiete an ideal 2×2 structure. A very noticeable effect is that the homogenous 2×2 structure is not found at the coverage 1 but rather near 0.8. This must imply that the 2×2 phase contains a high concentration of vacancies or a non-ideal behaviour of the substrate. The total substrate surface area was determined before and after the measurements by measuring Ar vapour pressure isotherms and reference to diffraction measurements on Kr monolayers using the same sample cell [12]. In the region where three of the phases in fig. 1, I, S and 3P, come together, the phase diagram is not known.

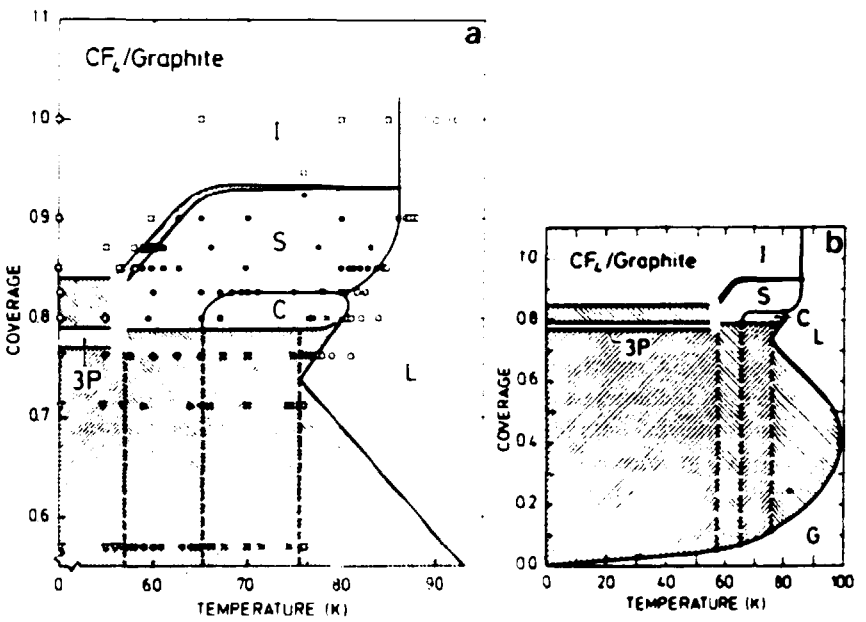

Fig. 1. Phase diagram of CF_4 on (001) graphite. C, S, I and 3P denote the 2×2 commensurate, stripe, hexagonal incommensurate and "three peak" structures, and L represents a two-dimensional liquid. Not shown is the dilute 2D gas at low coverages. Full lines indicate phase boundaries and broken lines show transitions of solid phases in coexistence with the dilute gas phase (not shown in the figure). Coexistence regions are shaded. Points denote diffraction measurements in the following sense: (○) liquid; (×) single 2×2 peak at 1.475 $Å^{-1}$; (●) two peaks with 1 : 2 intensity ratio; (□) one peak at $Q > 1.475$ $Å^{-1}$; (▽) three peaks; (◇) four peaks (coexistence of 3P and I).

but a pronounced first order transition is observed from 3P to I and from I to S.

Fig. 2 shows the position of the observed Bragg peaks as a function of temperature for three different coverages. The signature of the C phase is a single peak at the position $Q = 1.475$ $Å^{-1}$ which is half the (10) reciprocal lattice vector of the graphite honeycomb structure. The stripe structure [11] is characterized by a double peak, and the distance between them is a measure of the uniaxial compression. When we move out of the 2×2 region either by decreasing the temperature or by increasing the coverage, we observe that the single (10) reflection of the 2×2 structure splits into a double peak such that the low Q component remains at the commensurate position $Q = 1.475$ $Å^{-1}$, and the other one moves to slightly higher Q values. There is a constant ratio of 1 : 2 between the intensity of the two peaks, the low Q component being the smallest. The distance between the peaks is a continuous function of tempera-

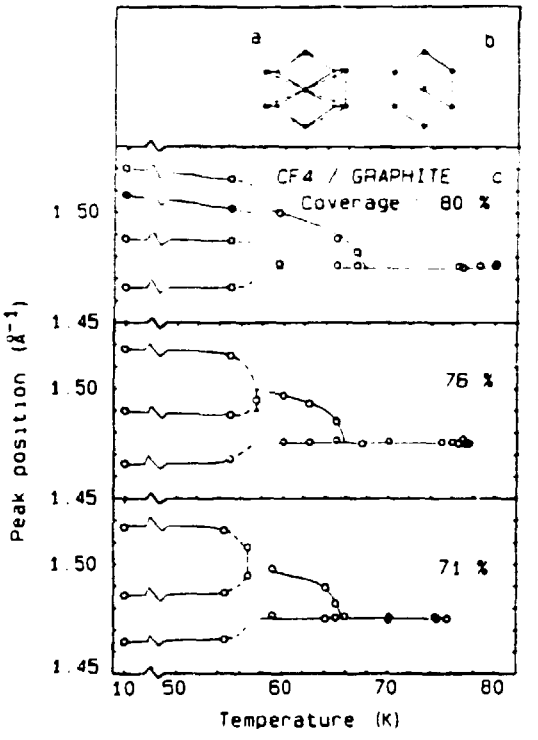

Fig. 2. (a) Points and dashed lines, reciprocal lattice of the uniaxially compressed ("stripe") structure (no satellite reflection points are shown); full lines: reciprocal lattice of the 2×2 structure. (b) Reciprocal lattice of the 2×2 structure. (c) Peak positions versus temperature for three different coverages. In the upper panel, the filled circles represent the signal from the I phase coexisting with the 3P structure. The lines are guides to the eye.

ture and coverage. This is explained by an axial compression of the structure or a corresponding expansion of the reciprocal lattice such as shown in the upper part of fig. 2 [15].

At low coverages ($\rho < 0.76$) and temperatures ($T < 57$ K) we see the three-peak structure. At higher coverages this phase coexists with the hexagonal incommensurate structure, so that four diffraction peaks are observed (fig. 2c, upper panel).

The phase diagram of CF_4 on graphite has earlier been studied by neutron diffraction [14]. The result was different from ours reported here, due to the lower resolution of the neutron scattering technique. In particular the stripe phase was not seen. Also LEED measurements have been performed on this system [17]. The 2×2 structure was identified and around 60 K a rotated slightly incommensurate structure was observed. The latter observation is difficult to combine with our interpretation.

4. Line shape analysis

The peaks from the 2×2 phase are well fitted by a powder-and-tilt averaged Gaussian (Warren line shape [6]) of coherence length $L = 1100$ Å, representing the combined effect of the 1600 Å coherence length of the ZYX substrate [12] and the instrumental resolution. For the liquid, a powder-and-tilt averaged two-dimensional Lorentzian cross section [2] is applicable, and this also fits the peaks from the hexagonal incommensurate (I) structure well. (We shall not discuss here the ideal scattering function of the I phases [1,2].) In our data the coherence length ξ_2 of this two-dimensional Lorentzian varies from 80 Å for the weakest liquid scattering peaks to 1600 Å for the peaks from the I solid. For these peaks, the abovementioned effective Gaussian resolution function also contributes to the width. We have not attempted to deconvolute this contribution. For the stripe phase we assume that the scattering function is anisotropic, being approximately Gaussian in the direction perpendicular to the strain, while fluctuations in the local strain amplitude lead to a *one-dimensional Lorentzian* shape in the parallel direction,

$$S(\bar{Q}_0 + \bar{q}) \propto \exp\left(-\frac{L^2 q_\perp^2}{4\pi}\right) \frac{1}{1 + \xi_\parallel^2 q_\parallel^2},$$

$\bar{Q}_0$ being a Bragg point of the stripe reciprocal lattice. Upon powder-and-tilt averaging, this leads to the abovementioned Warren line shape for the low-Q component of the stripe doublet, while the high-Q peak is approximately described by a tilt-averaged Lorentzian, the powder-averaging being redundant when the Gaussian is narrow compared to the one-dimensional Lorentzian. These line shapes were found to describe the stripe phase doublet quite well.

For the 3P structure it was noticeable that the widths of the three peaks were different.

5. Meltings and other phase transitions

The stripe doublet develops from the single peak of the 2×2 phase in what seems to be a continuous transition [21].

Contrarily, the transition from the stripe to the hexagonal incommensurate structure appeared to be distinctly of first order. The transition takes place through a coexistence region, in which the diffraction signal can be constructed as the weighted sum of the S- and I-phase signals.

The melting of the S phase was studied in constant coverage scans at $\rho = 0.85$ and $\rho = 0.90$. Fig. 3a shows some of the data for coverage $\rho = 0.90$. At low temperatures (lowest panel) we see two peaks of separation $\Delta Q = 0.030$ $Å^{-1}$ corresponding to a strain $\epsilon = 0.027$. As the temperature is raised, the peak separation varies little, but the high-Q peak broadens. Close to the transition

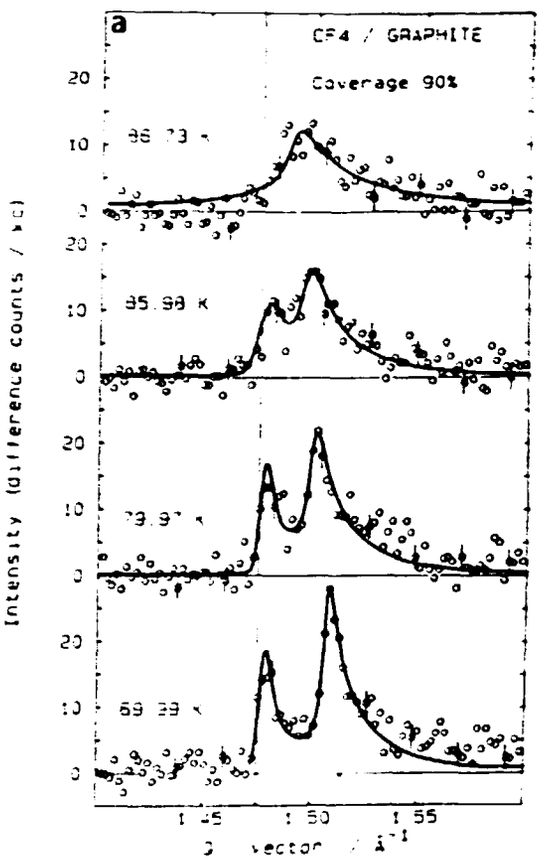

Fig. 3a. Constant coverage scan through the melting transition of the stripe phase: circles, measured intensities, lines, fitted curves (lineshapes discussed in text). Upper panel: single broad peak fitted by a two-dimensional Lorentzian lineshape (ξ_2 = 225 Å). Second panel: double peak fitted by two lineshapes with length parameters L = 600 Å (Gaussian) and ξ_1 = 200 Å (one-dimensional Lorentzian), in 1 : 2 intensity ratio. Lower two panels: double peaks fitted by two lineshapes, Gaussians (resolution limited), L = 1100 Å, and (high-Q peaks) one-dimensional Lorentzian with ξ_1 = 275 and 350 Å.

(T_M = 86 K) the low-Q component experiences some broadening, too. Finally, a single broad peak to the high-Q side of the 2 × 2 peak position emerges and this liquid-like structure factor could be seen in a temperature range of about 1.5 K above the transition. Thus, the transition seems most likely to be continuous. The full lines in the figure are fits of the line shapes described in the previous section: For the liquid, a two-dimensional Lorentzian, and for the solid, a Gaussian and a one-dimensional Lorentzian locked in a 1 : 2 ratio of

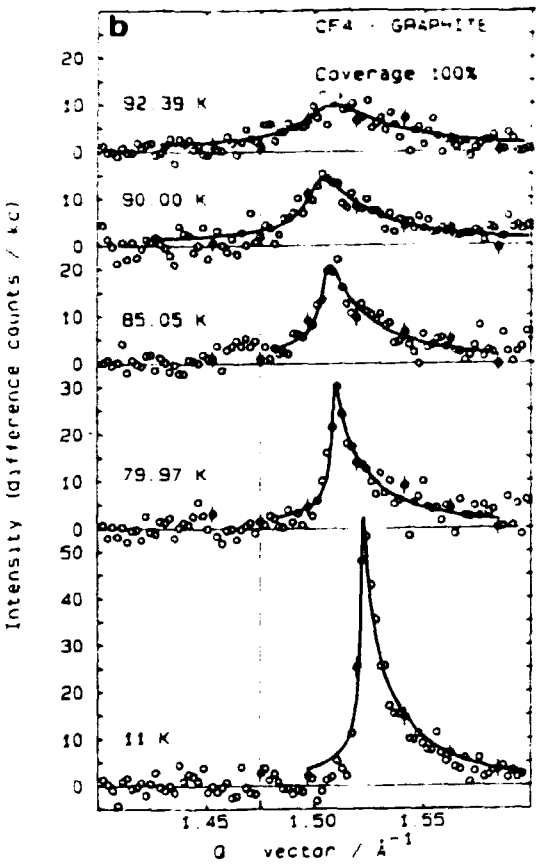

Fig. 3b. Constant coverage scan through the melting of the hexagonal incommensurate phase. For simplicity, all peaks are fitted by (powder-and-tilt averaged) two-dimensional Lorentzians as discussed in text. From above, the correlation lengths are ξ_2 = 110, 200, 400, 1000 and 1600 Å.

integrated intensities, the coherence length of the low-Q peak being fixed at L = 1100 Å except very near the transition. The fitted parameters are represented in panel B of fig. 4.

From a theoretical point of view, there is need of an investigation of possible mechanisms for a continuous freezing transition in which the isotropic liquid transforms to the uniaxial solid, and of the resulting diffraction lineshapes.

For completeness we show data for the melting of the hexagonal incommensurate solid at ρ = 1.00 (fig. 3b). Panel A of fig. 4 shows the continuous variation of peak position, width and intensity through the melting point taken

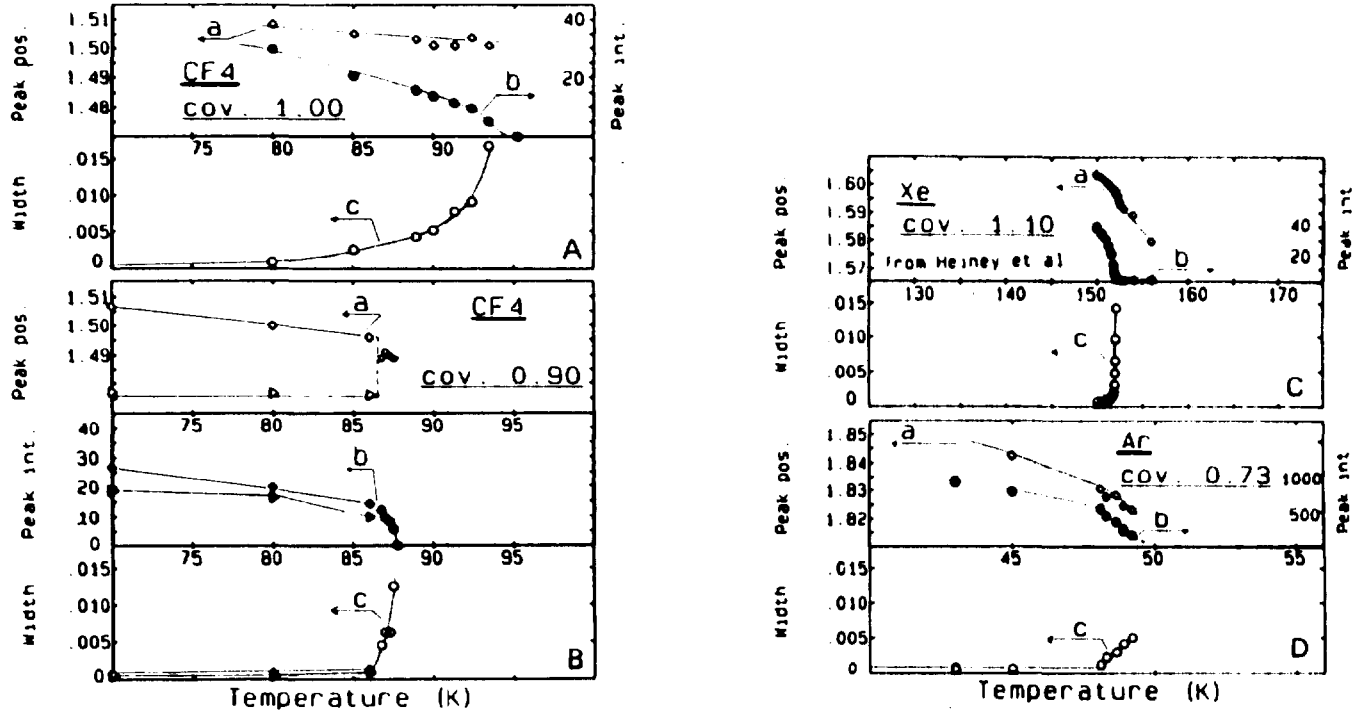

Fig. 4. Comparison of four two-dimensional melting transitions. The horizontal axis is the temperature in kelvins, the scale being chosen so that the reduced temperatures T/T_M are comparable in the four panels. The vertical axes are: (a) peak positions in $Å^{-1}$ units; (b) peak intensity in arbitrary units; (c) width of the diffraction peaks. The panels show the melting transitions of: (A) the hexagonal incommensurate structure of CF_4 on graphite, at coverage $\rho = 1.00$ (particles per *eight* substrate carbon atoms; (B) the CF_4 stripe structure (showing two peaks in solid phase) at coverage 0.90 (particles per *eight* carbon atoms); (C) the hexagonal incommensurate structure of dense monolayers of xenon, at coverage 1.10 (particles per six carbon atoms); (D) the hexagonal incommensurate structure of argon, at coverage 0.73 (per six carbon atoms). The data for the dense xenon layers are reproduced from ref. [2]

to be $T_M = 86$ K, at which point the peaks start to broaden quickly. The peak position varies little, and no distinct feature of this parameter marks the transition. The data indicate that the I to L melting transition of CF_4 is continuous.

Panels C and D of fig. 4 show for comparison the data for two other melting transitions of incommensurate 2D solids on graphite: Dense monolayers of xenon and submonolayers of argon.

Comparing the four transitions, it is apparent that the region of the CF_4 hexagonal incommensurate solid extends over 0.1 in reduced temperature T/T_M, a much wider range than for any of the other films. The dense Xe layers show a very steep decrease of correlation length in the liquid. These differences are not understood.

6. Conclusion

The study of the CF_4 films has shown that they have a rather complicated phase diagram with at least 5 different phases in the monolayer regime. At present our experimental information about the system is very limited, in particular no measurement nor calculation of the rotational state or the position of the adsorbed molecules has been performed. Despite this, diffraction measurements can identify phases already discussed theoretically [11,18] and give important information about the nature of the phase transitions between structures with different symmetries. Most significant in our data is the clear evidence that the commensurate to incommensurate transition between the 2×2 structure and the denser hexagonal structure takes place through the intervening uniaxially compressed phase, the stripe domain structure. The C to S, the S to L and the I to L transitions are continuous, or at least very weakly of first order if so, whereas S to I and 3P to I are of first order. Our diffraction data also give some information about the fluctuations near the continuous phase transitions: The diffraction peaks from the stripe phase could be fitted by line shapes derived by assuming anisotropic fluctuations and structure factors that are anisotropic near the Bragg points. The simple model assumed here can certainly be improved. More detailed measurements of the line shapes would then be needed, requiring much higher intensity than was available in our measurements.

Acknowledgements

The participation of Dr. J. Als-Nielsen in part of the experiment, as well as the invaluable help of our colleagues in the HASYLAB, is grateful acknowledged. It is also a pleasure to thank Drs. P. Bak and E. Riedel for many, very

fruitful discussions about the interpretation of our data. This work was supported in part by the Danish Natural Science Foundation and by the American National Science Foundation.

References

[1] J.P. McTague, J. Als-Nielsen, J. Bohr and M. Nielsen, Phys. Rev., to be published.
[2] P.A. Heiney, R.J. Birgeneau, G.S. Brown, P.M. Horn, D.E. Moncton and P.W. Stephens, Phys. Rev. Letters 48 (1982) 104;
E.M. Hammonds, P. Heiney, P.W. Stephens, R.J. Birgeneau and P.M. Horn, J. Phys. C13 (1980) L301.
[3] P.M. Horn, R.J. Birgeneau, P. Heiney and E.M. Hammonds, Phys. Rev. Letters 41 (1978) 961;
R.J. Birgeneau, G.S. Brown, P.M. Horn, D.E. MOncton and P.W. Stephens, J. Phys. C14 (1981) L49.
[4] M. Bretz, Phys. Rev. Letters 38 (1977) 501.
[5] D.E. Moncton, P.W. Stephens, R.J. Birgeneau, P.M. Horn and G.S. Brown, Phys. Rev. Letters 46 (1981) 1533.
[6] M. Nielsen, J.P. McTague and L. Passell, in: Proc. Nato Advanced Study Institute on Phase Transitions in Surface Films, Ettore Majorana Centre for Scientific Culture, Erice, Italy, 1979 (Plenum, New York) p. 127.
[7] T. Shinoda, Mol. Crystals Liquid Crystals 55 (1979) 101.
[8] E. Riedel and P. Bak, private communication.
[9] P. Bak, in: Solitons and Condensed Matter Physics, Eds. A.R. Bishop and T. Schneider (Springer, Berlin, 1980) p. 216.
[10] The triangular structure of the domain walls follows if the (2×2) structure is slightly compressed isotropically and the adsorbed particles subsequently moved towards the nearest ideal adsorption site. The same procedure applied to the $\sqrt{3} \times \sqrt{3}$ structure results in a honeycomb structure of domain walls.
[11] P. Bak, D. Mukamel, J. Villain and K. Wentowska, Phys. Rev. B19 (1979) 1610.
[12] M. Nielsen, J. Als-Nielsen, J. Bohr and J.P. McTague, Phys. Rev. Letters 47 (1981) 582.
[13] P. Dolle, M. Matecki and A. Thomy, Surface Sci. 91 (1979) 271.
[14] B. Croset, C. Marti, P. Thorel and H. Lauter, to be published.
H.J. Lauter, B. Croset, C. Marti and P. Thorel, in: Ordering in Two Dimensions, Ed. S.K. Sinha (North-Holland, New York, 1980) pp. 211–214.
[15] M. Nielsen, J. Als-Nielsen and J.P. McTague, in: Ordering in Two Dimensions, Ed. S.K. Sinha (North-Holland, New York, 1980) pp. 135–141.
[16] S. Ostlund and A.N. Berker, Phys. Rev. Letters 42 (1979) 843.
[17] S. Calisti, Thesis, Marseille (1981), unpublished.
[18] J. Villain, in: Ordering in Strongly Fluctuating Condensed Matter Systems, Ed. T. Riste (Plenum, New York, 1980) p. 221.
[19] V.L. Pokrovsky and A.L. Talapov, Phys. Rev. Letters 42 (1979) 65;
S.N. Coppersmith, D.S. Fisher, B.I. Halperin, P.A. Lee and W.F. Brinkman, Phys. Rev. B25 (1982) 349.
[20] P. Dutta, S.K. Sinha, P. Vora, M. Nielsen, L. Passell and M. Bretz, in: Ordering in Two Dimensions, Ed. S.K. Sinha (North-Holland, New York, 1980) pp. 169–174.
[21] K. Kjaer, M. Nielsen, J. Bohr, H.J. Lauter and J.P. McTague, Phys. Rev. B, to be published.

2.3.2. Line shape analysis. Warren line shape

In this and the next section we give an account of the line shapes used to analyse the data.

The observed diffraction line shapes are strongly modified by the special nature of the sample, which is a powder of two-dimensional (2D) crystallites, but with some preferred orientation. First, however, we must consider the scattering function of the average crystallite in the powder.

The momentum transfer is $\vec{Q} = \vec{k}_f - \vec{k}_i$, which we resolve in components in the crystallite plane and orthogonal to it, $\vec{Q} = \vec{Q}_h + \vec{Q}_v$. For a large 2D crystal, with long-range positional order (LRO), the scattering function is

$$S_{-}(\vec{Q}) \propto \Sigma_{\vec{G}} |F^2(\vec{Q})| \delta_2(\vec{Q}_h - \vec{G}) \ .$$

Here, F^2 is the structure factor. The sum is over the reciprocal lattice points ($\vec{G}$) of the 2D crystal, and the 2D delta function defines the "Bragg rods" of the 2D crystal. Near a reciprocal lattice point $\vec{G}$ we make the further decomposition $\vec{Q}_h = \vec{Q}_\ell + \vec{Q}_t$, along and across the $\vec{G}$ vector.

For at crystal of finite size L, the delta function is replaced by a $(\sin(Q \cdot L/2)/\sin(Q \cdot a/2))^2$ form where a is the lattic constant. The oscillating tails of this form which corresponds to a sharp cut-off in real space are unrealistic[2.3], and following Warren[2.4] we replace it by a Gaussian

$$S_W(\vec{Q}) \propto \exp\left(- \frac{L^2 \, \Delta Q_h^{\,2}}{4\pi} \right) ,$$

where $\Delta\vec{Q} = \vec{Q} - \vec{G}$. To within 6 per cent, S_W has the same width as the $(\sin(Q \cdot 1/2)/\sin(Q \cdot a/2)^2$ form. It is appropriate for a commensurate crystal (C), with 2D LRO imposed by the substrate. For the ZYX substrate, L = 1600 Å[2.5].

Next, S_W must be averaged over all orientations of the crystallites in the plane, (powder average)

$$\bar{S}_W(\vec{Q}_\ell) = \frac{1}{2\pi} \int_0^{2\pi} d\omega \; S_W \; (Q_\ell \cos\omega, \; Q_\ell \sin\omega)$$

By approximating the circle by a straight line we get

$$\bar{S}_W(\vec{Q}_\ell) \propto \exp\left(- \frac{L^2 \; \Delta Q_\ell^2}{4\pi} \right) .$$

Finally, we must average over the distribution of crystallite normals (tilt average). We take the probability for a crystallite normal deviating the angle θ from the vertical to be $\exp(-\theta^2/w^2)$, with FWHM(θ) = 18 degrees for the ZYX substrate. Following J. Bohr[2.6] we take the angle between a crystallite normal and the momentum transfer $\vec{Q}$ of the diffractometer to be $(\pi/2-\theta_o)$, and further, the azimuth of the normal (around Q) to be ψ, and express the powder- and tilt-averaged intensity as

$$\langle S \rangle (Q) \propto \int_{\theta_o} \int_{\psi} \bar{S}(Q\cos\theta_o) e^{-\theta^2/w^2} d\Omega_{\theta_o \psi} \quad ,$$

where

$$d\Omega_{\theta_o \psi} = \cos\theta_o \; d\theta_o \; d\psi$$

and

$$\cos\theta = \cos\theta_o \; \cos\psi \; .$$

In principle, <S> must finally be convoluted with the resolution function of the instrument as derived in 2.2.

For simplicity, the resolution was, however, accounted for by replacing the true coherence length 1600 Å with the value L_{eff} = 1100 Å.

2.3.3. Other line shapes

For phases other than the commensurate structure, different line shapes are observed and predicted from theories. A simple approximation to this problem is to use an effective coherence length in the Warren line shape. This provides a family of curves with the asymmetry characteristic of the experimental method, and a variable width. (This approach was used for simplicity in the Phys. Rev. paper above).

A more thorough approach is to substitute the appropriate line shape for the delta function in the formulae of Section 2.3.2. For the 2D liquid phase (L), assuming isotropic exponential decay of correlations, a 2D-Lorentzian is in order[2.22],

$$S_{2DL}(\vec{Q}) \propto (1 + \xi_2^2 \, \Delta\vec{Q}_h^2)^{-1} \ ,$$

where ξ_2 is the correlation length. This form must in principle be convoluted with the "Warren" Gaussian describing the finite size; however, when ξ_2 is not too long, this can be ignored. Using the same approximation as before, the powder average leads to

$$\bar{S}_{2Dl}(\vec{Q}_\ell) \propto (1 + \xi_2^2 \, \Delta Q_\ell^2)^{-1/2} \ .$$

For the (hexagonal) incommensurate solid phase (I), algebraic decay of positional order is expected[2.7], leading to

$$S_{\eta\infty}(\vec{Q}) \propto |\Delta\vec{Q}_h|^{-2+\eta_G} \ , \quad \eta_G \propto |\vec{G}|^2$$

This form, appropriate for an infinite crystal, must be convoluted with the finite size function S_W,

$$S_\eta = \int d^2\vec{Q}' \ S_{\eta\infty}(\vec{Q}') \ S_W(\vec{Q}-\vec{Q}') \ .$$

This can be done analytically[2.3].

However, Heiney et al.[2.8] found that their high-quality data for the incommensurate solid phase of xenon on ZYX could be fitted equally well by the above-mentioned Lorentzian and by

S_η. The signal-to-noise ratio in the CF_4 data is not nearly as good, and therefore, the 2D-Lorentzian was used in the further analysis of the I phase of CF_4 for simplicity.

For the stripe phase (S), anisotropic fluctuations are expected, since the adsorbate is commensurate with the substrate in one direction only (namely, the direction orthogonal to the strain ($\perp$)). Thus we are led to the simple ansatz

$$S_S(\vec{Q}) \propto \exp\left(-\frac{L^2\,\Delta\vec{Q}_\perp^2}{4\pi}\right) \cdot \left(1 + \xi_\parallel^2\,\Delta Q_\parallel^2\right)^{-1} ,$$

in terms of wave vector components along the strain ($\parallel$) and orthogonal to it ($\perp$): $\vec{Q}_h = \vec{Q}_\parallel + \vec{Q}_\perp$. The second factor describes of course an assumed exponential decay of correlations in the strain direction, convoluted, in principle, with the finite size function S_w. This function is represented in Fig. 2.5 by the anisotropic ellipses.

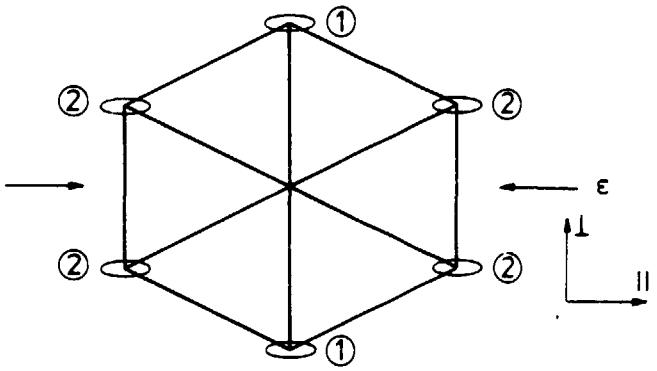

Fig. 2.5. Fluctuations in reciprocal space, for the stripe phase (S) of CF_4. 1) Commensurate reciprocal lattice points. 2) Incommensurate points.

The powder average leads for the commensurate points to

$$\bar{S}_S(\vec{Q}_\ell) \propto \exp\left(-\frac{L^2\,\Delta Q_\ell^2}{4\pi}\right) ,$$

while for the incommensurate points, when the Gaussian is somewhat narrower than the Lorentzian, we get

$$\bar{S}_S(\vec{Q}_\ell) \propto (1 + \xi_1^2 \cdot \frac{4}{3} \Delta Q_\ell^2)^{-1}$$

Thus only the projected width of the 1D Lorentzian, $\sqrt{3/2} \cdot 1/\xi_1$, is seen in the powder scan[2.9].

Sets of curves <S>(Q) were computed, using the formulae in this and the preceding section, for use in fitting the data. A computer program developed by J. Bohr[2.11] was used to perform the tilt average.

The results are summarized in the nomogram, Fig. 2.6.

Examples of the Gaussian line shape $\langle S_W \rangle$ are shown in Figs. 5 and 6 of the Phys. Rev. paper and in Fig. 2.7 below; of the line shape $\langle S_S \rangle$ in Fig. 3a of the Surf. Sci. paper; and of $\langle S_{2DL} \rangle$ in Fig. 3b of the Surf. Sci. paper. While the quality of the data do not allow an unambiguous choice of line shapes, it must be said that the calculated line shapes reproduce the overall features of the data quite well. The I and L phase date were fitted notably better by the 2D Lorentzian $\langle S_{2DL} \rangle$ than by the Gaussian $\langle S_W \rangle$.

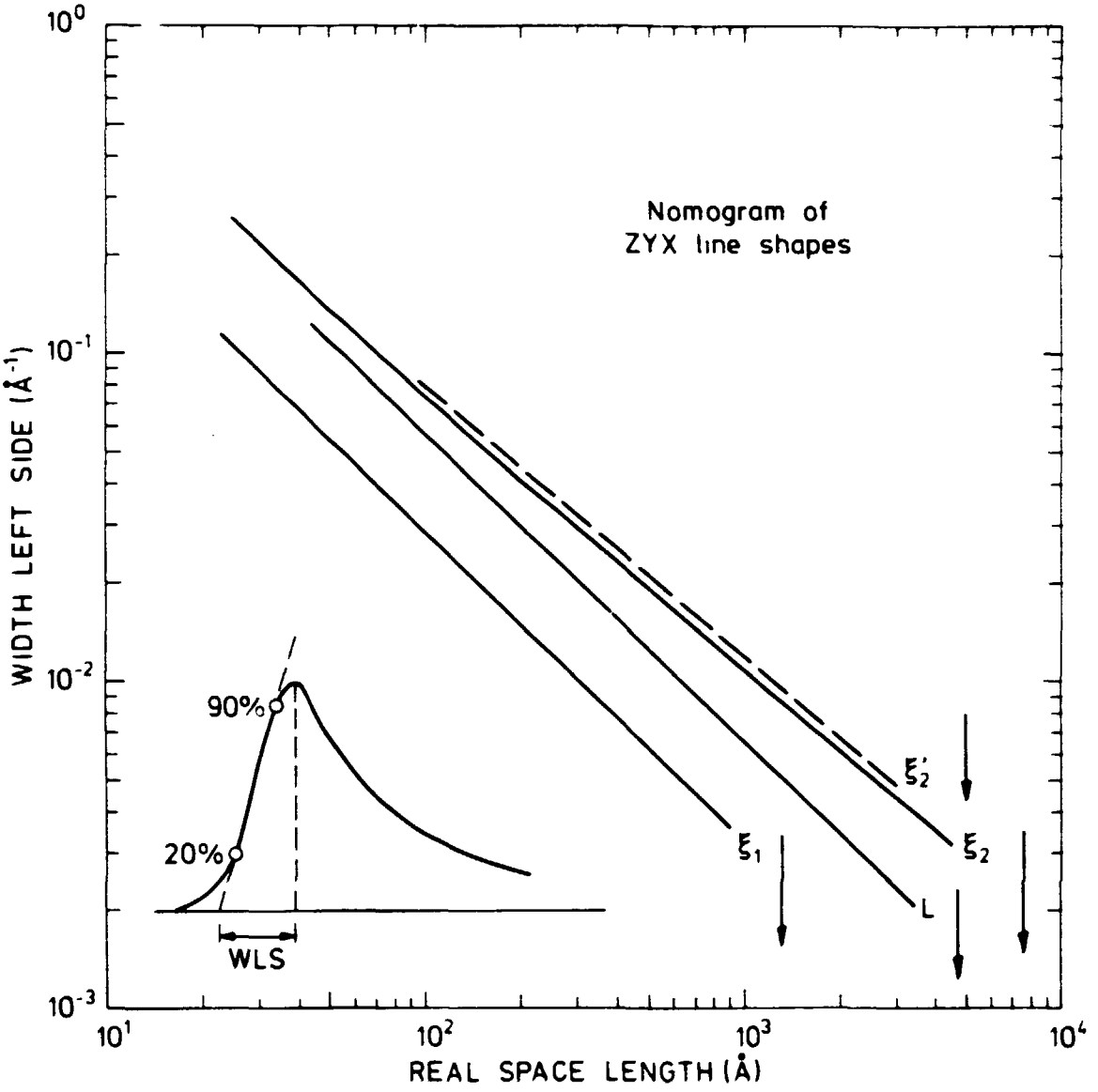
Nomogram of
ZYX line shapes
WIDTH LEFT SIDE (Å⁻¹)
REAL SPACE LENGTH (Å)
10⁰
10⁻¹
10⁻²
10⁻³
10¹
10²
10³
10⁴
90%
20%
WLS
ξ₂'
ξ₂
ξ₁
L

Fig. 2.6. For practical purposes, the asymmetrical lineshapes calculated for gas layers on ZYX graphite can be characterized by their width to the left side (WLS), defined as shown in the insert. The figure shows the WLS as function of the real space length parameters for the various line shapes used:

ξ_1: One-dimensional Lorentzian, $\bar{S}_S(Q_\ell) \propto (1 + \xi_1^2 \Delta Q_\ell^2)^{-1}$. For the stripe phase of CF_4 monolayers the direction of fluctuations is 30° from the incommensurate Bragg vector, and consequently, the ξ_1 must in this case be corrected, i.e., $\xi_1(\text{true}, CF_4) = \sqrt{3/2} \cdot \xi_1(\text{fitted or read from nomogram})$.

The parameters used in the calculation were the lowest reciprocal lattice vector of the (2 × 2) structure, $\tau_o = 1.475$ Å^{-1}, and the (002) mosaic FWHM = 18°.

L: Gaussian describing finite size in an otherwise perfectly long-range ordered 2D crystal;

$$\bar{S}_W(Q_\ell) \propto \exp\left(-\frac{L^2 \Delta Q_\ell^2}{4\pi}\right) .$$

Same parameters.

ξ_2: Two-dimensional Lorentzian, $\bar{S}_{2DL}(Q_\ell) \propto (1 + \xi^2 \Delta Q^2{}_\ell)^{-1/2}$. Same parameters.

ξ_2': Same cross-section as previous, but calculated for $\tau_o = 1.703$ Å^{-1} = $(10)\sqrt{3}\times\sqrt{3}$.

2.3.4. Phase diagram

This section discusses some details of the phase diagram.

C-L coexistence:

As pointed out in the published papers, a discrepancy may exist between the asserted phase diagram and the data at the melting of the commensurate (C) phase: As drawn in Fig. 2 of the Phys. Rev. paper, the phase diagram predicts for the melting at coverage $\rho = 0.76$ a ca. 50% decrease in intensity as the temperature is raised beyond the C-L-G triple point $T_3 = 75.6$ K. This is not borne out by the available data (Fig. 4 of the Phys. Rev. paper). The correction involved may be quantitative (pulling the lower C phase boundary down to $\rho = 0.76 + \varepsilon$ would solve the problem) or qualitative (the topology may be wrong in this corner of the phase diagram), but more data are obviously needed to reach a firm conclusion here.

3P, S, and I phases:

The region of the phase diagram where these three phases meet was left blank in the publications, since no diffraction groups were obtained in that region. By introducing an I-S-3P triple point and an S-3P-G triple point it is possible to connect the phase diagram in a topologically sound way but a large density of diffraction groups would be needed to verify any such hypothesis. Also, good resolution would be required, since interpretation of the diffraction signal from coexisting I + 3P, I + S and S + 3P phases is needed.

One-dimensional liquid:

On the basis of theoretical analysis, P. Bak and T. Bohr[2.12] have proposed several more subtle changes to the phase diagram. For the stripe phase, they predict anisotropic fluctuations, much as outlined in Section 2.3.3: long-ranged order (LRO) (limited only by finite size) parallel to the domain walls, and quasi-LRO (i.e., algebraic decay of correlations) perpendicular to the walls, (along the strain direction). Bak and Bohr also predict the existence of a new phase between the S and L phases and be-

tween the S and C phases. This new phase has exponential decay of correlations in the strain direction, and still LRO in the perpendicular direction. Thus, it is a "one-dimensional liquid". (Bak and Bohr elect to denote it "2 × 1 phase", in view of the discrete translational symmetry arising from the substrate potential).

This means that two of the transitions involving the stripe phase are modified (according to Bak and Bohr) to become:

Melting:

S (with 1D LRO × 1D algebraic decay)
→ "2 × 1" (1D LRO × 1D exponential decay)
→ L (2D exponential decay)

and Incommensurate to Commensurate transition:

S → "2 × 1" → C(2D LRO) .

An experimental test of this hypothesis would involve detailed line-shape studies and would probably be extremely difficult for the latter transition, since we here have the two powder peaks of the stripe phase merging in the transition. While the situation is intrinsically better for the melting, the present data do not warrant such a line-shape analysis (as commented in Section 2.3.3). Qualitatively, the data are probably consistent with the behaviour predicted by Bak and Bohr (see Fig. 3a of the Surf. Sci. paper).

In any case, the apparently continuous melting of the stripe phase is an intriguing transition which could well warrant further detailed study.

Liquid with Ising transition:

Bak and Bohr[2.12] also predict another transition, within the liquid (L) phase. Assuming that, in the I phase, only 4 of the 8 sublattices are populated, they predict that this exclusive occupation will persist into the L phase during the I → L (melting) transition. Then, at a higher temperature, this preferential occupation would disappear in a transition with Ising

symmetry. It seems improbable, however, that this new transition would have much impact on the diffraction signal in a powder scan.

Also, the basic assumption of preferential occupation need not be correct. Indeed, Fig. 2.8a below shows a quite plausible domain structure in the I phase, populating all eight sublattices equally.

2.3.5. Three peak structure

The lowest panel of Fig. 2.7 shows the diffraction response from the 3P structure.

For the 3P group in the figure, the integrated intensity ratio is 15:31:54, and this ratio doesn't vary much with temperature and coverage. Note also the different peak widths, corresponding to 1100, 700 and 500 Å in coherence length.

Several plausible models for the 3P structure present themselves, but must, however, be rejected on closer scrutiny. (See also Ref. 2.13).

Monoclinic cell with one molecule:

Such a structure could of course be adjusted to fit the observed peak positions: 1.466, 1.487 and 1.516 $Å^{-1}$. Then the intensity variation must come from the variation of the CF_4 molecular form factor with orientation. Calculation shows that the form factor varies less than 25% at momentum transfer 1.475 Å in any one plane through the molecule, so this possibility must be discarded.

Domain structure:

We cannot interprete the data as a satellite reflection pattern from some kind of domain structure, simply because the peaks do not index like that. Also, the intensity would seem to be distributed too evenly in this case. Specifically, the calculation summarized in Fig. 2.9 concentrates much more of the intensity in a main peak.

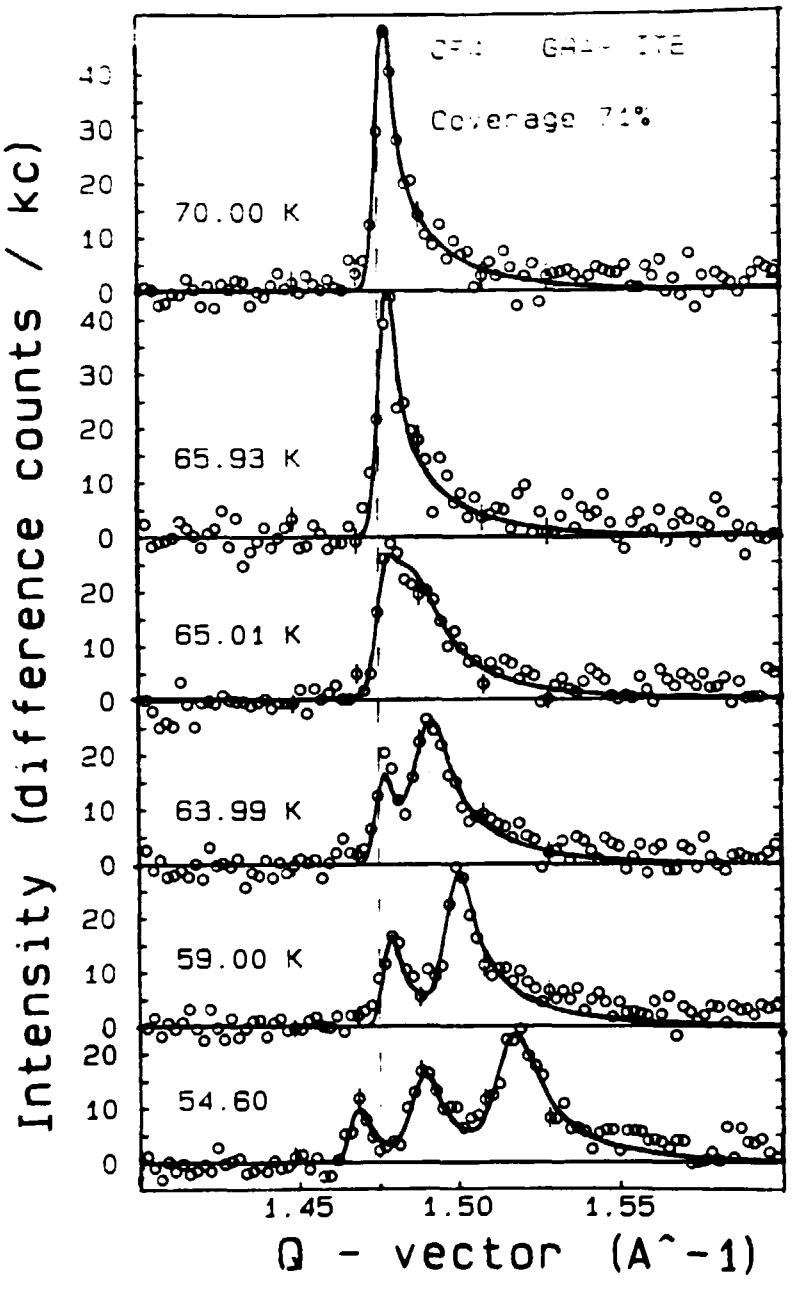

Fig. 2.7. Diffraction groups as a function of temperature for a CF_4 coverage $\rho = 0.71$. With decreasing temperature, first the 2 × 2 structure (upper two panels) changes into the stripe phase (next three panels). Below 56K, the 3P structure appears. Each solid phase coexists with the dilute gas phase at this coverage. The full lines are fits of (Gaussian) Warren line shapes with variable coherence lengths (except for commensurate peaks at 1.475 Å-1, for which L ≡ 1100 Å).

Monoclinic cell with several molecules:
Of course, a model with more degrees of freedom could fit both the intensities and peak positions. A larger unit cell would, however, give rise to new reflections in the powder pattern. Such reflections were looked for, in vain, in a neutron diffraction study by H.J. Lauter et al.[2.13].

Bulk condensation:
For completeness, the observed peak positions were compared with the reported diffraction patterns of powdered 3D CF_4 crystals[2.14]. This allowed the exclusion of the possibility that we were observing a 3D (bulk) condensate of CF_4.

Thus, the riddle of the three peak structure remains unsolved. It is possible that a LEED study could shed some light on the problem, since, by this method, some information about the orientation of the adsorbate relative to the substrate could be obtained.

2.3.6. Satellite reflections

The periodic potential from the substrate must in principle cause a density modulation in the (S and I) incommensurate phases, causing satellite reflections to appear. When the potential is strong, the ground state of an incommensurate phase will consist of domains of locally commensurate configurations, delimited by sharp domain walls. For a weaker potential relative to the adsorbate forces, the domain walls will be broader until, for a compleately flat substrate, a homogeneous incommensurate phase results. We have not observed any satellite reflections in the S or I phases of CF_4 on graphite, so the domain walls must be fairly broad.

This statement can be made more quantitative and simultaneously some general ideas about slightly incommensurate phases[2.15,2.16] can be spelled out more clearly if a specific model of the domain structure is assumed and subjected to calculation.

The domain structure (for the hexagonally incommensurate I phase) illustrated (for the rather large strain $\varepsilon = -0.091$) in

Fig. 2.8a has the following properties: All eight sublattices of the commensurate 2 × 2 structure are populated. The displacement vectors between neighbouring domains are the nearest neighbour vectors between the threefold coordinated adsorption sites. The triangular domain shape reflects the threefold coordination of the sites. The domain size is chosen so that the domains form a superstructure; this is possible for a set of strain values ε which is dense at $\varepsilon = 0$. Two adjacent triangles make up the unit cell and define translation vectors of the superstructure. The reciprocal lattice of this superstructure is illustrated by the (fine) triangular lattice in Fig. 2.8b. This reciprocal lattice results also from a more general argument, also illustrated in Fig. 2.8b, by which the satellite reflection vectors are generated from the mismatch between the substrate reciprocal lattice points (r.l.p.) and the nearest r.l.p. of the adsorbate.

The satellite intensities were calculated for the sharp domain walls shown in Fig. 2.8a and also for various more relaxed walls producing eventually the strain-free incommensurate phase. The specific relaxation illustrated in Fig. 2.9c was assumed. A triangular domain containing $\propto N^2$ particles can be thought of as consisting of $\propto N$ rows of equidistant particles. Since the structure amplitude of a row can be expressed simply, only $\propto N$ terms need be summed numerically for each structure amplitude. These single-crystal structure amplitudes are then normalized by the supercell area, squared, and a sum over terms of equal momentum transfer gives the powder pattern. This method of calculation is similar to the one presented in Ref. 2.18 for the hexagonal domains of the ABC structure.

Results are illustrated in Fig. 2.9a and b for a strain $\varepsilon = -0.048$. Calculations were performed for various strains down to $\varepsilon = 0.0005$, i.e. a very slightly incommensurate structure, and gave qualitatively similar results as a function of the fraction of particles residing in the walls. It is notable that the satellite intensities near the 1.475 $Å^{-1}$ commensurate Bragg position are always less than 15% of the main peak, and that several satellite peaks have comparable intensities. Satellites as intense as those in Fig. 2.9.1 and 2 would probably be recognizable in

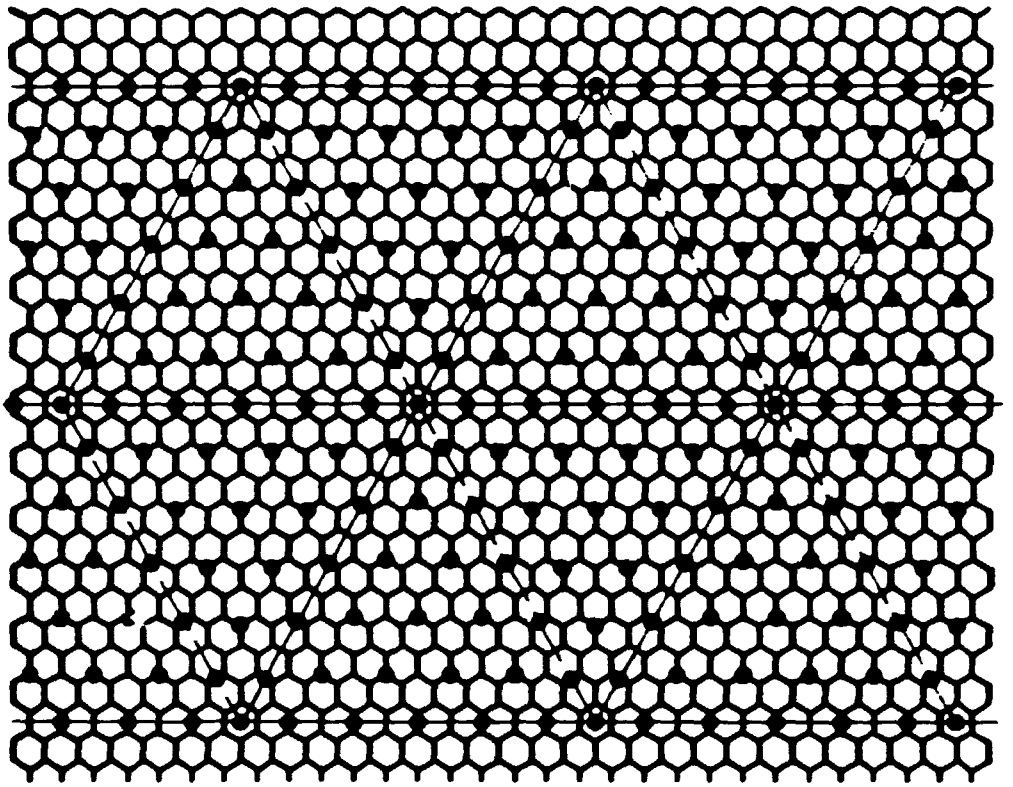

(a)

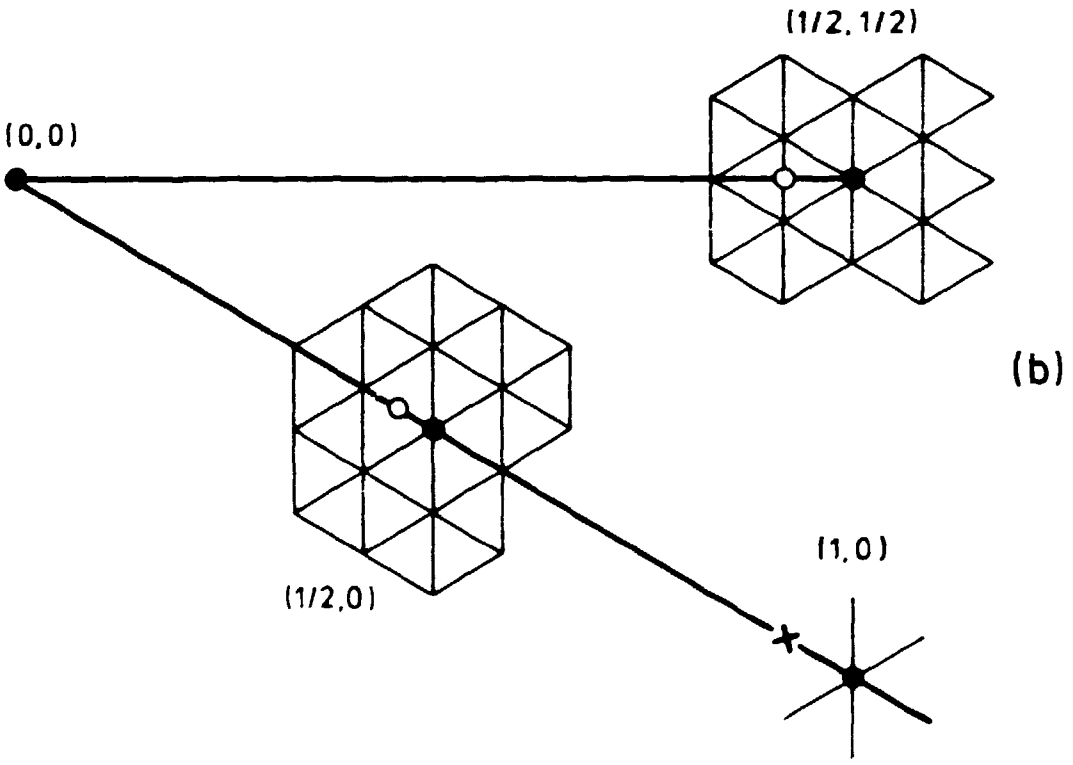

(b)

Fig. 2.8. a) Plausible triangular domain structure of a hexagonal incommensurate solid. The structure is slightly compressed relative to the commensurate 2 × 2 structure and populates all eight sublattices of the 2 × 2 structure. Full and broken lines indicate domain walls. Full lines also show the unit cell of the super lattice of the modulated structure. The nominal density ("x-ray density") of the structure shown is $\rho = 1.19 \approx 1-2\epsilon$.

b) The corresponding reciprocal lattice:
- x, reciprocal lattice point (r.l.p.) of the graphite lattice.
- o, additional r.l.p.s of the 2 × 2 structure.
- •, r.l.p.s. of the compressed structure.

The star of modulation vectors shown near the graphite r.l.p. (x) define the reciprocal lattice of the super structure, i.e., the satellite reflections present near the main r.l.p.s of the compressed structure (•), as shown by the triangular lattice (thin lines).

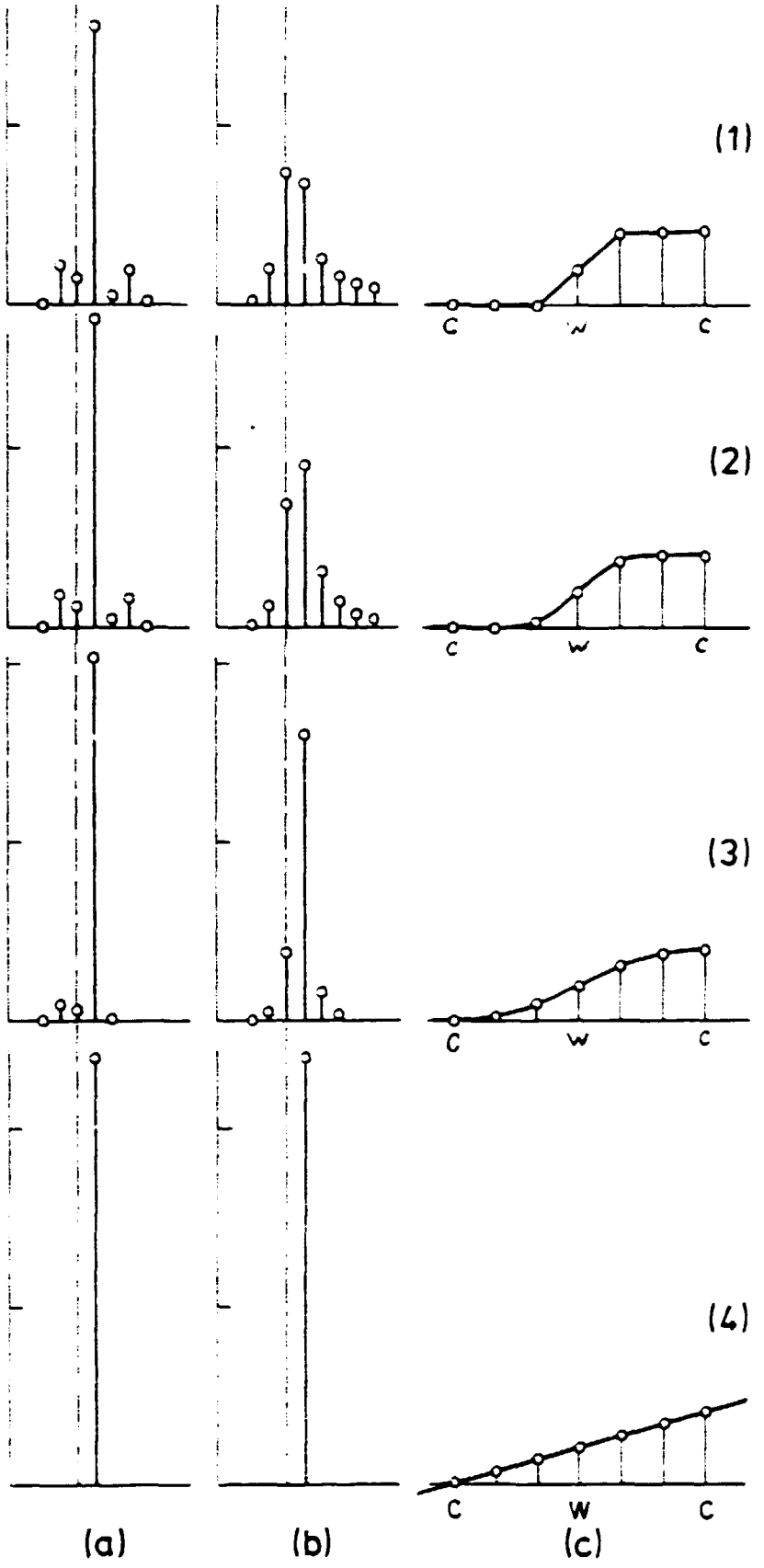
(1)
(2)
(3)
(4)
C
W
C
(a)
(b)
(c)

Fig. 2.9. Calculated powder averaged satellite intensities vs. momentum transfer for a triangular domain structure similar to that shown in Fig. 2.8a. Nominal density ('x-ray density') $\rho = 1.098 = 1-2\varepsilon$.

(a)-(b): Intensities near the reciprocal lattice points. $(10)_{2\times2}$ (1.475 $Å^{-1}$, (a)) and $(11)_{2\times2}$ (2.555 $Å^{-1}$, (b)). --- marks the commensurate reflection position.

(c): Displacements relative to the 2 × 2 structure, versus position along a line from the centre of one domain (C) across the domain wall (W), to the centre of the next domain (C).

(1)-(4): Various relaxations of the domain structure.

(1): Narrow walls as shown in Fig. 2.8a.

(2)-(3): Parabolic relaxation of the displacements away from the wall.

(4): Homogeneously strained adsorbate lattice (corresponding to zero substrate potential), leading of course to zero satellite intensities.

our data, so it may be tentatively concluded that Fig. 2.9.2c is a bound on the sharpness of the domain wall. For the I phase data presented in Fig. 3b of the Surf. Sci. paper, the strain ε varies from -0.031 to -0.020.

2.4. Conclusion

In conclusion, the work reported above has shown that CF_4 monolayers physisorbed on the (001) face of graphite have an interesting phase diagram including in particular the stripe phase which is connected to the commensurate 2 × 2 phase and to the liquid phase by what appears to be second-order phase transitions. Also, the hexagonal incommensurate phase was seen to melt continuously.

Simple line shapes, corrected for the orientation distribution of the substrate, were used to fit the observed diffraction groups.

Some problems remain, e.g., concerning two corners of the phase diagram. Also, a model for the three peak phase has not resulted from this work (nor from the complementary neutron scattering data (Ref. 2.13)).

More information could probably be obtained by detailed line shape studies of the meltings of the incommensurate phases and also of the commensurate to stripe structure transition. This will, however, require a higher flux than was available in the experiments reported here. The wiggler port presently being prepared at the storage ring DORIS[2.31] will improve the situation, making these and many other new experiments possible.

References

2.1. MCTAGUE, J.P., ALS-NIELSEN, J., BOHR, J. and NIELSEN, M. (1982). Phys. Rev. B 25, 7765-72.

2.2. BOHR, J., KJÆR, K., NIELSEN, M. and ALS-NIELSEN, J. (1983). Nucl. Instrum. Methods Phys. Res. 208, 555-58.

2.3. DUTTA, P. and SINHA, S.K. (1981). Phys. Rev. Lett. 47, 50-53.

2.4. WARREN, B.E. (1941). Phys. Rev. 59, 693-98.

2.5. NIELSEN, M., ALS-NIELSEN, J., BOHR, J. and MCTAGUE, J.P. (1981). Phys. Rev. Lett. 47, 582-85.

2.6. BOHR, J. (1984). Synchrotron x-ray diffraction studies of phase transitions in physisorbed monolayers of rare gases on graphite. Risø-R-504, 135 pp.

2.7. See, e.g., VILLAIN, J. (1980) in: "Ordering in strongly fluctuating condensed matter systems. Edited by T. Riste (Plenum Press, New York) p. 222 (Nato Advanced Study Institutes Series: Series B, Physics, 50)
and
NELSON, D.R. and HALPERIN, B.I. (1979) Phys. Rev. B: Condens Matter 19, 2457-84.

2.8. HEINEY, P.A., BIRGENEAU, R.J., BROWN, G.S., HORN, P.M., MONCTON, D.E., and STEPHENS, P.W. (1982). Phys. Rev. Lett. 48, 104-108.

2.9. The uniaxial compression of N_2 on graphite[2.10] is along one of the reciprocal lattice axes, i.e. 30° from the direction for CF_4. Thus, the stripe fluctuations are seen, in the powder scans with N_2, at both types of reciprocal lattice points, the projected widths being $\propto 1/\xi_1$ and $1/2 \cdot 1/\xi_1$, respectively.

2.10. DIEHL, R.D. and FAIN, S.C. (1982). Phys. Rev. B: Condens Matter 26, 4785-88.
and
NIELSEN, M., ALS-NIELSEN J., BOHR, J. and KJÆR, K. unpublished.

2.11. Thanks are due to J. Bohr for the loan of the program and for advice regarding its use.

2.12. BAK, P. and BOHR, T. (1983). Phys. Rev. B: Condens Matter 27, 591-93.

2.13. LAUTER, H.J., CROSET, B., MARTI, C. and THOREL, P. (1980) in: Ordering in two dimensions. Edited by S.K. Sinha (Elsevier. New York) 497 p.
and
CROSET, B., MARTI, C., THOREL, P. and LAUTER, H.J., unpublished.

2.14. BOL'SHUTKIN, D.N., GASAN, V.M., PROKHVATILOV, A.I. and ERENBURG, A.I. (1972). Acta Crystallogr. Sect. B 28, 3542-47.
Note that the y coordinates of F(2) and F(3) are interchanged by mistake in this publication.

2.15. BAK, P. (1978) in: Solitons and condensed matter physics. Edited by A.R. Bishop and T. Schneider (Springer, Berlin) p. 216 and Rep. Progr. Phys. 1982, 45, 587-629.

2.16. VILLAIN, J. in: Ordering in strongly fluctuating condensed matter systems. Edited by T. Riste (Plenum Press, New York) p. 221 and in: Ordering in two dimensions. Edited by S.K. Sinha, (Elsevier, New York, 1980) p. 123.

2.17. DOLLE, P., MATECKI, M. and THOMY, A. (1980). Surf. Sci. 91, 271-282.

2.18. NIELSEN, M., ALS-NIELSEN, J. and MCTAGUE, J.P. (1980) in: Ordering in two dimensions. Edited by S.K. Sinha (Elsevier, New York) 135 p.

2.19. ONSAGER, L. (1944). Phys. Rev. 65, 117-49.

2.20. Both are from the Union Carbide Company.

2.21. For reviews on gases physisorbed on graphite, see
NIELSEN, M., ELLENSON, W.D. and MCTAGUE, J.P. (1978) in: Neutron inelastic scattering 1977, vol. 2, p. 433 (IAEA, Vienna)
and
NIELSEN, M., MCTAGUE, J.P. and PASSEL, L. (1980) in: Ordering in strongly fluctuating co..densed matter systems. Edited by T. Riste (Plenum Press, New York)
and
NIELSEN, M., KJÆR, K., BOHR, J. and MCTAGUE, J.P. (1983). J. Electron Spectrosc. Relat. Phenom. 30, 111-18.

2.22 HAMMONDS, E.M., HEINEY, P., STEPHENS, P.W., BIRGENEAU, R.J. and HORN, P. (1980). J. Phys. C: 13, L301-6.

2.23 STEPHENS, P.W., HEINEY, P., BIRGENEAU, R.J. and HORN, P.M. (1979). Phys. Rev. Lett. 43, 47-51.
and
MONCTON, D.E., STEPHENS, P.W., BIRGENEAU, R.J., HORN, P.M. and BROWN, G.S. (1981). Phys. Rev. Lett. 46, 1533-36.

2.24 NIELSEN, M., ALS-NIELSEN, J., BOHR, J. and MCTAGUE, J.P. (1981). Phys. Rev. Lett. 47, 582-85.

2.25 SINHA, S.K., VORA, P., DUTTA, P. and PASSELL, L. (1982). J. Phys. C: 15, L275-281.
and
VORA, P., SINHA, S.K. and CRAWFORD, R.K. (1979). Phys. Rev. Lett. 43, 704-08.

2.26 KJEMS, J.K., PASSELL, L., TAUB, H., DASH, J.G. and NOVACO, A.D. (1976). Phys. Rev. B: Solid State 13, 1446-62.

2.27 HORN, P.M., BIRGENEAU, R.J., HEINEY, P. and HAMMONDS, E.M. (1978). Phys. Rev. Lett. 41, 961-64.
and
BIRGENEAU, R.J., BROWN, G.S., HORN, P.M., MONCTON, D.E. and STEPHENS, P.W. (1981). J. Phys. C: 14, L49-54.

2.28 VILLAIN, J. (1980) in: Ordering in two dimensions. Edited by S.K. Sinha (Elsevier, New York) p. 123.

2.29 BAK, P. (1982). Rep. Prog. Phys. 45, 587-629.

2.30 TAUB, H., CARNEIRO, K., KJEMS, J.K., PASSELL, L. and MCTAGUE, J.P. (1977). Phys. Rev. B: Solid State 16, 4551-68.

2.31 GÜRTLER, P. and JACKSON, A. (1983). Nuc. Instr. Meth. Phys. Res. 208, 163-66.

3. A NEUTRON SCATTERING STUDY OF DILUTED DIPOLAR ISING FERROMAGNETS

Using neutron diffraction, the dipolar-coupled Ising ferromagnets $LiTbF_4$ and $LiHoF_4$ were studied when the magnetic ions were randomly diluted by yttrium ions. Two crystals were grown: $LiTb_{.3}Y_{.7}F_4$ and $LiHo_{.34}Y_{.7}F_4$ and found to be isostructural with the concentrated crystals. Both ordered ferromagnetically, below Curie points of 0.49 and 0.36 K respectively. The magnetization as well as the critical magnetic fluctuations were studied. A slow saturation with temperature of the magnetic moments was observed. The critical scattering of the $LiHo_{.3}Y_{.7}F_4$ was consistent with that predicted for a dipolar Ising magnet (and found experimentally in $LiTbF_4$). In contrast, the critical scattering of the $LiTb_{.3}Y_{.7}F_4$ was found to contain an anomalous component at small angles. This may be connected to the enhanced significance with dilution of the split ground state of the Tb ion and to anomalies observed in the (bulk) susceptibility of the system.

3.1. Introduction

The compounds $LiRF_4$ with R representing a heavy rare earth ion or yttrium, all crystallize in the tetragonal *Scheelite* structure. Under the influence of the crystalline electric field actting on the rare earth ions, $LiTbF_4$ and $LiHoF_4$ become uniaxial (or Ising) magnets, ordering ferromagnetically at sub-liquid-helium temperatures. There is compelling experimental evidence that the magnetic dipolar interactions between the rare earth magnetic moments are dominant over any "exchange" interactions. The peculiar nature of the dipolar interaction (long ranged and anisotropic) leads to an ordered state consisting of needle-shaped magnetic domains. Likewise, the precursor fluctuations above the Curie point exhibit a marked anisotropy, the correlated regions becoming again very long needles as the transition is approached. Therefore, as has been shown in the literature (refs.

3.43-44, 3.47, 3.24, 3.31 and 3.40) and as will be developed below, the systems can be thought of as simulating a four-dimensional behaviour, i.e. $LiTbF_4$ and $LiHoF_4$ are systems at upper marginal dimensionality. Because of this, theories predict that the critical phenomena near the magnetic phase transition will be mean field like except for logarithmic correction terms. These predictions have been verified in great detail for $LiTbF_4$ (see refs. 3.14-15, 3.31, 3.34-35, 3.48).

Theoretical predictions for a lattice of dipolar-coupled Ising spins, some of which are randomly absent (a random magnet) suggest subtle changes to the critical phenomena, still retaining the essentially mean field-like features[3.49]. $LiTbF_4$ and $LiHoF_4$ lend themselves to an experimental study of such phenomena, since crystals can be grown in which the magnetic ions are replaced partly with closed shell yttrium ions.

Susceptibility studies on diluted crystals $LiTb_pY_{1-p}F_4$ have been reported[3.19-23]. In contrast with theory, a marked departure from mean field theory was observed in the susceptibility critical exponent γ, which rose well above unity as the concentration was lowered.

An important aspect in understanding the behaviour of $LiTb_pY_{1-p}F_4$ may well be the "ground state" of the Tb ion which is in fact a pair of close lying singlets. At $p = 1$ this groundstate splitting is unimportant, but as the net magnetic forces are lowered with dilution, the splitting gains significance. This complication is absent for the $LiHo_pY_{1-p}F_4$ crystals, since the Ho ion has a true doublet ground state.

A neutron diffraction study, reported in this chapter, was undertaken in order to gain information about the microscopic behaviour of the $LiTb_pY_{1-p}F_4$ and $LiHo_pY_{1-p}F_4$ systems and to assess the influence of the ground-state splitting. After several growth attempts, crystals of $LiTb_{.3}Y_{.7}F_4$ and $LiHo_{.3}Y_{.7}F_4$ were obtained and these formed the basis for the investigation.

The rest of the chapter is organized as follows: 3.2 presents the previously available experimental and theoretical information about the rare earth *Scheelite* crystals. In 3.3 the experiments performed are described, and the results are presented and discussed. Finally, 3.4 concludes the chapter.

3.2. Review of the experimental and theoretical situation

In this paragraph we review some of the experimental information regarding the rare earth *Scheelites*. Also the relevant theoretical aspects are reviewed or developed. Only information relevant for the subsequent analysis will be reviewed, so completeness is not the aim.

3.2.1. Crystal structure

The compounds $LiRF_4$ (with R representing: a) a heavy rare earth: Eu, Gd, Tb, Dy, Ho, Er, Tm, Yb or Lu, b) yttrium, c) a mixture of these or d) yttrium with a small doping of any of the rare earth ions) form tetragonal crystals isomorphous to the mineral Scheelite ($CaWO_4$)[3.1,3.2,3.3,3.4]. The space group is $I4_1/a$ (No. 88, C_{4h}^6). There are four formula units in the centered tetragonal cell, in the positions given in Table 3.1.

The structure may be (partly) visualized in the following manner. Within 5 per cent, the lattice constants of the tetragonal crystal obey c = 2a (cf. Table 3.4 on page 88). The metal ions between them occupy the sites of an fcc lattice with lattice constants (a, a, $\frac{1}{2}$ c = a).

In the figure, it may be seen that each Li ion is surrounded by a Fluorine tetrahedron (Li-F distance = 1.90 Å). The rare earth ions are surrounded by two Fluorine tetrahedra of different shape (R-F distances = 2.26 and 2.31 Å).

Table 3.1. The (scheelite) structure of the compounds $LiRF_4$, (R = heavy rare earth or yttrium). Origin at inversion point. All coordinates must be shifted by (0,0,0) and by the body-centering translation (BC) $(\frac{1}{2}, \frac{1}{2}, \frac{1}{2})$. In the body centered cell, there are four formula units, i.e., Z=4,

Ion	Coordinates	Wyckoff Label[3.5]	Site symmetry
Li^+	$\pm$ $(0, \frac{1}{4}, \frac{1}{8})$, BC	4a	$\bar{4}$
R^{3+}	$\pm$ $(0, \frac{1}{4}, \frac{5}{8})$, BC	4b	$\bar{4}$
F^-	$\pm$ $(x,y,z$; $\bar{x}, \frac{1}{2} - y, z$; $\frac{3}{4} - y, \frac{1}{4} + x, \frac{1}{4} + z$; $\frac{1}{4} + y, \frac{1}{4} - x, \frac{1}{4} + z)$, BC	16f	1

The structure is shown in Fig. 3.0.

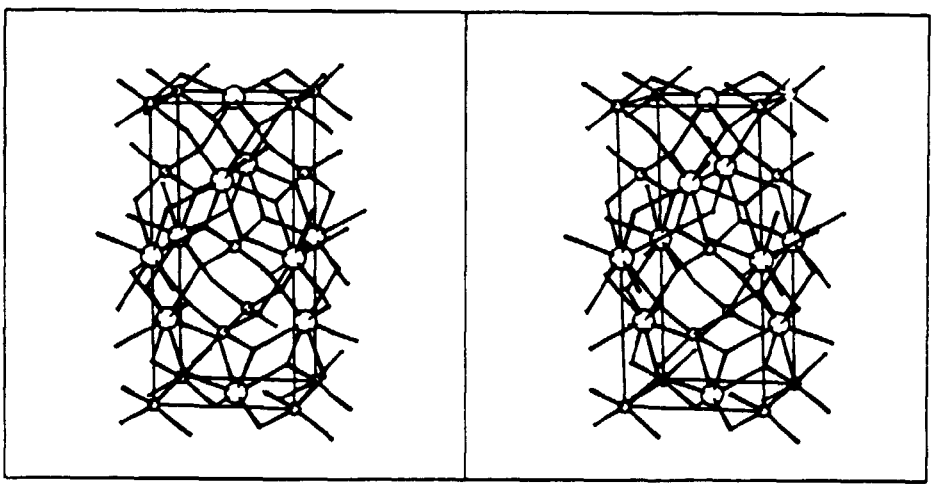

Fig. 3.0. Diastereogram.

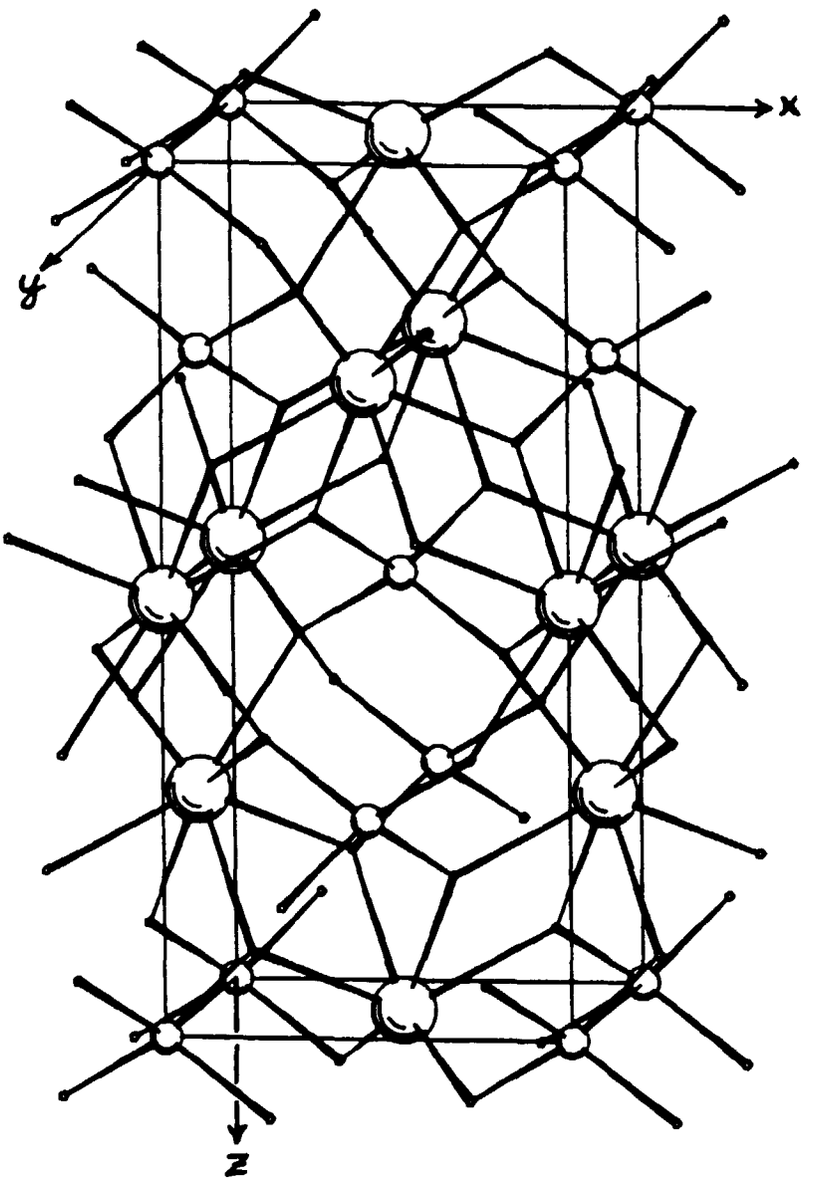

Projection.

Fig. 3.0. Projection and diastereogram[3,77] of the structure of $LiTb_{.3}Y_{.7}F_4$, using atom positions from Table 3.5.
Large spheres: Tb/Y.
Smaller spheres: Li.
Dots: F.
For clarity, the origin in the figure is shifted to coincide with one of the Li positions.

3.2.2. Crystal field and single-ion magnetic properties

In the crystalline electric field (CEF) from the surrounding crystal, the (2J + 1) times degenerate free ion *Multiplet* $^{2S+1}L_J$ of the 4f electrons is split into a series of CEF levels, the energies of which extend over several hundreds of kelvins. Specifically the level schemes for $LiTbF_4$ and $LiHoF_4$ are shown in Fig. 3.1 (reproduced from ref. 3.6).

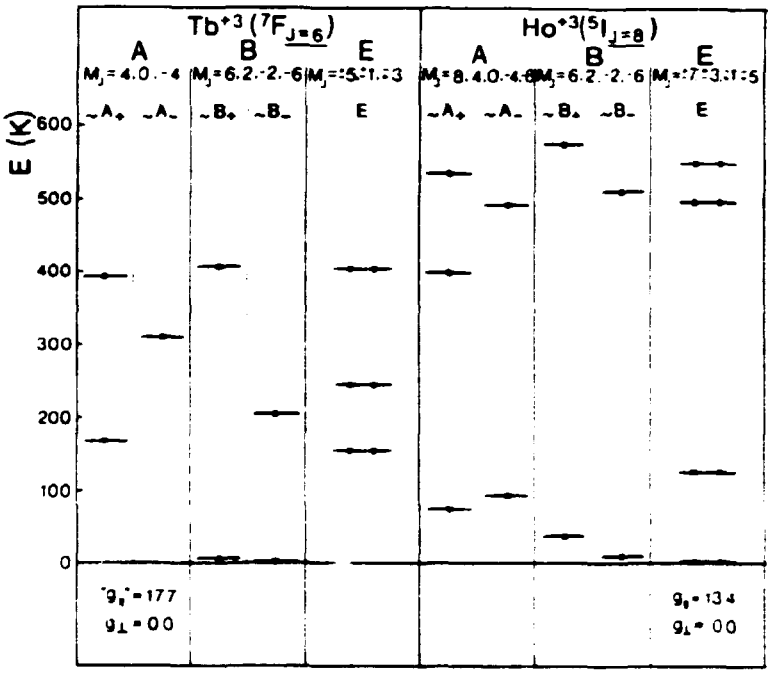

Fig. 3.1. Crystal field levels for Tb^{3+} and Ho^{3+} in scheelite crystals. (Reproduced from Ref. 3.6).

The response of a *free* R^{3+} ion to a magnetic field is given by the Zeeman expression (MKSA units)

$$\vec{\mu} = \chi_T^{free} \vec{H} = \mu_0 \frac{g_J^2 J\cdot(J+1)\mu_B^2}{3k_B T} \cdot \vec{H} \qquad (3.1)$$

where $\vec{\mu}$ is the induced magnetic moment, $\vec{H}$ is the magnetic field, g_J is the Landé factor for the multiplet $^{2S+1}L_J$.

$$g_J = \frac{3}{2} + \frac{S(S+1)-L(L+1)}{2J(J+1)} \quad ,$$

μ_B is the Bohr magneton and $\mu_o = 4\pi \cdot 10^{-7}$ Vs/Am is the vacuum permeability. χ_T^{free} is the free ion polarizability.

For the Ho^{3+} ion in the $LiHoF_4$ crystal field, the ground level is a doublet as shown in Fig. 3.1. At temperatures that are low compared with the energy of the first excited level (9K), the single ion response to a magnetic field becomes

$$\vec{\mu} = \bar{\chi}_T^o \vec{H}$$

Relative to the tetragonal axis, the ionic polarizability tensor $\bar{\chi}_T^o$ is diagonal and has components in the basal plane ($\perp$) and along the c axis ($\parallel$) given by

$$\chi^o_{T\perp,\parallel} = \mu_o \frac{(g_{\perp,\parallel})^2 \mu_B^2}{4kT} \qquad (3.2)$$

where the g-factors for the ground-state doublet are given by

$$g_{\perp,\parallel} = 2\langle 1|_c \, g_J \cdot \hat{J}_{\perp,\parallel} \, |0\rangle_c \, , \qquad (3.3)$$

when the basis states $|1\rangle_c$ and $|0\rangle_c$ of the doublet are chosen as eigenstates of both the CEF operator and the time reversal operator. $\hat{J}_{\perp,\parallel}$ are angular momentum operators. For the Ho^{3+} doublet, $g_\perp = o$, since adjacent μ_J-values do not occur (Fig. 3.1). Thus, $LiHoF_4$ is a uniaxial or Ising magnet, the magnetic moment being confined to the tetragonal axis.

The case of $LiTbF_4$ is slightly more complicated. As shown in Fig. 3.1, the Tb^{3+} ion has two low-lying singlets split by $\Delta = 1.34$ K[3.7]. As derived in Appendix B, the polarizability for the singlet-singlet case is

$$_{ss}\chi^o_T = \mu_o \frac{(_{ss}g)^2 \mu_B^2}{4} \frac{\tanh \frac{\Delta/2}{kT}}{\Delta/2} \qquad (3.4)$$

where the "g-factor" for the close pair of singlets is

$$_{ss}g = 2\langle 1|_c \, g_J \hat{J}_z \, |0\rangle_c \, .$$

Since the singlet states have time-reversal symmetry and adjacent M_I-values do not occur, all other matrix elements such as $\langle 1|_c \vec{J} |1\rangle_c$ or $\langle 1|_c J_x |0\rangle_c$ are zero. Thus also $LiTbF_4$ is an Ising magnet, modified, however, by the splitting Δ of the ground levels which, as shown in Appendix B, corresponds to a transverse magnetic field.

For the other $LiRF_4$ crystals, both $g_\perp$ and $g_{||}$ are non-zero. Thus, the magnetic moment in these crystals is a truly 3-dimensional vector: the crystals are Heisenberg magnets (with some magnetic anisotropy). For the diluted crystals $LiR_pY_{1-p}F_4$ the same $g_{||}$ and $g_\perp$ values are found as for the concentrated crystals[3.7,3.6-3.13]. Thus, the crystal field at a rare earth ion seems to be independent of the ions present at other rare earth sites.

3.2.3. Collective magnetic properties

Ferromagnetism has been observed in $LiTbF_4$[3.12,3.3,3.14,3.15] and $LiHoF_4$[3.6,3.16,3.17,3.18] below Curie points T_C of 2.87 and 1.55 K, respectively. Also the corresponding diluted crystals $LiR_pY_{1-p}F_4$ are seen to order, at least for concentrations $p > 0.15$ (R = Tb)[3.19-3.23,3.4], respectively, $p > 0.3$ (R = Ho)[3.4]. The transitions are continuous. A mean field theory including only magnetostatic dipolar interactions between the ionic magnetic moments comes up with Curie-Weiss temperatures for ferromagnetic ordering that are close to the observed T_C-values, indicating that exchange contributions to the ordering field are small. We review first a mean field theory for magnetic ordering characterized by a non-zero wavevector[3.24] in the long wavelength limit. This sheds some light on the detailed origin of the ordering field, and further, the anisotropy of the fluctuations is established. Mean field theory for a zero wave vector may also be applied. We comment on the connection between the two approaches. With reference to Appendix B, the effect of the ground-level splitting in the Tb compounds is addressed.

3.2.4. Mean field theory for magnetic ordering at non-zero wave vector

We follow the exposition given in Ref. 3.24. The theory applies strictly to the holmium compounds where the ground level is a true doublet.

For any mode of magnetic ordering $\vec{\mu}$(site i) $\equiv \langle\vec{\mu}_i\rangle$(mode), the corresponding susceptibility per ion χ_T^{mode} is given by

$$\frac{\chi_T^o}{\chi_T^{\text{mode}}} = 1 - \frac{\vartheta(\text{mode})}{T} \tag{3.6}$$

where the Curie-Weiss temperature ϑ(mode) for the mode of ordering considered is the energy (in temperature units) gained by a particular spin $\vec{\mu}$(site i) by taking its mean value $\langle\vec{\mu}_i\rangle$(mode) in the presence of the field from the other spins which are held equal to their mean values $\langle\vec{\mu}_j\rangle$(mode). $k_B\vartheta$(mode) is thus found as a sum over the lattice of the interaction energies of the spins. From Eq. (3.6) it is seen that as $T \to \vartheta$ from above, $\chi_T \to \infty$. Below $T = \vartheta$ ($= T_C$ in mean field theory) the spins order in the pattern of the particular mode. The actual mode of ordering, then, will be the mode having the highest value of ϑ.

In the $LiRF_4$ compounds, the magnetic ions occupy two Bravais sublattices 1 and 2 (not four, since a primitive unit cell with Z=2 could be chosen instead of the (Z=4) centered tetragonal cell). We specifically consider modes of magnetic ordering in which the magnetic moments are $\mu(\vec{r}_i) = \vec{\mu}_{1Q} e^{-i\vec{Q}\cdot\vec{r}_i}$ or $\mu_{2Q}\, e^{-\vec{Q}\cdot\vec{r}_i}$ for a site r_i on either sublattice (1 or 2). Then Eq. (3.6) becomes

$$\chi_T^o \cdot \underline{\underline{\chi}}_T(\vec{Q})^{-1} = \underline{\underline{1}} - \frac{1}{T} \cdot \underline{\underline{\vartheta}}(\vec{Q}) \quad , \tag{3.7}$$

where the susceptibility $\underline{\underline{\chi}}_T(\vec{Q})$ is a 2×2 matrix defined by

$$\begin{pmatrix} \mu_1(\vec{Q}) \\ \mu_2(\vec{Q}) \end{pmatrix} = \underline{\underline{\chi}}_T(\vec{Q}) \cdot \begin{pmatrix} H_1(\vec{Q}) \\ H_2(\vec{Q}) \end{pmatrix} \tag{3.8}$$

describing the response to a magnetic field varying as $e^{-i\vec{Q}\cdot\vec{r}}$ and having amplitudes $H_1(Q)$ and $H_2(Q)$ on either sublattice. The matrix

$$\underline{\underline{\vartheta}}(\vec{Q}) = \begin{pmatrix} \vartheta_{11}(\vec{Q}) & \vartheta_{21}^{*}(\vec{Q}) \\ \vartheta_{21}(\vec{Q}) & \vartheta_{11}(\vec{Q}) \end{pmatrix}$$

contains the interactions of the spins within a sublattice (ϑ_{11}) and the interaction of a spin with the spins of the other sublattice (ϑ_{21}). * denotes complex conjugation. Including only the magnetostatic dipolar interactions and putting the origin on a point of sublattice 1, the energy of the interaction between the spin at $\vec{r} = o$ and the other spins on the sublattice is

$$k_B\vartheta_{11}(\vec{Q}) = p \cdot \frac{\mu_o}{4\pi} \frac{(g_{||}\mu_B)^2}{4} \sum_{\vec{r}\neq o} e^{-i\vec{Q}\cdot\vec{r}} \frac{3z^2-r^2}{r^5} \qquad (3.9)$$

where the sum is over the other sites of sublattice 1. The intersublattice value $\vartheta_{21}(\vec{Q})$ is given by the corresponding sum over sublattice 2. Within mean field theory, the Curie-Weiss temperatures for the diluted crystals $LiR_pY_{1-p}F_4$ scale with the concentration p of the magnetic ions. Ordering means a finite response μ to zero field H in Eq. (3.8), i.e.

$$\underline{\underline{\chi}}_T(\vec{Q})^{-1} \begin{pmatrix} \mu_1(\vec{Q}) \\ \mu_2(\vec{Q}) \end{pmatrix} = \begin{pmatrix} 0 \\ 0 \end{pmatrix}$$

or, using (3.7),

$$\begin{pmatrix} \vartheta_{11}(\vec{Q})-T & \vartheta_{21}^{*}(\vec{Q}) \\ \vartheta_{21}(\vec{Q}) & \vartheta_{11}(\vec{Q})-T \end{pmatrix} \cdot \begin{pmatrix} \mu_1(Q) \\ \mu_2(Q) \end{pmatrix} = \begin{pmatrix} 0 \\ 0 \end{pmatrix}, \qquad (3.10)$$

an eigenvalue problem for the Curie temperature $T = T_C$ and the ordering mode ($\mu_1(Q)$, $\mu_2(Q)$). Equation (3.10) can describe any mode of ordering (including non-zero $\vec{Q}$ and different amplitudes on the sublattices). Since the observed ordering is ferromagnetic we now consider the limit $\vec{Q} = 0$. In this limit ϑ_{21} becomes

real[3.24] (θ_{11} is always real since each sublattice has inversion symmetry), and the two solutions to Eqs. (3.10) are

$$T_C = \theta(\vec{Q}) \equiv \theta_{11} + \theta_{21} \ , \ \mu_1 = \mu_2 \tag{3.11}$$

corresponding to ferromagnetic ordering, and

$$T_C = \theta_{11} - \theta_{21} \ , \ \mu_1 = - \mu_2 \ ,$$

describing antiferromagnetic ordering with opposite spins on the two sublatices. Holmes, Als-Nielsen and Guggenheim[3.24] have evaluated the total ferromagnetic Curie-Weiss temperature $\theta(\vec{Q})$ defined in Eq. (3.11) numerically for $LiTbF_4$. Apart from the scale factor in Eq. (3.9), $\theta(\vec{Q})$ depends only on the structure,

$$k_B\theta(\vec{Q}) = p \cdot \frac{\mu_o}{4\pi} \frac{(g_{||}\mu_B)^2}{4} \cdot s(\vec{Q}) \tag{3.12}$$

where

$$s(\vec{Q}) = \sum_{\vec{r}\neq o} e^{-i\vec{Q}\cdot\vec{r}} \frac{3z^2-r^2}{r^5} \tag{3.13}$$

is a sum over all the spin sites.

Since the structure is nearly the same for all of the $LiR_pY_{1-p}F_4$ compounds (see Tables 3.4 and 3.5 below), so also is the lattice sum $s(\vec{Q})$, so that the results of Ref. 3.24 are generally applicable. Figure 3.2 shows the results of Ref. 3.24.

Notable in the figure is the discontinuity at $\vec{Q} = 0$. The long range of the dipolar interaction in Eq. (3.13) leads to conditional convergence of the sum $s(\vec{Q} \equiv 0)$; and the sums $s(\vec{Q} \neq 0)$ become discontinuous at $\vec{Q} \to 0$ for an infinite crystal, as seen in the figure. This has to do with so-called demagnetization effects and has some interesting consequences for the resulting ordered state:

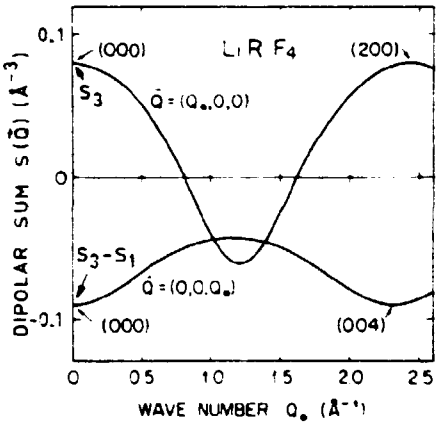

Fig. 3.2. Normalized ferromagnetic dipole sum $s(\vec{Q})$ for the $LiRF_4$ compounds (Eq. 3.13), arrived at by scaling the results of Ref. 3.24 according to Eq. (3.12). As indicated, the intercepts at $\vec{Q} = 0$ are s_3 and $(s_3 - s_1)$, where $s_1 - s_4$ are defined in Eq. 3.14 below. Further, the curvatures at $\vec{Q} = 0$ are $s_4(<0)$ for the $(Q_o,0,0)$ curve and $(s_2 + s_4)(>0)$ for the $(0,0,Q_o)$ curve.

The highest $\theta(\vec{Q})$ occurs for $\vec{Q} \to 0$ as assumed in the analysis above. However, $\theta(Q_z << Q_x \to 0)$ is larger than $\theta(Q_x << Q_z \to 0)$ (which is in fact negative). Thus, the resulting ordered state must be described by wave vectors $\vec{Q} \approx 0$, $Q_{x,y} >> Q_z$, and that implies a structure of magnetic domains whose extent along the Ising axis (ca. $1/Q_z$) is much larger than the transversal dimension (ca. $1/Q_{x,y}$). That is, the magnetic domains are in the shape of thin needles parallel to the Ising axis. This result is perhaps not so spectacular, since it is well known that all ferromagnets form domains of different orientation in zero field as a result of dipolar interactions, or - putting it differently - the domains are formed to minimize the magnetic field energy. However, for most exchange coupled magnets this effect is spurious in a sense in that it results from dipolar interactions which contribute negligibly to the ordering energy. For the $LiR_pY_{1-p}F_4$ compounds, as will be shown, the dipolar interaction

contributes most of the ordering energy, at the same time as causing the ordered state to split up in domains.

The above conclusions are borne out as well by a mean field theory which keeps $\vec{Q} \equiv 0$ from the beginning, as will be seen in the next section. Here we take advantage of the present $\vec{Q}$-dependent formulation to calculate the fluctuations in the paramagnetic phase.

In Ref. 3.24, the following limiting formula for the dipolar lattice sum is arrived at:

$$s(\vec{Q}) = - s_1 \left(\frac{Q_z}{|\vec{Q}|}\right)^2 + s_2 Q_z^2 + s_3 + s_4 |\vec{Q}|^2 , \qquad (3.14)$$

for $\vec{Q} \to 0$, where the parameters are given in Table 3.2 below. The above-mentioned discontinuity is borne out by this equation. The Curie-Weiss temperature for ordering is

$$T_C(MF) = \theta_o \equiv \theta(Q_z << Q_x \to 0) = p \cdot \frac{1}{k_B} \frac{\mu_o}{4\pi} \frac{(g_{||}\mu_B)^2}{4} \cdot s_3 . \qquad (3.15)$$

From (3.7) we find the long wavelength susceptibility per ion, $\chi_T(\vec{Q}) = \chi_{11} + \chi_{21}$:

$$\frac{\chi_T^o}{\chi(\vec{Q})} = 1 - \frac{\theta(\vec{Q})}{T}$$

$$= \frac{T-\theta_o}{\theta_o} + \frac{s_1}{s_3}\left(\frac{Q_z}{|\vec{Q}|}\right)^2 - \frac{s_2}{s_3} Q_z^2 - \frac{s_4}{s_3} Q^2$$

$$= \frac{\xi_o^2}{\xi^2}\left(1 + \xi^2 \left[|\vec{Q}|^2 + g\left(\frac{Q_z}{|\vec{Q}|}\right)^2 - h\, Q_z^2\right]\right) , \qquad (3.16)$$

where we have introduced the correlation length, reduced temperature and correlation length amplitude:

$$\xi = \xi_o \, t_{MF}^{-1/2} \quad ,$$

$$t_{MF} = \frac{T-\theta_o}{\theta_o} \quad ,$$

$$\xi_o = \left(\frac{-s_4}{s_3}\right)^{1/2}$$

and the asymmetry parameters

$$g = \frac{s_1}{-s_4} > o \quad ,$$

$$h = \frac{s_2}{-s_4} > o \quad .$$

In Table 3.2 we give numerical values for the mean field parameters introduced above.

The quantity derived in (3.16) is of considerable importance, being essentially the Fourier transform of the spin-spin correlation function3.37,3.38

$$\frac{\chi_T(\vec{Q})}{\chi_T^o} \propto T \cdot \chi_T(\vec{Q}) \propto \sum_{\text{sites } \vec{r}} e^{-i\vec{Q}\cdot\vec{r}} < s_{\vec{r}=o}(t) \cdot s_{\vec{r}}(t) >_T \qquad (3.16b)$$

where, as indicated by the argument t, the spins are observed simultaneously.

Table 3.2. Parameters for the dipolar Ising magnets $LiR_pY_{1-p}F_4$, R = Ho, Tb. The lattice sums s_1-s_4 were calculated in Ref. 3.24, using the parameters for $LiTbF_4$, a = 5.181 Å and c = 10.873 Å. Since the compounds are quantitatively almost isostructural, the values apply, to a good approximation, to all the crystals. The ordering temperature ϑ_0 scales - within mean field theory with the concentration p and the square of the magnetic moment.

	$LiHo_pY_{1-p}F_4$	$LiTb_pY_{1-p}F_4$	
$g_{\|\|}$, $g_\perp$	13.8 , 0	17.8 , 0	-
$p \cdot \frac{1}{k_B} \cdot \frac{\mu_0}{4\pi} \cdot \frac{g_{\|\|}^2 \cdot \mu_B^2}{4}$	p·29.6	p·49.3	K·Å^3
s_1	.1720		Å^{-3}
s_2	.239		Å^{-1}
s_3	.0805		Å^{-3}
s_4	-.1095		Å^{-1}
$\vartheta_0 = p \cdot \frac{\mu_0}{k_B \cdot 4\pi} \frac{(g_{\|\|}\mu_B)^2}{4} \cdot s_3$	p·2.39	p·3.97	K
$\xi_0 = (\frac{-s_4}{s_3})^{1/2}$	1.17		Å
$g = \frac{s_1}{-s_4}$	1.57		Å^{-2}
$h = \frac{s_2}{-s_4}$	2.2		-

The form (3.16) then implies that, as $T \to T_C$ and $\xi \to \infty$, spin correlations extend over distances of the order of ξ in the a-b plane and over distances

$$\xi_{\|} = g^{1/2} \cdot \xi^2 \qquad (3.16c)$$

in the c direction. This is easily seen[3.31] by deriving the half-maximum contour from (3.16). Thus the precursor fluctua-

tions has the "long needle" character of the ordered phase, as indeed they must in a second-order phase transition. For any given spin, the number of spins well correlated with it, or the volume of correlation, must then vary as

$$\xi \cdot \xi \cdot \xi_{||} \propto \xi^4 .$$

3.2.5. Mean field theory for zero wave vector

We imagine a sample with a uniform (single domain) ferromagnetic magnetization and calculate the mean field sustaining this configuration. From a microscopic point of view, the spins are situated in a vacuum, and thus the energy of a spin μ is simply

$$- \mu_z \cdot B_z = - \mu_z \cdot \mu_o \cdot H_z = - \mu_z \cdot \frac{\mu_o}{4\pi} s(\vec{Q} \equiv 0) \cdot \langle \mu_z \rangle$$

in terms of the magnetic induction density B_z, the magnetic field H_z, the mean value of the spins $\langle \mu_z \rangle$ and the dipole sum $s(\vec{Q} \equiv 0)$ introduced in the preceding section,

$$s(\vec{Q} \equiv 0) = \sum_{\substack{\text{sites} \\ \text{in} \\ \text{sample}}} \frac{3z^2-r^2}{r^5}$$

Here we encounter the problem that $s(\vec{Q} \equiv 0)$, albeit independent of the *size* of the sample, is dependent on its *shape* Mathematically, this is because the dipole sum is conditionally convergent. Following Lorentz[3.25], we derive the shape dependence by writing

$$H_z = \frac{1}{4\pi} \sum_{\substack{\text{sites} \\ \text{within} \\ \text{sphere}}} \langle \mu_z \rangle \frac{3z^2-r^2}{r^5} + \frac{1}{4\pi} \int_{\substack{\text{rest} \\ \text{of} \\ \text{sample}}} \frac{\langle \mu_z \rangle}{V_{spin}} \frac{3z^2-r^2}{r^5} \, dV$$

where the contribution from the spins within a chosen imaginary sphere are evaluated exactly once and for all, and the rest of

the spins are treated in a continuum approximation, i.e. in terms of the magnetization $\langle\mu\rangle/V_{spin}$. The larger the sphere, the better the approximation. As derived in elementary text books, the latter contribution is constant throughout a sample in the shape of an ellipsoid and can be expressed in terms of equivalent polarization charges on the imaginary sphere and on the surface of the sample, with the result

$$H_z = \frac{1}{4\pi} s_{sphere}(\vec{Q} \equiv 0) \cdot \langle\mu_z\rangle + (\frac{1}{3} - N) \cdot \frac{\langle\mu_z\rangle}{V_{spin}} \qquad (3.17)$$

Here the dipole sum $s(\vec{Q} = 0)$ is evaluated for a large sphere, and the standard demagnetization factor N has been introduced. Of course, N = 1/3 for a sphere. We include for completeness a field H_{ext} from external sources and display the resulting equation.

$$H_z = \underset{(a)}{\frac{\langle\mu_z\rangle}{4\pi} \cdot s_{sphere}} + \underset{(L)}{\frac{1}{3} \cdot \frac{\langle\mu_z\rangle}{V_{spin}}} + \underset{(d)}{(-N \cdot \frac{\langle\mu_z\rangle}{V_{spin}})} + \underset{(e)}{H_{ext}} \qquad (3.18)$$

(a: anisotropy field; L: Lorentz field; d: demagnetizing; e: external; d+e: internal field, Maxwell field; a+L+d+e: local field).

The nomenclature is rich. The term "local" for the field actually experienced by the spins seems well chosen. The macroscopic Maxwell equations consider only averaged quantities such as the magnetization $\langle\mu_z\rangle/V_{spin}$ and thereby miss the two first terms. These in turn are the "anisotropy" field (which indeed is zero in high, e.g., cubic, symmetry) and the (everpresent) "Lorentz" field. Finally, the "demagnetizing" field (formally arising from polarization charges on the surface of the sample) indeed reduces the externally applied field, thereby also reducing the resulting magnetization.

From (3.17) the Curie-Weiss temperature is derived:

$$k_B\theta = p \cdot \frac{\mu_o}{4\pi} \cdot \frac{(g_{||}\mu_B)^2}{4} \cdot (s(\vec{Q} = 0) + \frac{4\pi}{V_{spin}} (\frac{1}{3} - N)) \tag{3.19}$$

Thus, assuming single domain magnetization, we come up with a shape-dependent ordering temperature. (Such shape dependence is discussed in Refs.[3.26-3.30]).

It is apparent, however, that a sample of any shape can lower its energy by breaking up in domains of zero demagnetization factor, i.e., long thin needle-shaped domains in the ferromagnetic phase. This is the same domain structure as predicted in the previous section. (Such a domain structure has indeed been observed for $LiTbF_4$ and $LiHoF_4$ by neutron scattering[3.31-32] and optical techniques[3.14,3.17,3.18].)

There is, of course, also quantitative agreement between the two formulations of mean field theory. Using the parameters for $LiTbF_4$[3.3], the lattice sum $s(\vec{Q} = o)$ was calculated in Ref. 3.33, with the result $s = 0.02308\ \text{Å}^{-3}$. This is in good agreement with the spherical average of Eq. (3.14), $1/3 \cdot (- s_1) + s_3 = 0.02317\ \text{Å}^{-3}$. More interestingly, the parameter directly giving the Curie-Weiss temperature, $s(\vec{Q} \equiv 0) + 4\pi/3V_{spin}$ equals $0.0805\ \text{Å}^{-3}$, in agreement with $S(Q_z << Q_x \to 0) = s_3$.

Next, we include the ground-level splitting of the Tb^{3+} ion in the description. The susceptibility in the paramagnetic phase is

$$\chi_{ss}T = \mu_o \frac{(_{ss}g\mu_B)^2}{4} \cdot \frac{1}{\Delta/2} \cdot (\coth \frac{\Delta/2}{kT} - \frac{\theta}{\Delta/2})^{-1} \tag{3.20}$$

where θ is the Curie-Weiss temperature for zero splitting of the levels. Thus the mean-field transition temperature is suppressed from $T_C(MF) = \theta$ to a value given by

$$\coth \frac{\Delta/2}{kT_C} = \frac{k\theta}{\Delta/2} \qquad (3.21)$$

and for $k\theta/(\Delta/2)$ less than one, the system never orders. In the ordered phase the magnetisation curve can be constructed by the usual self-consistent method: An assumed mean magnetic moment $\langle\mu\rangle$ leads to a molecular field given by (3.17), which must in turn stabilise the assumed moment $\langle\mu\rangle$ in accordance with the calculated single-ion magnetization curve $\mu = \mu(H,T)$.

The magnetic moment at zero temperature is suppressed below the value $(g\mu_B/2)$ applying for zero-level splitting. The analysis in Appendix B shows that, within the mean field approximation, the effect of the level splitting is negligible for values of $k\theta/(\Delta/2)$ greater than five, say.

3.2.6. Dipolar interactions

We review the evidence for dominant dipolar interactions between the magnetic moments in $LiTbF_4$ and in $LiHoF_4$. Table 3.3 gives the observed transition points T_C, and Curie-Weiss temperatures, θ, and compares them to the calculated mean-field (MF) value using only the dipolar interactions. The mean-field approximation overestimates T_C by ignoring the fluctuations close to the transition but compares well with the experimental θ which are measured well above T_C, where the fluctuations are small. Thus, the contribution of exchange forces to the ordering is estimated by

$$\theta_{exch} \simeq \theta_{dip,mean\ field} - \theta_{meas}.$$

This leads to the conclusion that for $LiTbF_4$, the exchange contribution is minus ten per cent. For $LiHoF_4$, the exchange has the same absolute magnitude, suppressing the observed Curie-Weiss temperature by about 20 per cent.

The same result was reached (for $LiTbF_4$) by Holmes *et al.*[3.24], who, by comparing their neutron diffuse-scattering data to the cross-section calculated with dipolar interactions only, were

Table 3.3. 1) Calculated dipolar-only Curie-Weiss temperatures using a) $g_{||} = 17.8$ for $LiTbF_4$ and b) $g_{||} = 13.8$ for $LiHoF_4$. 2) Observed Curie-Weiss temperatures, from the T-dependence of the reciprocal susceptibility well above T_C [except c), which was based on data immediately above T_C]. 3) Observed transition points.

	1) θ_{dip}	2) θ_{meas}	3) $T_{C,meas}$	Ref.
	K	K	K	
$LiTbF_4$	3.97[a]	3.6	2.86	3.12
		3.72	2.865	3.34
		3.57		3.9
$LiHoF_4$	2.39[b]	2.0	1.30	3.6
		1.50[c]	1.53	3.16
		$1.9 \mp .1$		3.9
			1.52	3.17
			1.54	3.18

able to conclude that an assumed nearest and next nearest neighbour exchange coupling is so large as to lower the Curie-Weiss temperature by about 12 per cent.

Thus, the magnetic dipolar interaction is the dominant force between the spins.

3.2.7. Critical phenomena

The mean-field theory (MF) outlined above contains predictions about the singular variation of various quantities near the ferromagnetic phase transition: The interior susceptibility, correlation length and spontaneous magnetization vary as

$$\frac{\chi_{int}}{\chi_T^o} = \frac{\chi(Q_z << Q_x \to 0)}{\chi_T^o} \propto \left(\frac{T-T_c}{T_c}\right)^{-\gamma} , \quad \gamma = 1 ,$$

$$\xi = \xi_o \left(\frac{T-T_c}{T_c}\right)^{-\nu} , \quad \nu = 1/2 ,$$

$$\langle \mu \rangle \propto \left(\frac{T_c-T}{T_c}\right)^{\beta} , \quad \beta = 1/2 .$$

For completeness, the heat capacity Cp can be calculated also, with the result that C_p shows a finite jump at T_C, i.e. we can write for the singular part,

$$C_p \propto \left|\frac{T-T_C}{T_C}\right|^{\alpha} , \quad \alpha = o .$$

Also, the full (long wavelength) $\vec{Q}$-dependence of $\chi(\vec{Q})$ was derived (Eq. 3.16).

It is well known that experiments on critical phenomena disprove the quantitative results of simple mean-field theory. Better agreement is obtained by various other theoretical methods, in particular by the so-called Renormalization Group (RG) techniques[3.39], which come up with critical exponent α, β, γ and ν different from the MF values quoted above. The general result of RG theory is that for systems of spatial dimensionality (d) larger than a marginal dimensionality ($d^* = 4$) MF predicts the critical phenomena correctly; for $d = d^* = 4$, there are only small logarithmic correction factors which can be calculated exactly within RG; whereas for $d < d^*$, RG yields critical exponents different from the MF values (and in most cases the ex-

ponents can only be calculated approximately). Since only $d < 3 < d^* = 4$ is accessible in real physical systems, this correspondence with the simple theory may seem of little practical value.

The condition $d > d^* = 4$ for MF to apply comes about because MF ignores the effect of fluctuations on the thermal averages in question. In particular, long wavelength fluctuations are important because they have low energies, and spatial dimensionality affects the critical phenomena by the amount of phase space available for long wavelength fluctuations[3.40].

We can now argue heuristically that the dipolar-coupled Ising magnets concerning us here are a special case for the following reason[3.41]; As $T \to T_C$ and the correlation length $\xi \to \infty$, the volume of correlation varies as $\xi \cdot \xi \cdot \xi_{||} \propto \xi^4$ (as derived above), simulating a four-dimensional system. Thus the system is <u>at</u> marginal dimensionality: $d^* = d = 3$ for a dipolar coupled Ising magnet.

This result is borne out by a full Renomalization Group analysis of the system[3.42-3.46]. The RG theory can be worked out exactly in this case and the predictions are

$$C_p \propto |\ln t/t_o|^{1/3}, \tag{3.23}$$

$$\mu \propto t^{1/2} |\ln t/t_o|^{1/3}, \tag{3.24}$$

$$\frac{\chi_T(\vec{Q})}{\chi_T^o} = \frac{\xi^2}{1+\xi^2(Q^2+g|\frac{Q_z}{Q}|^2-hQ_z^2)}, \tag{3.25}$$

$$\xi^2 \propto t^{-1} |\ln t/t_o|^{1/3}, \tag{3.26}$$

$$t \equiv \left|\frac{T-T_C}{T_C}\right|,$$

i.e., the predictions of MF theory modified by logarithmic correction factors. The term $\ln(t_o)$ actually represents higher-order terms in the correction factor ($\sim \ln|\ln t|$). In (3.25), the parameters g and h are different from their MF values (Table 3.2), and vary slowly with temperature, but the fundamental anisotropy in the diverging fluctuations is obviously retained. The following relation connecting the amplitudes in (3.23-3.26) was also derived:[3.47]

$$\xi_{\perp}^2 \xi_{\parallel} C_p \, t^2/k_B = \frac{3}{32\pi} |\ln t/t_o| \qquad (3.27)$$

As discussed in the preceeding section, a non-dipolar term is present in the Hamiltonian describing $LiTb_pY_{1-p}F_4$ and $LiHo_pY_{1-p}F_4$. The influence of this term on the critical phenomena has been addressed in Ref. 3.44. The conclusion of this paper is that between the phase transition point and a certain crossover reduced temperature t_x, (i.e., $0 < t < t_x$) the dipolar interactions will dominate the critical phenomena, leading to the results (3.23 - 3.27) above.

t_x is given by

$$t_x \sim \text{(dipolar term)/(exchange term)},$$

i.e., $t_x \sim$ 5-10 for the scheelite crystals considered here. Thus, the results (3.23-3.27) can probably be applied to the scheelites. (It must be noted, though, that ref. 3.44 deals with a ferromagnetic exchange term, whereas a term defracting from the mean dipolar forces is observed in $LiTb_pY_{1-o}F_4$ and $LiHo_pY_{1-p}F_4$).

On the experimental side, much detailed work has been done on $LiTbF_4$. Specific heat data could be fitted[3.48] with Eq. (3.23), neutron scattering data 3.31, 3,40 confirmed Eqs. (3.25-26) and - together with the specific heat data[3.48] - the amplitude relationship (3.27). The spontaneous magnetization was measured by neutron diffraction[3.3] and by means of light scattering[3.14]. The full equation of state $\mu = \mu(H,t)$ was measured[3.15] and found to agree with the theory[3.42]. Also, the susceptibility $\chi(Q_z << Q_x \to 0)$ was measured[3.35].

Although standard power laws with empirical exponents ($\alpha, \beta, \gamma, \nu$) could in some cases fit the data as well as RG Eqs. (3.23-27), all of the data are in agreement with the RG predictions and, further, several non-trivial amplitude relations, e.g., Eq. (3.27) and relations between amplitudes (understood in Eqs. (3.23-27)) above and below T_C have been confirmed. Therefore, it seems well warranted when several authors call $LiTbF_4$ one of the best understood systems in the field of critical phenomena. For $LiHoF_4$ the data is less abundant. The susceptibility was measured and found to agree equally well with Eqs. (3.25-26) and with the standard power law.[3.36]

A measurement of the spontaneous magnetization yielded significantly better agreement with the proposed Eq. (3.24) than with any power law.[3.18]

3.2.8. Dilution by yttrium

Renewed interest in the rare earth scheelites was spurred by the theory of Aharony[3.49] on the random Ising dipolar-coupled magnet. Using the renormalization group technique to study a magnetic lattice in which some of the spins are absent (at random), he concluded that below a cross-over (reduced) temperature t_x given by

$$|\ln t_x| \propto (p(1-p))^{-3} , \tag{3.28}$$

(p being the fraction of spins present), a new type of critical behaviour was to be expected: The singular part of the heat capacity should vary as

$$C_{sing} \propto - |\ln t|^{1/2} \exp(-2(D|\ln t|)^{1/2}) , \tag{3.29}$$

$$D \equiv 0.11795 \ldots$$

and the correlation length and susceptibility as

$$\chi \propto \xi^2 \propto t^{-1} \exp((D|\ln t|)^{1/2}). \tag{3.30}$$

Finally,

$$\xi^2 \xi_{||} \, C_{sing} \, t^2/k_B = - \frac{1}{32\pi} \left(\frac{|\ln t|}{D}\right)^{1/2} . \qquad (3.31)$$

A general argument[3.50] suggests that a new type of singular behaviour is to be expected on random dilution of systems having a diverging heat capacity C_p. As the heat capacity shows a weak logarithmic singularity (Eq. 3.23), the "marginal" change fro. logarithmic correction factors (Eqs. 3.23-27) to those of Eqs. (3.28-31) is perhaps not so surprising.[3.49]

The rare earth scheelites $LiTbF_4$ and $LiHoF_4$ naturally lend themselves to experimental investigations of these phenomena, as the magnetic ions can be replaced with closed-shell Y^{3+} ions with little distortion of the surrounding crystal structure or of the crystalline electric field on the rare earth ions present. An important question in this context is that of the existence of any correlation of the occupation of the Y/Tb/Ho sites, since such a correlation could probably influence the critical behaviour markedly. On macroscopic scales, such correlations (or clustering) can be easily detected, and on a scale of microns, the correlations can be assessed by monitoring the characteristic X-ray fluorescense as an electron beam is swept over the sample in an electron microscope (EDAX technique), or by other similar methods relying on characteristic radiation from atoms or nuclei. Further, a sharp phase transition may itself be taken as evidence for the absence of clustering on scales larger than the correlation length.

Yttrium-diluted crystals $LiTb_pY_{1-p}F_4$ were studied for $p = 0.5$ and 0.3 in Refs. 3.19-3.21 and for eight concentrations $p > 0.15$ in Refs. 3.22 and 3.23, by susceptibility measurements. The crystals were found to order ferromagnetically. At the higher concentrations, the data could be fitted by both the non-classical laws (3.25-26) and (3.30) as well as by the empirical power law $\chi \propto t^{-\gamma}$, with γ rather close to one. For lower concentrations, only the power law could fit the data and the exponent γ departed markedly from unity in good agreement with the semi-empirical relation

$$\gamma(p) = \gamma(p = 1) \cdot \frac{T_C(p=1)}{T_C(p)} .$$

Reference 3.51 argues that this departure from the predicted behaviour (3.29-31) may come about because the true critical region shrinks to be inaccessible close to T_C as $p \to 0$.

A cruder feature is the dependence of the transition point itself upon the concentration, i.e. $T_C = T_C(p)$. Within mean field theory for the $LiTb_pY_{1-p}F_4$ crystals, T_C is given by Eq. (3.21) (see Fig. B.2)

$$\coth \frac{\Delta/2}{kT_C} = \frac{k\theta}{\Delta/2} = p \cdot \frac{k\theta(p=1)}{\Delta/2} ,$$

i.e., T_C first decreases linearly with p, then bends down and becomes zero when

$$p = p_o = \frac{\Delta/2}{k\theta(p=1)} = 0.19 ,$$

using $\Delta/k = 1.34$ K and $\theta(p = 1) = 3.6$ K. MF theory overestimates T_C, of course. Scaling the interactions[3.52] to reproduce the observed $T_C(p = 1)$, one arrives at $p_o = 0.23$, and good agreement is obtained with the observed $T_C(p)$, except at small p, where ferromagnetism is observed below p_o. This may be caused by the (hyperfine) interaction between the electronic and nuclear magnetic moments which may become important at the very low temperatures relevant in this limit[3.51,3.52] (T_C ($p = 0.15$) = 0.13 k[3.51]).

For the diluted $LiHo_pY_{1-p}F_4$ crystals, MF arguments, of course, predict transition temperatures proportional to p, since the ground state is degenerate. No work seems to have been done on these crystals prior to that reported here below.

3.3. Experiments, results and discussion

We present here the experimental results of this study. Single crystals of $LiTb_{.3}Y_{.7}F_4$ and $LiHo_{.3}Y_{.7}F_4$ were grown. The structure (i.e., the fluorine positions) of the Tb compound was found

by a neutron structure determination. The spontaneous magnetization curve was derived from the intensity of magnetic Bragg reflections when the crystals were mounted in a ^3He - ^4He dilution refrigerator on a neutron diffractometer, and also by neutron scattering the fluctuations near the transition were determined.

3.3.1. Crystal growth[3.54]

Crystals of $LiTb_{.3}Y_{.7}F_4$ and $LiHo_{.3}Y_{.7}F_4$ were grown by spontaneous nucleation from the melt. Several unsuccessful attempts were made, the failure of which could be attributed to insufficient purity of the starting materials.

Terbium and holmium trifluoride[3.55] and yttrium trifluoride[3.56] in the molar ratio of 30:70 were mixed with lithium fluoride. Relative to the peritectic points calculated from the data in Refs. 3.1 and 3.2 the mixture was LiF-rich by *ca.* one molar per cent. For the holmium compound, ^7LiF[3.57] was used to avoid neutron absorption by the (7.5 per cent abundant) ^6Li nuclei. The resulting 50 g of chemicals were mixed with 8 g of $NH_4F \cdot HF$[3.58] and put in a 50 ml platinum crucible which was then placed in the INCONEL oven. Several times the oven was evacuated and flushed with grade N48 Argon. Following this, the temperature was raised to 300°C overnight, while the oven was flushed with 1 atm. argon gas. This was to obtain dehydrolysation and fluorisation of any oxides formed[3.53]. Subsequently, the temperature was raised another 100°C and the system was pumped and flushed with argon at low pressure for several hours to remove volatile reaction products, including HF. Then, at a 1 atm. argon flow, the temperature was raised to 1000°C, the flow was stopped and the melt was allowed to mix for at least 15 hours. With a temperature gradient of as much as 70°C over the crucible (to avoid supercooling) the temperature was then lowered through the temperature range of (incongruent) solidification (815°C to 695°C from Ref. 3.1, 3.2) at a rate of 2 °C/h.

The oven was allowed to cool and the boule was extracted. By inspection, by X-ray Laue back-reflection pictures and by the subsequent neutron diffraction study it was established that the

right phase had been obtained. As established by the Laue pictures, the $Li(Ho,Y)F_4$ boule contained quite a few single crystals. These were separated by crushing the boule and the largest single crystal was selected for the neutron study. The $Li(Tb,Y)F_4$ boule contained large single crystals, and large pieces could be cut from it with a string saw.

To establish the chemical composition and homogeneity, a piece of $Li(Tb,Y)F_4$ crystal was polished, coated with a carbon film and placed in an electron microscope[3.59]. Maps of the terbium and yttrium X-ray L-fluorescence were recorded as the 40 keV electron beam was swept over the sample. Negative intensity correlations between the two maps were looked for and not found on length scales of micrometers to 0.2 mm. Such correlations would be evidence of variations in the Tb:Y ratio over the sample. Quantitatively, the observed intensities yielded Tb concentrations of around p = 0.32, but the accuracy of this number is uncertain[3.60]. The composition was taken to b that of the melt: $^{nat}LiTb_pY_{1-p}F_4$ and $^{7}LiHo_pY_{1-p}F_4$, with $p = 0.30 \pm 0.02$.

Another check on the homogeneity is provided by the sharpness of the ferromagnetic phase transition (see Fig. 3.3 below). By fitting the observed magnetic Bragg intensity with a power law $I \propto (T_C-T)^1$ smeared with a Gaussian distribution of T_C, the standard deviation $\sigma T_C/T_C$ was found to be 0.04 for $LiHo_{.3}Y_{.7}F_4$ and 0.06 for $LiTb_{.3}Y_{.7}F_4$. From the known[3.23] $T_C(p)$ curve this gives $\sigma(p) = 0.01$ for $LiTb_{.3}Y_{.7}F_4$ and (assuming $T_C(p)$ to be linear) $\sigma(p) = 0.008$ for the $LiHo_{.3}Y_{.7}F_4$ crystal. These numbers must be regarded as upper bounds, as the data were not corrected for critical scattering. A sharp peak in the critical scattering was observed when the $LiHo_{.3}Y_{.7}F_4$ crystal was passed through the the transition point. Interpreting the temperature width of this peak as solely due to a T_C-smearing yields the same upper bound $\sigma(p) = 0.008$.

3.3.2. Structure refinement of $LiTb_{.3}Y_{.7}F_4$[3.61]

In order to verify that the structure of the intermediate compound $LiTb_{.3}Y_{.7}F_4$ is indeed isomorphous to the known structures

of the $LiRF_4$ crystals[3.1,3.2,3.3] and in particular to determine the small quantitative deviations from, e.g., the $LiTbF_4$ structure[3.3], a conventional neutron structure analysis was performed.

A single crystal of $^{nat}LiTb_{.3}Y_{.7}F_4$ was ground to a sphere of diameter 4.0 mm. It was mounted on a four-circle diffractometer, in a monochromatic beam of wavelength λ = 1.070 Å produced by Bragg reflection in a Beryllium (002) monochromator crystal of a thermal neutron beam from the Risø DR 3 reactor. At room temperature (295 K) 1283 reflections and at low temperature[3.62] (175 K) 1213 reflections were measured within a sphere of $\sin\theta/\lambda < 0.79$ Å^{-1}. Peak and background were located in the measured profiles (intensity *vs.* crystal rotation) by an automatic computer routine[3.63], and the resulting integrated intensities were corrected for absorption[3.65] (using the linear absorption coefficient μ = 0.70 cm^{-1} [3.64]).

Observed structure factors F^2 in arbitrary units were deduced, $F^2 \propto \sin(2\theta)\cdot$(integrated intensity). Assuming the space group $I4_1/a$, the structure factors were averaged over each *form* {hkl} of symmetry-related reflections, giving about 290 reflections for each temperature and internal consistency R-factors of 2.7%,

$$R_{int} = \sum_{hkl} |F^2_{obs} - \langle F^2_{obs} \rangle| / \sum F^2_{obs} .$$

About 100 reflections that are forbidden in $I4_1/a$ symmetry were measured and found to be zero or very small. They were not included in the subsequent refinement.

The observed structure factors F^2_{obs} were compared to the calculated ones

$$F^2_{hkl} = \left| \sum_j b_j \exp(i\vec{\tau}\cdot\vec{r}_j) \exp(-\frac{1}{2}\vec{\tau}\cdot\overline{\overline{U}}_j\cdot\vec{\tau}) \right|^2 , \qquad (3.32)$$

where, for atom j at position $\vec{r}_j$, b_j is the scattering length and the anisotropic thermal vibrations enter through the $\overline{\overline{U}}_j$-matrix. $\vec{\tau} = h\vec{a}^*+k\vec{b}^*+\ell\vec{c}^*$ is the Bragg vector, $|\vec{\tau}| = 4\pi\cdot\sin\theta/\lambda$.

Starting from the parameters of $LiTbF_4$[3.3], the structure of $LiTb_{.3}Y_{.7}F_4$ was refined by minimizing the expression

$$\sum_{hkl} \sigma_{hkl}^{-2} \left(\frac{F_{obs}^2}{E_{hkl}} - k^2 F_{calc}^2\right)^2$$

Here the observed intensities are corrected for extinction by the isotropic factor $E_{hkl}(g)$ which depends on the adjustable parameter g[3.66]. k is a scale factor. The standard deviation σ_{hkl} of F_{obs}^2 was based on counting statistics or on the scatter of data within a form {hkl}, whichever yielded the larger value. The structure could be refined within the Scheelite structure (Table 3.1), with resulting R-factors

$$R = \sum_{hkl} |F_{obs}^2 - E_{hkl}\, kF_{hkl}^2| / \sum F_{obs}^2$$

of 3.7 and 3.3 per cent for the room temperature and cold data. The refined extinction parameter g equals 4900 ± 150, corresponding to a (Lorentzian) mosaic distribution of width 6.7 seconds of arc (HWHM). Allowing the individual scattering lengths b_j to vary did not yield significantly lower R-values nor change the b_j from their nominal values b(natural lithium) = -0.214, b(Tb) = b(Y) = 0.76 and b(F) = 0.56 × 10^{12} cm. The weak reflections were consistently observed stronger than the calculated values. A correction for an assumed 2nd-order contamination of the monochromatic beam of 0.5% or 2% did not remedy this discrepancy. Thus we assume that the extra intensity comes from multiple scattering.

In Table 3.4 the lattice constants of the $LiRF_4$ crystals are compared, and Table 3.5 shows the results of this structural analysis and compares it to other known structures.

In conclusion, the structure of $LiTb_{.3}Y_{.7}F_4$ has been shown to be isomorphous to the mineral scheelite (Table 3.1). The adjustable parameters (fluorine coordinates) of the structure have been determined and shown to be close to those of $LiTbF_4$ and $LiYbF_4$. Thus, accurate structure factors are available. These, however, when small do not compare well with the measured intensities, probably because of multiple scattering.

3.3.3. Low-temperature set-up

For the low-temperature measurements described in the following sections, the samples were mounted in a ^3He-^4He dilution refrigerator[3.69]. The samples were thermally anchored to the mixer chamber through a copper pin. A calibrated germanium thermistor on the mixer chamber was used as thermometer, the conductance being measured by an a.c. bridge. An electric heater on the mixer chamber was used to control temperature, as a proportional control loop was established by means of a d.c. output from the bridge and an amplifier. Temperatures down to 0.090 K were obtained.

Table 3.4. Lattice constants of the scheelite crystals $LiRF_4$, for various ions R.

R	a Å	c Å	c/a	temp.	ref.
Y	5.26(3)	10.94(3)	2.08	room	3.1
Y	5.175(5)	10.74(1)	2.077	"	3.67
Eu	5.228(5)	11.03(1)	2.110	"	"
Gd	5.219(5)	10.97(1)	2.102	"	"
Tb	5.200(5)	10.89(1)	2.094	"	"
Tb	5.192(3)	10.875(6)	2.095	295 K	3.3
Tb	5.181(3)	10.873(6)	2.099	100 K	3.3
Dy	5.188(5)	10.83(1)	2.087	room	3.67
Ho	5.175(5)	10.75(1)	2.078	"	"
Er	5.162(5)	10.70(1)	2.073	"	"
Tm	5.145(5)	10.64(1)	2.067	"	"
Yb	5.132(5)	10.59(1)	2.064	"	"
Yb	5.1335(2)	10.588(2)	2.063	"	3.2
Lu	5.124(5)	10.54(1)	2.057	"	3.67
$Ho_{.3}Y_{.7}$	5.146(1)	10.758(1)	2.090	1 K	this work
$Tb_{.3}Y_{.7}$	5.18(1)	10.83(1)	2.09	295 K	"
$Tb_{.3}Y_{.7}$	5.186(5)	10.826(5)	2.087	175 K	"
$Tb_{.3}Y_{.7}$	5.130(1)	10.735(1)	2.093	1 K	"

The $^{nat}LiTb_{.3}Y_{.7}F_4$ sample used in the low-temperature measurements was cut and polished to a plate parallel to the a-b plane, 2.6 mm thick by 65 mm^2, the thickness being chosen to approximately match the absorption length for 5-meV neutrons, μ^{-1} = 3.9 $mm^{3.64}$. The copper pin ended in a pair of chaps which could hold the platelet firmly. The $^7LiHo_{.3}Y_{.7}F_4$ sample was cut from the largest singly crystalline piece to a quasi-regular shape of 6 × 6.5 × 8 mm^3 (a × a × c). At 5 meV, μ^{-1} = 12 $mm^{3.64}$. The crystal was held to the copper pin by a copper brace and was polished where it would make contact with the copper. The latter design proved inferior to the former in that longer equlibrium times were observed. The equilibrium of sample temperature was monitored by observing the magnetic Bragg intensity as a function of time at fixed temperature of the ^3He-^4He mixer chamber and equilibrium times were in the order of tens of minutes and hours, respectively, for the two designs.

The copper was masked from the neutron beam by cadmium foil.

3.3.4. Magnetic ordering

Both crystals were seen to order ferromagnetically below Curie temperatures of (0.493 ± .005)K ($LiTb_{.3}Y_{.7}F_4$) and (0.360 ± .002)K ($LiHo_{.3}Y_{.7}F_4$), through second-order phase transitions. This was evidenced by a continuous increase in the intensity of the magnetic Bragg reflections (103), (301) and (305) (Fig. 3.3a & b). For the holmium compound, a peak in the critical scattering also marked the transition (Fig. 3.3c).

Details of the data taking are given in the following sections.

Table 3.5. The known structures of $LiRF_4$ crystals. The temperature parameters U are defined in Eq. (3.32). For $LiTb_{.3}Y_{.7}F_4$, the quoted uncertainties derive from the uncertainties of measured F^2-values, i.e. are exclusive of any systematic errors. The two values given for the fluorine y-coordinate in the $Tb_{.3}$ compound refer to two different settings of the tetragonal right-hand coordinate system relative to the crystal.

	atom	x	y	z	U_{11}	U_{22}	U_{33}	U_{12}	U_{13}	U_{23}	temp.	rad.	ref.
					$Å^2$	$Å^2$	$Å^2$	$Å^2$	$Å^2$	$Å^2$			
$LiTbF_4$	Li	0	1/4	1/8	.0202(24)	$=U_{11}$	.0268(16)	0	0	0	295 K	1.07 Å	3.3
	Tb	0	1/4	5/8	.0125(5)	$=U_{11}$	.0110(3)	0	0	0	-	neutrons	
	F	.2198(1)	.4119(1)	.4560(1)	.0182(3)	.0177(3)	.0172(3)	.0035(2)	.0040(2)	.0030(2)	-		
	Li	0	1/4	1/8	.0163(35)	$=U_{11}$	.0178(21)	0	0	0	100 K		
	Tb	0	1/4	5/8	.0092(7)	$=U_{11}$	.0089(4)	0	0	0	-		
	F	.2199(2)	.4107(2)	.4563(2)	.0127(4)	.0124(4)	.0127(4)	.0014(4)	.0016(3)	.0010(3)	-		
$LiTb_{.3}Y_{.7}F_4$	Li	0	1/4	1/8	.0121(5)	$=U_{11}$	.0165(10)	0	0	0	295 K	1.07 Å	this work
	Tb/Y	0	1/4	5/8	.0054(2)	$=U_{11}$	.0050(3)	0	0	0		neutrons	
	F	.21887(8)	.08606(7) or .41394	.45618(4)	.0104(2)	.0101(2)	.0110(2)	-.0033(1)	.0039(1)	-.0029(1)			
	Li	0	1/4	1/8	.0086(5)	$=U_{11}$	.0118(10)	0	0	0	175 K		
	Tb/Y	0	1/4	5/8	.0035(2)	$=U_{11}$	.0025(3)	0	0	0			
	F	.21914(8)	.08671(8) or .41329	.45623(4)	.0066(2)	.0066(2)	.0058(3)	-.0017(1)	.0019(1)	-.0013(1)			
$LiYbF_4$	Li	0	1/4	1/8	.020(7)	$=U_{11}$	.023(15)	0	0	0	room	MoKα	3.2
	Yb	0	1/4	5/8	.0073(1)	$=U_{11}$	.0029(1)	0	0	0		X-rays	
	F	.2166(6)	.4161(6)	.4564(3)	.013(1)	.011(1)	.008(1)	.0043(8)	.0033(9)	.0028(9)			

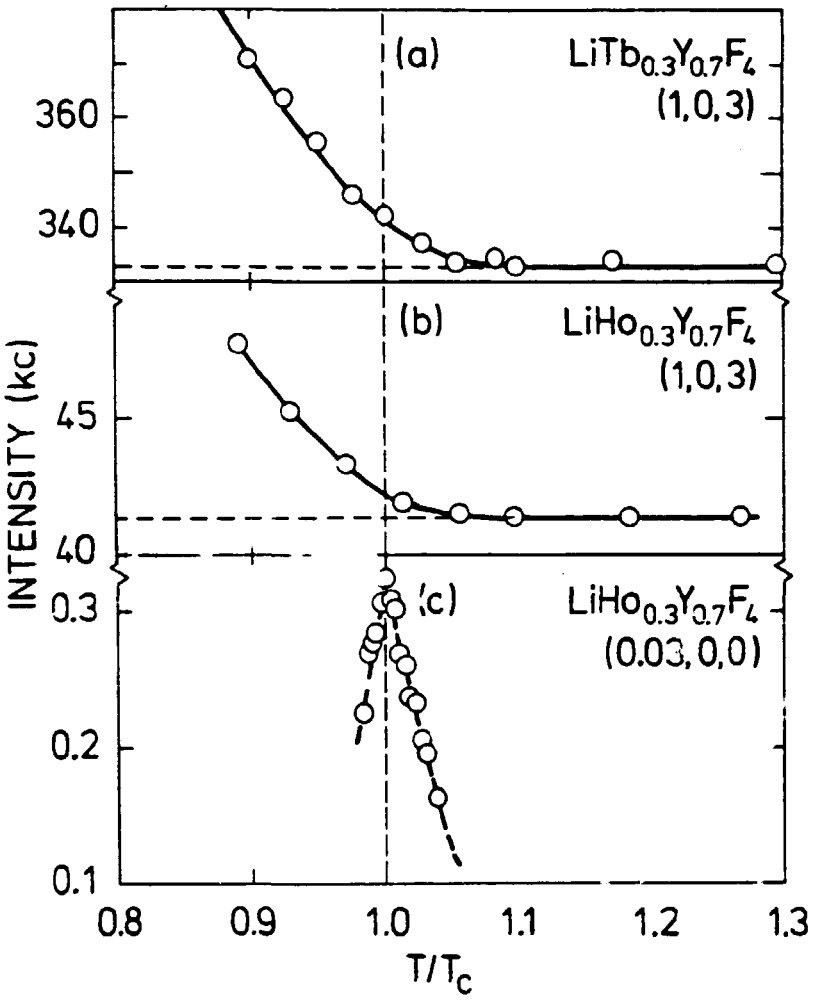

Fig. 3.3. Neutron intensity *vs.* reduced temperatures T/T_C.
a) (103) Bragg intensity from $LiTb_{.3}Y_{.7}F_4$, T_C = 0.493 K.
b) (103) Bragg intensity from $LiHo_{.3}Y_{.7}F_4$, T_C = 0.360 K.
c) Critical scattering from $LiHo_{.3}Y_{.7}F_4$ at (0.03·a*,0,0), T_C = 0.360 K.

3.3.5. Spontaneous magnetization

By means of double-axis neutron diffraction, the spontaneous magnetization versus temperature was measured. For a ferromagnetic crystal, the elastic cross-section at Bragg setting $\vec{Q} = \vec{\tau}_{hkl}$ is

$$\frac{d\sigma}{d\Omega} \propto F^2_{nuc} + F^2_{magn} \quad . \tag{3.33}$$

For unpolarized neutrons, there are no interference terms between the two contributions[3.70]. The nuclear structure factor is given by Eq. (3.32) above, and at the low temperatures relevant here, the thermal vibrations ($\bar{\bar{U}}$) can be set to zero. The magnetic contribution, which arises from the interaction between the magnetic moments of the neutron and the 4f-electrons, takes the form[3.70]

$$F^2_{magn} = \left| \frac{\langle \mu \rangle}{\mu_B} \cdot 2.7\text{fm} \cdot f\left(\frac{\sin\theta}{\lambda}\right) \cdot \sqrt{1 - \frac{\tau_z^2}{\tau^2}} \cdot p \cdot \sum_{j\ mag} e^{i\vec{\tau}\cdot\vec{r}_j} \right|^2 \qquad (3.34)$$

Here $\langle \mu \rangle$ is the magnetic moment per magnetic ion in the crystal, 2.7 fm is the magnetic scattering length per Bohr magneton, and the magnetic form factor f is the Fourier transform of the 4f-electronic magnetization density (spin and orbital contribution)[3.70]. The normalization is: $f(0) = 1$. f may be calculated for the free R^{3+} ions on the basis of self-consistent wavefunctions[3.71]. In a crystal, the crystal field gives rise to a form factor anisotropy which can be calculated in first-order perturbation theory[3.71]. As this effect is on the one per cent level, it will be ignored hre. The polarization factor $(1 - \tau_z^2/\tau^2)^{1/2}$ in Eq. (3.34) comes from the anisotropy of the dipolar interaction between the neutron and the 4f-electrons, and is written here for a Ising magnet. Finally, the geometrical structure amplitude of the R^{3+} sites ($\sum_{j\ mag}\ldots$) enters, weighted (under the $|\ |^2$ brackets) by the fraction p of spins present.

It follows from (3.33-3.34) that the magnetization may be found by measurement of the Bragg intensity above and below T_C,

$$\langle \mu \rangle_T / \mu_B = c \cdot (I(T)/I(T > T_C) - 1)^{1/2} \qquad (3.35)$$

This was done for $LiTb_{.3}Y_{.7}F_4$ using 13.9 meV neutrons and the (103) and (301) reflections. The very weak (103) reflection (see Table 3.6 below) is convenient because a relatively large ratio of magnetic to nuclear Bragg intensity is obtained. However, in the structure analysis, poor agreement was obtained

between the measured and refined intensities for the (103) and other weak reflections. Neither of these considerations apply to the stronger (301) reflection (Table 3.6). Consistent results were obtained with increasing and decreasing temperature, and the data from the two reflections could be scaled to fall on the same curve. Using 15.7 meV neutrons and the (103) reflection, the magnetization of the $LiHo_{.3}Y_{.7}F_4$ crystal was also studied. Here the rocking curve was measured many times at each mixer temperature setting until a constant intensity was obtained. Some raw data were shown in Fig. 3.3a&b, and Fig. 3.4 compares the magnetization data with those for $LiTbF_4$[3.3] and mean field theory. Apparent in the figure is the very slow saturation in the diluted crystals.

It is not known how much of the rounding of the intensity curve (Fig. 3.3) is critical scattering and how much results from a distribution of transition temperatures over the crystal. If no correction is applied, a pronounced rounding of the magnetization curve near T_C results (Fig. 3.4a). If all of the intensity above the nominal T_C is attributed to critical scattering and the data just below T_C are corrected, assuming that the critical scattering intensities are equal at $(T_C + \Delta T) > T_C$ and $(T_C - 1/2\ \Delta T)$ [3.72], magnetization curves with a vertical tangent at T_C are obtained (Fig. 3.4b). The values of the magnetization critical exponent β which result from this analysis are 0.47 ± 0.02 (Tb compound) and 0.48 ± 0.03 (HO compound.

Absolute values of the magnetic moment may also be derived, since the scale factor c in (3.35) is easily found from Eqs. (3.33-3.34),

$$c = \frac{|F_{nuc}|}{|2.7\ fm \cdot f \cdot \sqrt{1-\tau_z^2/\tau^2} \cdot p \cdot \sum_{j\ mag} e^{i\vec{\tau}\cdot\vec{r}_j}|} \qquad (3.36)$$

In Table 3.6 the c-values and the resulting magnetizations are displayed and compared with the data for the pure crystals.

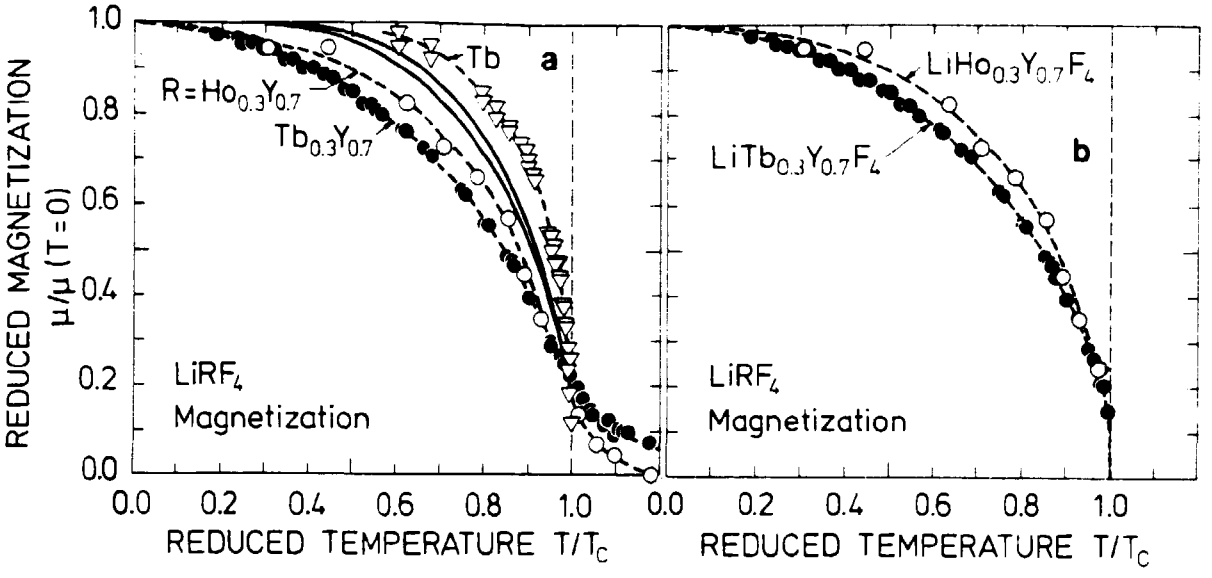

Fig. 3.4(a). Reduced magnetic moment versus reduced temperature for $LiRF_4$ crystals.
•, R = $Tb_{.3}Y_{.7}$
o, R = $Ho_{.3}Y_{.7}$
▽, R = Tb (from Ref. 3.3)
Broken lines are guides for the eye only. Full lines represent mean field theory (Appendix B).
Lower curve: $\Delta = 0$ (true doublet);
upper curve: $k\theta/(\Delta/2) = 1.3$ (two singlets).
(b): Magnetization curves for $LiTb_{.3}Y_{.7}F_4$ and $LiHo_{.3}Y_{.7}F_4$, corrected for critical scattering (see text).

Notable in the table is the 40% discrepancy in the $Tb_{.3}$ data and the 15% uncertainty in the $Ho_{.3}$ datum resulting from the scatter of data for the three Bragg points. The Poisson uncertainty is well below either of these values. The scale factor, c in Eq. (3.36), was calculated *for both crystals* using the structural parameters found for $LiTb_{.3}Y_{.7}F_4$ at 175 K (Table 3.5) and free-ion form factors from Ref. 3.71. Although c depends sensitively on the structure for the weak (103) reflection, the resulting uncertainty on c is estimated not to exceed 15% and is less for the stronger reflections. We discuss sources of error in the determination. Due to extinction, the measured intensity may in-

Table 3.6. Low-temperature magnetic moments. For $LiHo_{.3}Y_{.7}F_4$, the (103) reflection was measured *vs.* temperature, and at a few selected temperatures, the (301) and (305) reflections were measured in order to check on the scale of the magnetization, and the quoted uncertainty in μ derives from the scatter thus observed. The μ-values for $LiHoF_4$ are from g-factor measurements and from the saturation magnetization in a field.

	T_C K	hkl -	$\|F_{nuc}\|^2$ $10^{-24}cm^2$	c -	μ(T=o) μ_B	Ref.
$LiTb_{.3}Y_{.7}F_4$	0.493	103	0.212	4.08	3.6	This
	±.005	301	2.53	10.50	5.0	work
$LiTbF_4$	2.87	301 } 400 }			8.9	3.3
$LiHo_{.3}Y_{.7}F_4$	0.360	103	.359	5.16	4.6±.6	This
	±.002	301	2.99	10.60		work
		305	1.03	9.33		
$LiHoF_4$	1.55	(000)			6.7 - 7.0	3.6, 3.16, 3.17

crease less-than-proportionally to the cross-section, (3.33). This is difficult to address theoretically for the irregular sample shape used. However, extinction would tend to give a larger apparent magnetization from the weaker (103) reflection. Another source of error is multiple scattering. This would affect the weak reflection (103) most. and give lower apparent ionic moments.

In the structure determination, most of the weak reflections including the (103) were observed stronger than the refined structure factors, in evidence of multiple scattering. At the lower neutron energies used in the magnetization measurement, multiple scattering is less probable, but a calculation for the actual scattering geometries gave several reflections close to the Ewald sphere for the (103) spectrometer settings for the two diluted crystals. A quantitative correction has not been attempted, but

if, as in the structure analysis, the nuclear (103) intensity was enhanced as a result of multiple scattering, a too small magnetic moment would be derived.

In spite of these difficulties, the reduction of the T = 0 moments below those observed in the pure crystals (Table 3.6) is probably significant. Such a reduction is theoretically expected for the $LiTb_{.3}Y_{.7}F_4$ crystal (Fig. B.2 and $k\theta/(\Delta/2) = 1.6$ yields a 22% reduction in mean field theory), but for the Holmium compound we expect the ions to saturate completely at low temperature (unless the crystal field levels are different from those of the pure magnet, and in view of the evidence presented in Refs. 3.6-3.17 (see Section 3.2.2), this seems very unlikely). Thus, the apparent reduction needs to be understood theoretically, and on the experimental side, better data would be of value, either from bulk magnetization measurements or by neutron scattering (e.g., measuring many magnetic reflections from a small spherical sample). Temperatures down to the 0.100 K range or less are, however, needed for a reliable extrapolation to zero.

3.3.6. Critical scattering

In the study of phase transitions, the ability of diffraction methods to measure the spatial correlation of the fluctuations is of considerable value. In the case of magnetic systems, neutron diffraction remains the only technique available. The differential cross-section for diffuse magnetic scattering of thermal neutrons[3.37] by an Ising magnet is

$$\frac{d\sigma}{d\Omega d\omega} \propto \frac{k'}{k} (1 - Q_z^2/Q^2) \cdot S(\vec{Q},\omega) \ . \qquad (3.37)$$

Here, $\vec{k}$ and $\vec{k}'$ are the incident and final wave vectors corresponding to energies E and E'; $\vec{Q} = \vec{k} - \vec{k}'$ and $\hbar\omega = E-E'$ are the transfers of momentum and energy. S is the Fourier-transformed spin-spin correlation function

$$S(\vec{Q},\omega) \propto \int dt \sum_{\vec{r},\vec{r}'} e^{i\omega t}\, e^{i\vec{Q}\cdot(\vec{r}'-\vec{r})} \langle \hat{S}^z(\vec{r},\, t=o) \cdot \hat{S}^z(\vec{r}',t)\rangle_T \tag{3.38}$$

where the sum is over magnetic ion sites. Near a 2nd-order phase transition the scattering will be almost purely elastic[3.73]. Then, the intensity measured by a two-axis neutron diffractometer will be to a good approximation proportional to

$$\frac{d\sigma}{d\Omega} = \int d\omega \, \frac{d\sigma}{d\Omega d\omega} \propto (1 - Q_z^2/Q^2) \cdot S(\vec{Q}) \,, \tag{3.39}$$

$$S(\vec{Q}) \propto \sum_{\vec{r},\vec{r}'} e^{i\vec{Q}\cdot(\vec{r}'-\vec{r})} \langle \hat{S}^z(\vec{r},\, t=o)\, \hat{S}^z(\vec{r}',\, t=o)\rangle_T \tag{3.40}$$

$$\propto T \cdot \chi_T(\vec{Q}) \propto \chi_T(\vec{Q})/\chi_T^o \tag{3.41}$$

as derived in Ref. 3.37.

If dipolar interactions dominate the fluctuations in the diluted c ystals, this cross-section will be of the form (3.16) or (3.25) which, as mentioned in the preceeding paragraph, becomes extremely compressed in the c*-direction, corresponding to the super-diverging longitudinal correlation length, Eq. (3.16c). Thus, to measure the correlation function by two-axis neutron diffraction, very good resolution is needed, at least in the c*-direction. As shown by Als-Nielsen[3.31], the solution to this problem is to measure $\chi_T(\vec{Q})$ near the (000) Bragg point, i.e. by small-angle neutron scattering (SANS).

A SANS instrument is being developed[3.75] at the cold neutron source of the Risø DR3 reactor. This instrument will be ideally suited to measure the cross-section (3.25). As the instrument was still under construction at the time of the work reported on here, conventional double-axis diffractometers at the cold neutron source were used with tight Soller collimators (Fig. 3.5a).

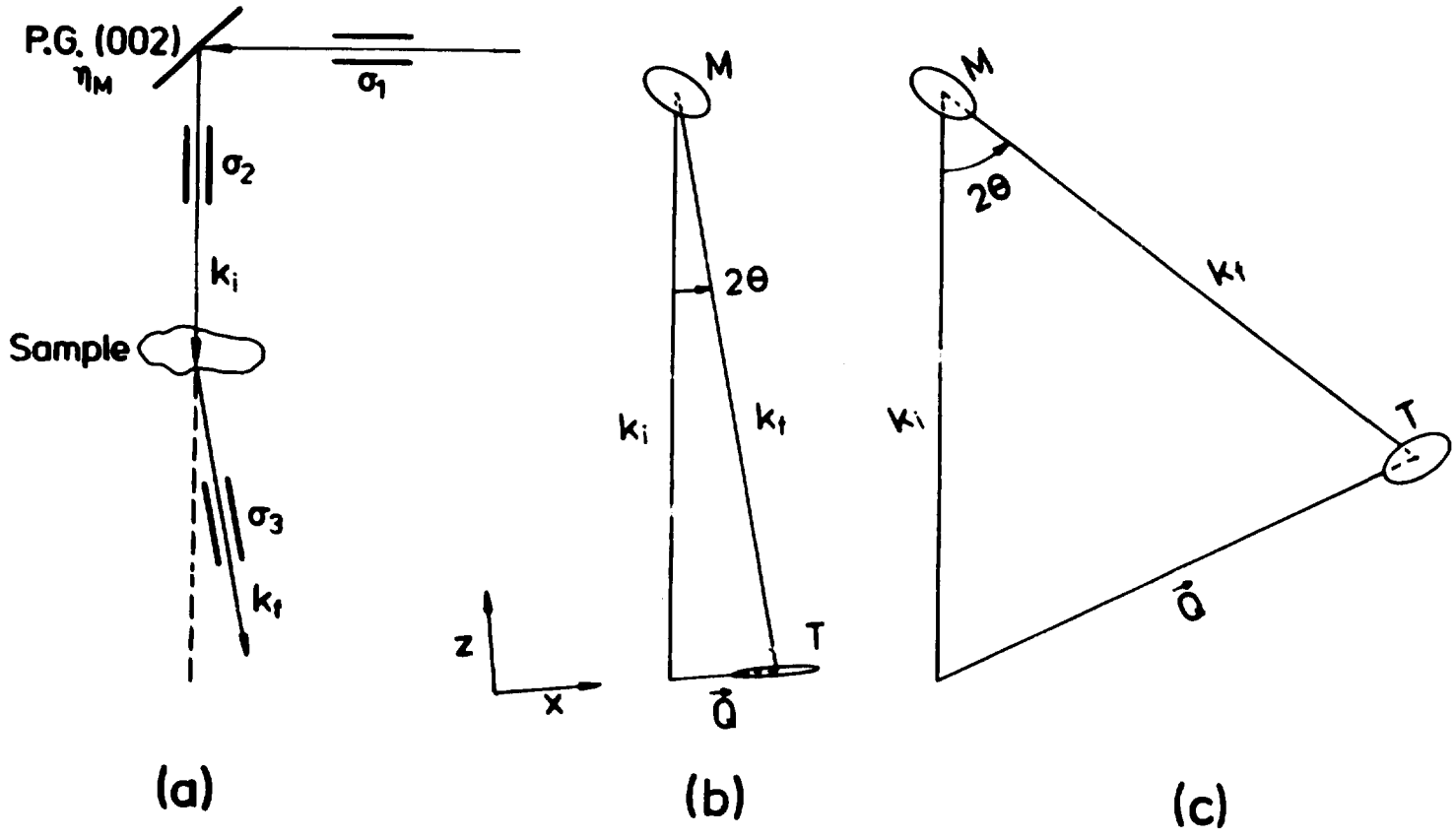

Fig. 3.5. a) Double-axis diffractometer in real space. η_M is the mosaicity of the (pyrolytic graphite) monochromator crystal, and σ_1-σ_3 are angular collimations. b, c) Scattering triangles for the sample. After the monochromatization, the neutrons have a spread in energy and direction (contours M). Assuming elastic scattering by the sample, the resulting $\vec{Q}$-resolution (contours T) is very much compressed in the small-angle case (b). In the calculation, the parameters of line two in Table 3.7 below were used. The resolution contours are shown x25 expanded relative to the scattering triangle.

Table 3.7. Instrument parameters in the critical scattering measurements. η_M and σ_1-σ_3 are defined in Figure 3.5, and R_x, R_y and R_z are the calculated dimensions (FWHM) of the resolution function R_z is proportional to the scattering vector Q. The calculated R_x values were in good agreement with the measured widths of the direct beam.

	monochromator	η_M	k $Å^{-1}$	E meV	σ_1	σ_2	σ_3	R_x $Å^{-1}$	R_y $Å^{-1}$	R_z/Q
$LiTb_{.3}Y_{.7}F_4$ TAS VI	PG(002) (flat)	30'	1.55	5.02	30'	10'	10'	0.0070	0.05	0.0023
$^7LiHo_{.3}Y_{.7}F_4$ TAS VII	"	30'	1.14	2.71	32'	14.4'	13.5'	0.0066	0.05	0.0029

Looking at Fig. 3.5b it is easy to see that although the neutrons incident on the sample have a spread in both energy and direction (contour M), the resulting $\vec{Q}$-vector resolution (contour T) must become narrow in the z-direction as the scattering angle $2\theta \to 0$, assuming only that the scattering is elastic.

Critical scattering from $LiTb_{.3}Y_{.7}F_4$ and $LiHo_{.3}Y_{.7}F_4$ was measured using the instrument parameters given in Table 3.7. Given in the table are also the calculated Gaussian resolution widths R_x, R_y and R_z, using the theory of Møller & Nielsen[3.74].

The background, as measured at high temperatures ($T > 2T_c$) has been subtracted in the data displayed below.

3.3.7. Critical scattering from $LiHo_{.3}Y_{.7}F_4$

Figure 3.6 shows data for $LiHo_{.3}Y_{.7}F_4$ just above T_c.

As seen in the figure, the scattering is very anisotropic. To see whether the dipolar cross-section 3.25 fits the data we need to convolute it with the calculated resolution function (Table 3.7), i.e. we compare the measured intensity with

$$I(\vec{Q}) = \int d^3\vec{Q}' \cdot R(\vec{Q}-\vec{Q}') \cdot \frac{d\sigma}{d\Omega}(\vec{Q}') \qquad (3.42)$$

$$\frac{d\sigma}{d\Omega}(\vec{Q}) = \frac{\sigma_o}{1+\xi^2\left(Q^2+g\left(\frac{Q_z}{Q}\right)^2\right)} \qquad (3.43)$$

The term hQ_z^2 from Eq. (3.25) has been omitted from (3.43) since it is negligible for the $\vec{Q}$ vectors in Fig. 3.6. $R(\vec{Q}-\vec{Q}')$ is a Gaussian of widths R_x, R_y and R_z (FWHM). Since, as seen in the figure, R_x and R_z are narrow compared with the features of the observed scattering, we may well put

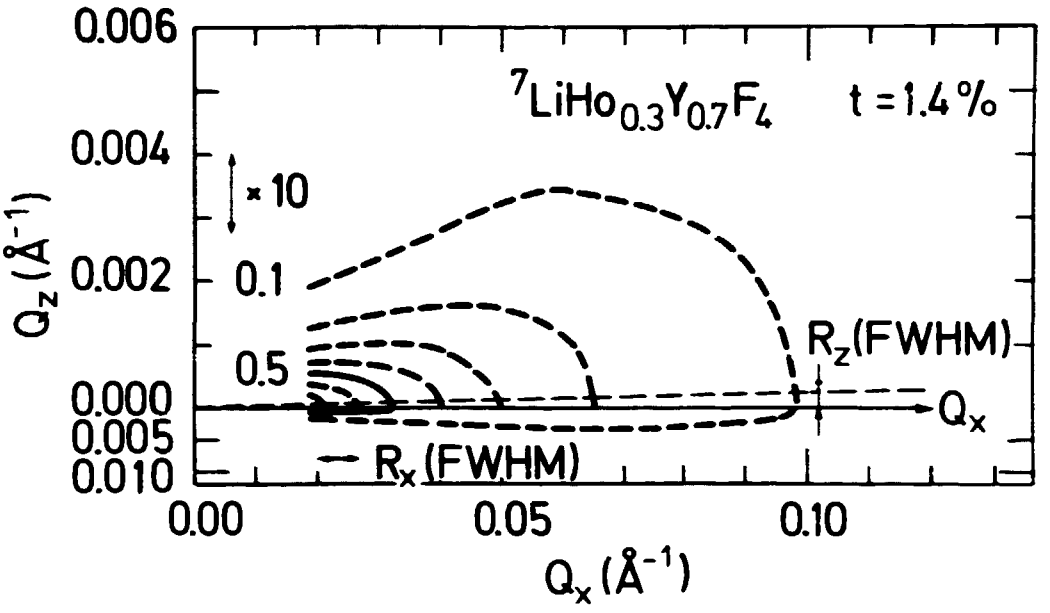

Fig. 3.6. Critical scattering from $^7LiHo_{.3}Y_{.7}F_4$ at 1.4% above T_C = 0.360 K. The intensity is normalized by the extrapolated maximum intensity $I_o = I(Q_z << Q_x \to 0)$ and contour lines are shown for I/I_o = 0.1 to 0.7 in steps of 0.1. Note the x10 expansion of the Q_z-scale in the upper part of the figure. Also shown are the calculated resolution widths $R_z \propto Q$ and R_x.

$$R(\vec{Q}-\vec{Q}') \propto \delta(Q_x-Q_x') \cdot \delta(Q_z-Q_z') \cdot e^{-\frac{4\ \ln 2\cdot(Q_y-Q_y')^2}{R_y^2}} \qquad (3.44)$$

retaining only the large vertical resolution width R_y. By fitting Eqs. (3.42-3.44) to intensities measured at Q_z = 0 we have extracted the correlation length ξ and the amplitude σ_o, which is proportional to the internal susceptibility $\chi(Q_z << Q_x \to 0)/\chi_T^o$. Subsequently, by fitting Eqs. (3.42-3.44) to full two-dimensional intensity distributions we have extracted values for the parameter g.

On axis data. Scans were made along the Q_x-axis in reciprocal space for several temperature settings. For the low counting rates obtained, the time needed for thermal equilibrium after small temperature changes was only a small fraction of the counting time. Figure 3.7 shows some of the data.

As seen in the figure, the line shape (3.42-4) fits the data quite well. The resulting χ squared (χ^2) for the fits are in the range 0.7-1.7, and the correlation length ξ and the extrapolated ($\vec{Q} \to 0$) cross-section σ_o may be extracted.

Two-dimensional data. The fingerprint of the dipolar cross-section (3.43) is the peculiar variation with Q_z. Full $I(Q_x, Q_z)$ intensity profiles were measured at two temperatures above T_c. Figure 3.8 shows again the data represented in Fig. 3.6 (T = 0.3650 K). Keeping σ_o and ξ fixed at the values derived from a $Q_z = 0$ cut in the data, the only adjustable parameter in (3.43) is the asymmetry parameter g. Allowing g to vary, the data are well represented by the dipolar cross-section.

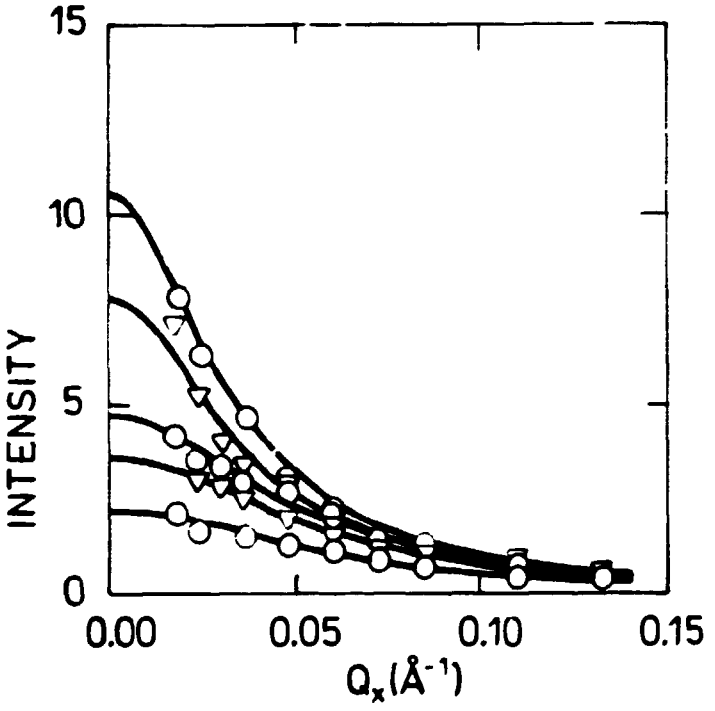

Fig. 3.7. Measured critical scattering $I(Q_x,0)$ from $^7LiHo_{.3}Y_{.7}F_4$ at temperatures T = 0.3650, 0.3674, 0.3705, 0.3733 and 0.3824 K (o,▽). The full lines are the best fits of the Lorentzian cross-section (3.43) convoluted with the vertical resolution (3.44).

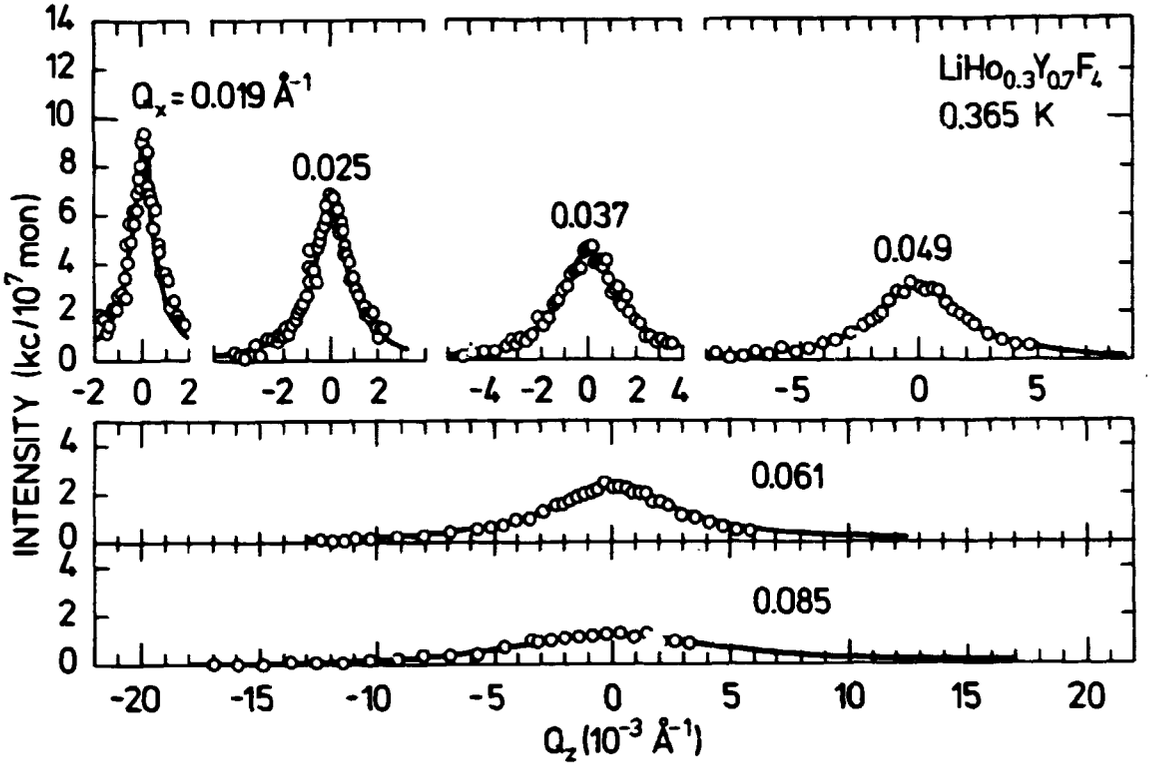

Fig. 3.8. Critical scattering $I(Q_x, Q_z)$ from $^7LiHo_{.3}Y_{.7}F_4$ at 0.3650 K ≈ T_C · 1,014 (•). The full lines are a simultaneous fit of Eq. (3.42-3.44) to all the data points, allowing only the asymmetry parameter g to vary.

One more data set $I(Q_x, Q_z)$ was obtained at a higher temperature (0.3824 K, not shown). The results of the fits are given in Table 3.8.

As was the case for $LiTbF_4$[3.31], g is changed somewhat from the mean field value as the phase transition is approached. The good fits of the dipolar cross-section to the data lead us to conclude that for $LiHo_{.3}Y_{.7}F_4$, the dipolar interaction between the spins is dominant and that the random dilution by the nonmagnetic yttrium ions has not changed the behaviour from that of the pure crystal other than by reducing the transition temperature.

Table 3.8. Results of fitting Eqs. (3.42-3.44) to the measured critical scattering $I(Q_x, Q_z)$ from $^7LiHo_{.3}Y_{.7}F_4$.

T (K)	$\frac{T-T_C}{T_C}$	g ($Å^{-2}$)	No. of points	χ^2 (-)
0.3650	1.4%	1.92±0.3	250	2.1
0.3824	6.2%	1.86±.10	54	1.6
mean field		1.57	-	-

Correlation length and susceptibility. Figure 3.9 shows the fitted, resolution corrected transverse correlation length squared ξ^2 (in the a-b plane) and compares it to the data for $LiTbF_4$ (Ref. 3.31) and to mean field theory. Apparent in the figure is that the correlation lengths observed in the holmium compound are larger (by a factor of ~ 2) than those of $LiTbF_4$, at the same reduced temperature. This effect may be understood in terms of the reduction of the transition points T_C below the values predicted by mean field theory, θ = 3.6 K for $LiTbF_4$ and, (scaling this number by the concentration and the magnetic moment), θ = 0.6 for $LiHo_{.3}Y_{.7}F_4$. Thus, T_C/θ = 0.80 and 0.60, respectively. Although long-range order does not occur till below T_C, the fluctuations at $T >> T_C$ are well described by mean-field theory, which predicts that the fluctuations will diverge at $T = \theta > T_C$. Thus, the fluctuations observed in the real physical system are enhanced when the transition temperature is suppressed as a result of, e.g., competing interactions[3.76]. It would be interesting to see if the large suppression of T_C in the randomly diluted magnet can be understood theoretically. For comparison, the mean field predictions are shown in the figure (dotted lines).

Figure 3.10 shows the extrapolated deconvoluted intensity at zero momentum transfer, σ_o, being proportional to the susceptibility, $\sigma_o \propto \chi_T(Q_z << Q_x \to 0)/\chi_T^o$. $\chi_T(0)/\chi_T^o$ may be found on an

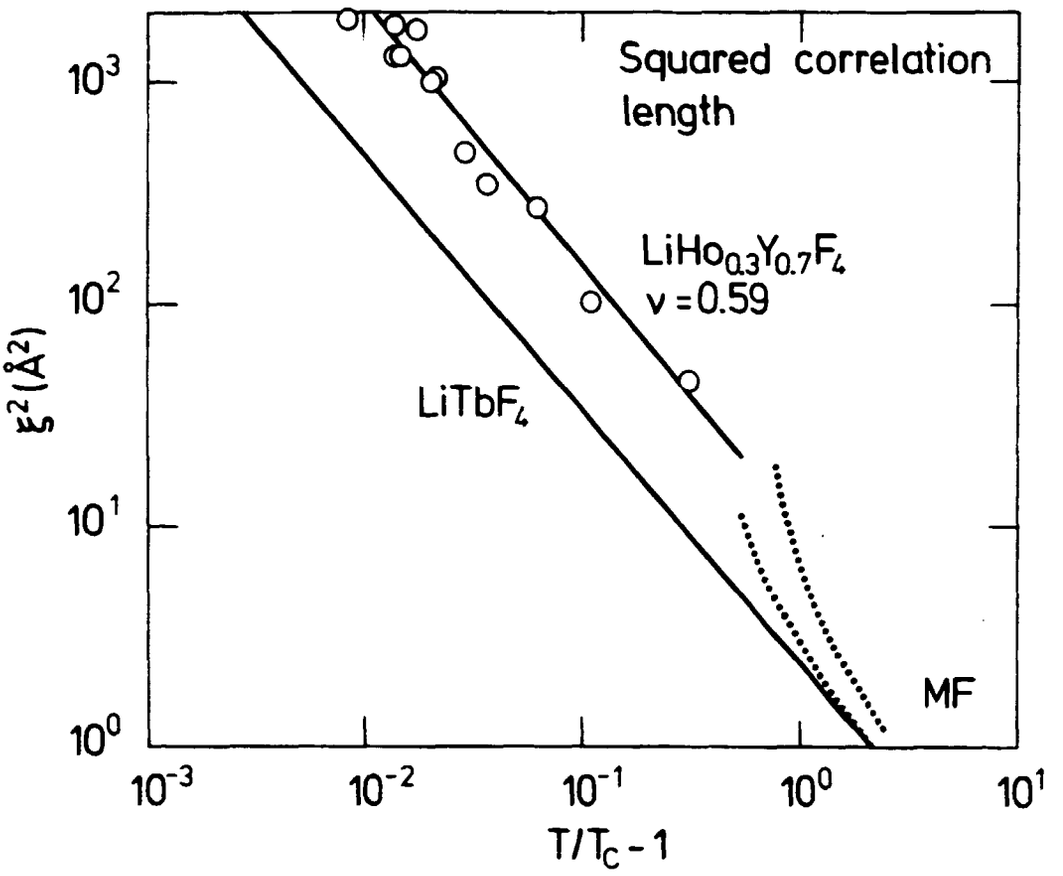

Fig. 3.9. Squared correlation lengths ξ^2 for $^7LiHo_{.3}Y_{.7}F_4$ (o), from $I(Q_x)$ scans corrected for the vertical resolution. Full lines are (upper curve) the best fit power law $\xi = \xi_o \cdot ((T-T_c')/T_c)^{-\nu}$, yielding $\nu = 0.59 \pm 0.02$ and $\xi_o^2 = 10$ Å^2; and (lower curve) the data for $LiTbF_4$ (Ref. 3.31). The dotted curves are the prediction of mean-field theory (MF), $\xi^2 = \xi_o^2 \cdot \theta/(T-\theta)$, with $\xi_o^2 = 1.37$ Å^2 and $\theta = 3.6$ K ($LiTbF_4$), resp. 0.60 K ($LiHo_{.3}Y_{.7}F_4$).

absolute scale by extrapolating to high temperatures, where $\chi_T(0)/\chi_T^o \to 1$. This extrapolation has been attempted for the $LiHo_{.3}Y_{.7}F_4$ data in the figure. However, since good data have not been obtained at very high temperatures, the extrapolation, and thus the scale of $\chi_T(0)/\chi_T^o$, is somewhat uncertain. In comparison with the data for $LiTbF_4$ (for which the extrapolation was performed with better accuracy) it is very plausible that the susceptibility (or fluctuation amplitude, Eq. (3.40)), is larger for $LiHo_{.3}Y_{.7}F_4$, in accordance with the results for the correlation length and with the argument given above.

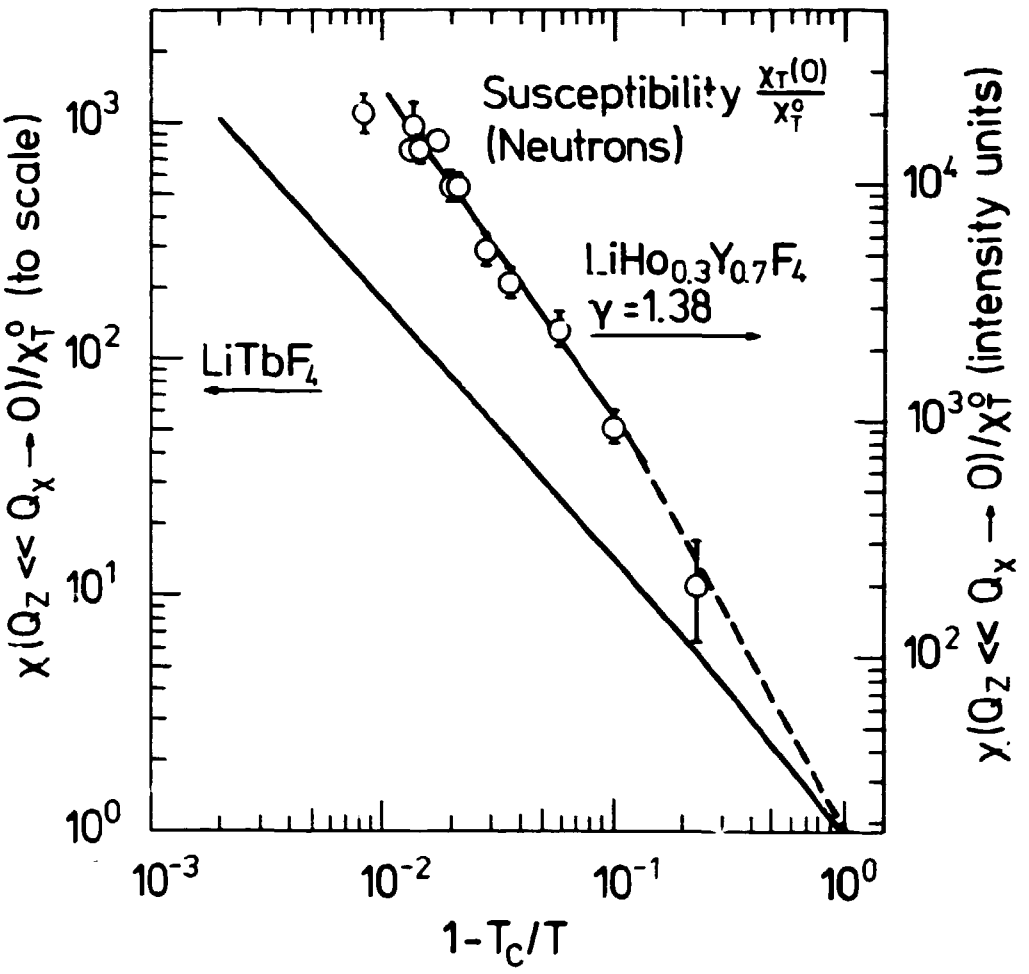

Fig. 3.10. Extrapolated susceptibility $\sigma_o (\propto \chi_T\ (Q_z << Q_x \to 0)/\chi_T^o)$ for $LiHo_{.3}Y_{.7}F_4$ (o) and $LiTbF_4$ (lower full curve; from Ref. 3.31). σ_o is given in intensity units (counts per 10^7 monitor counts; right-hand scale) χ/χ^o may be obtained to scale by extrapolation to high temperatures (left scale). This extrapolation is, however, uncertain for $LiHo_{.3}Y_{.7}F_4$ (broken line). The upper full line is a power law fit $\chi \propto (\Delta T)^{-\gamma}$, yielding $\gamma = 1.38 \pm 0.10$.

3.3.8. Critical scattering from $LiTb_{.3}Y_{.7}F_4$.

Figure 3.11 shows scattering data for $LiTb_{.3}Y_{.7}F_4$ just above T_C.

As for $LiHo_{.3}Y_{.7}F_4$, the scattering is very anisotropic. However, near the forward direction, for momentum transfers $Q_x < 0.03$ Å^{-1},

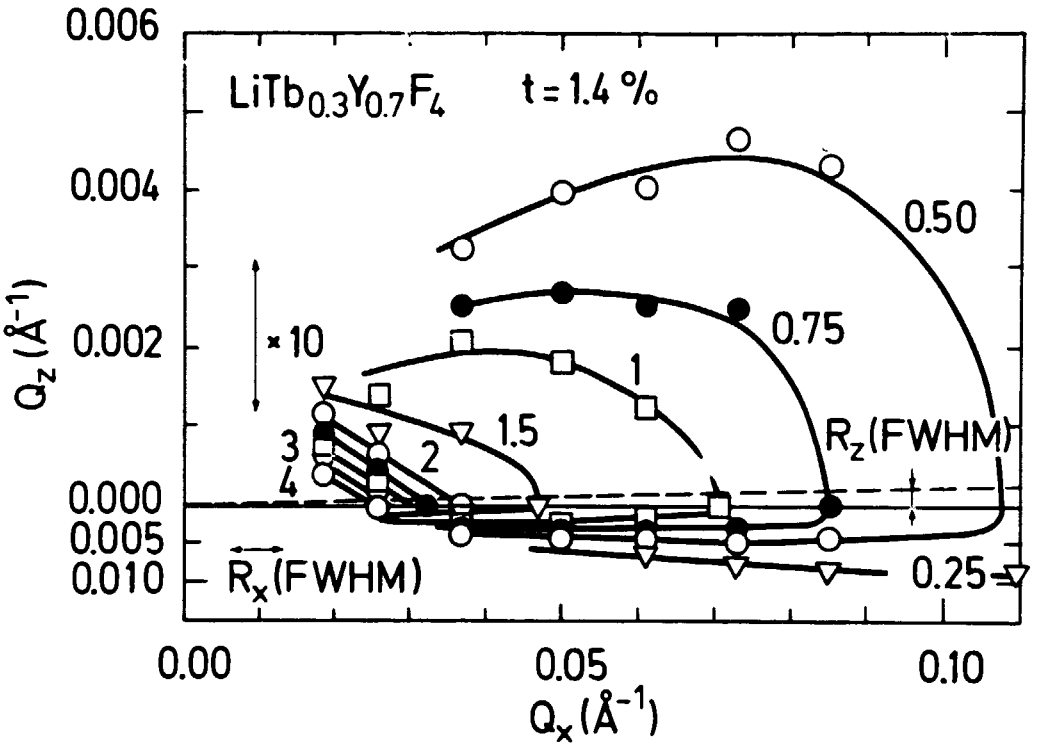

Fig. 3.11. Scattering $I(Q_x, Q_z)$ from $LiTb_{.3}Y_{.7}F_4$, at T = 0.500 K = 1.014 · T_C. Intensity, represented by contour lines, is in units of counts pe second. Note the x10 expansion of the Q_z scale in the upper part of the figure. Also shown are the calculated resolution widths (FWHM) $R_z \propto Q$ and R_x.

a sharp rise in the intensity is seen above that predicted by the cross-section (3.43). Qualitatively, similar features were observed at two higher temperatures. This is seen more clearly in Fig. 3.12 which represents data obtained *on axis* $I(Q_x, 0)$.

In the figure, the full lines are fits of simple Lorentzians, effectively representing the cross-section (3.43) convoluted with the vertical resolution. The extra intensity observed at low momentum transfers is indicated by the broken lines which are guides to the eye. The background (subtracted in the figure) was measured at high temperatures T ≈ 2 T_C and was of the order of 70-100% of the resulting signal close to T_C (upper-most curve in Fig. 3.12) for all momentum transfers. Errors in the background subtraction are estimated to be of the order of 15% for

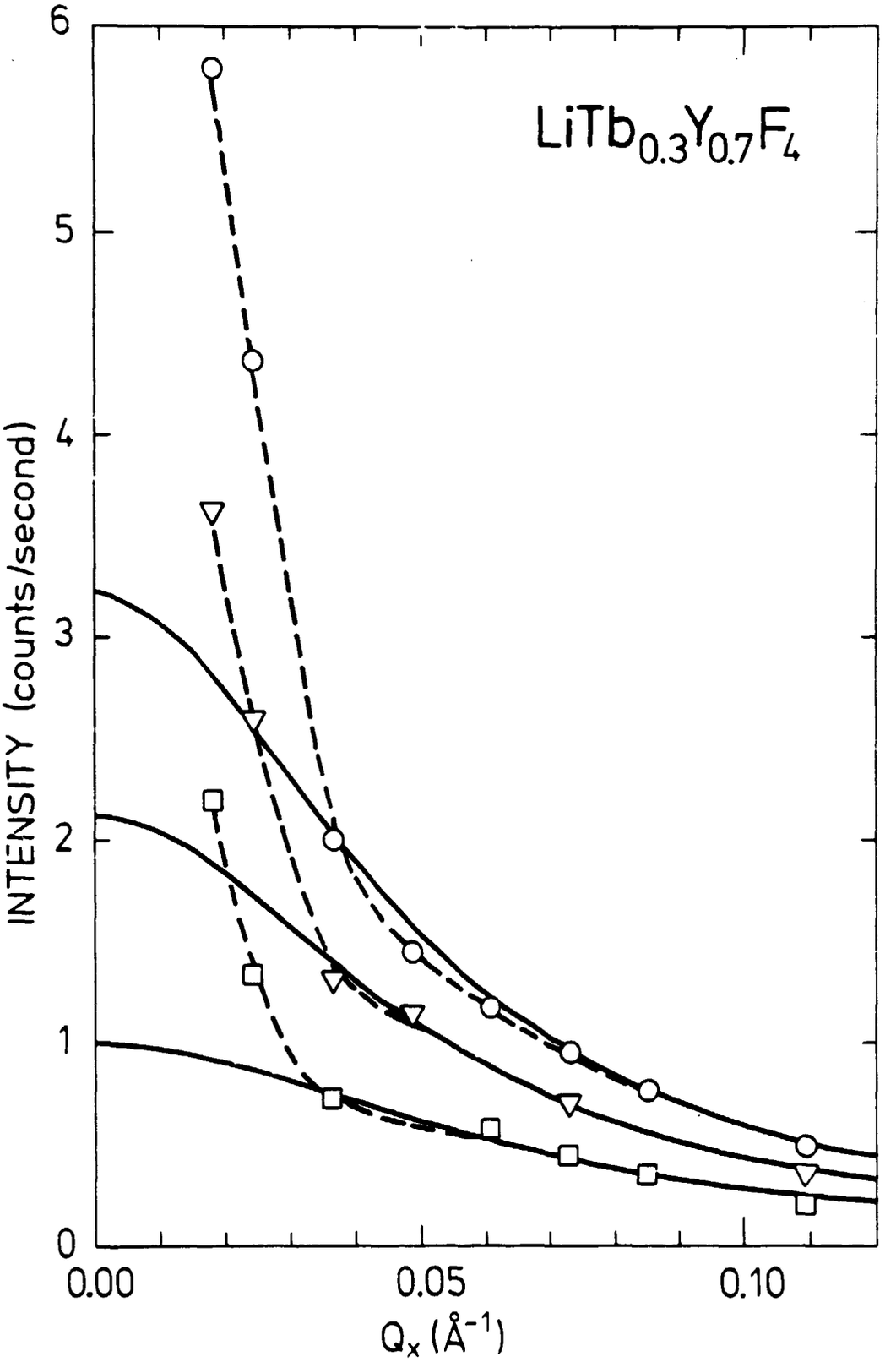

Fig. 3.12. Scattering $I(Q_x, 0)$ from $LiTb_{.3}Y_{.7}F_4$ in the paramagnetic phase (at temperatures 0.500 K ≈ 1.014 · T_C (o), 0.530 K ≈ 1.075 · T_C (▽) and 0.570 K ≈ 1.16 · T_C (□). Full lines are fits of Lorentzians (no resolution correction). Broken lines are guides to the eye.

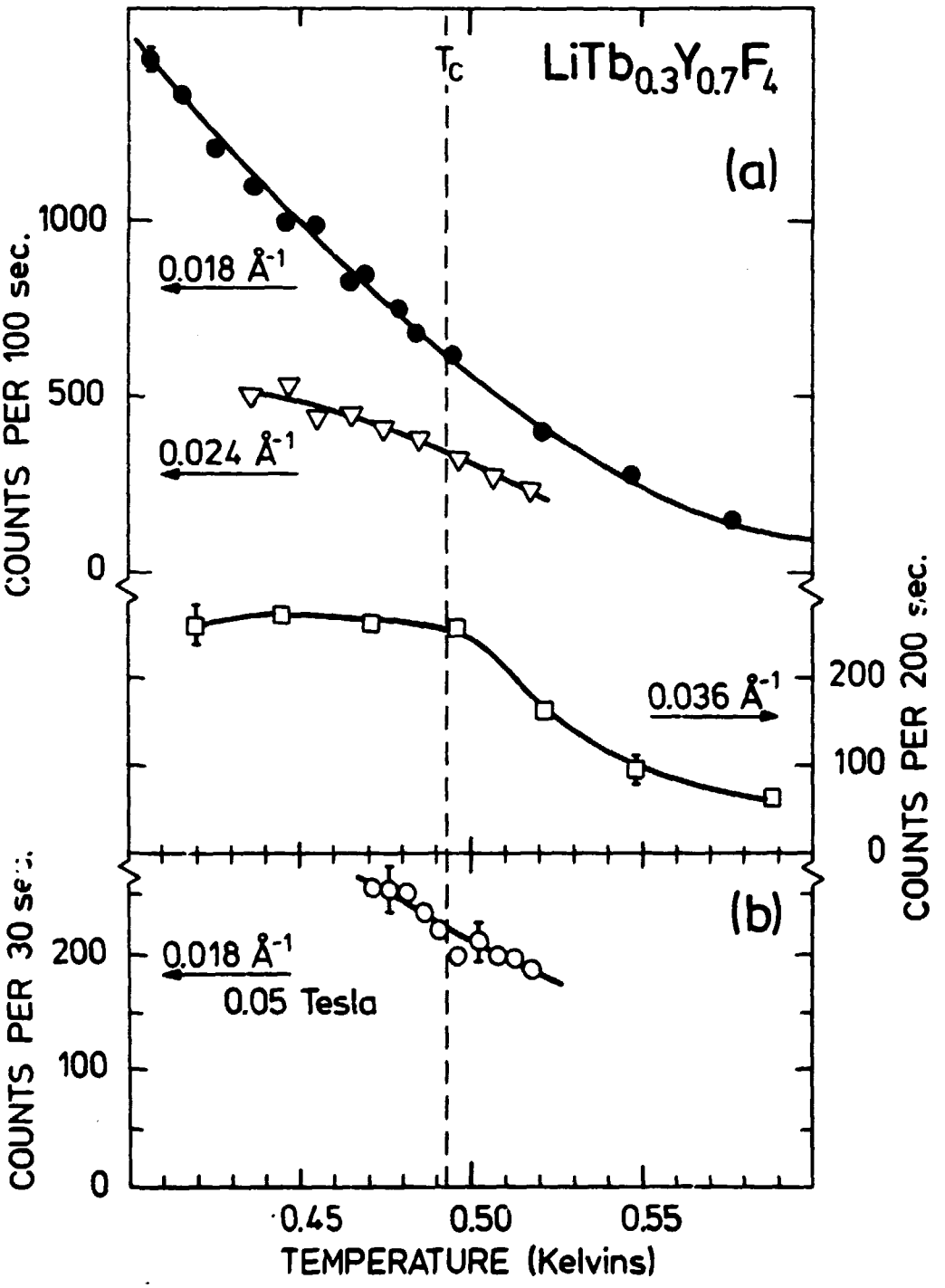

Fig. 3.13. Critical scattering from $LiTb_{.3}Y_{.7}F_4$ *vs.* temperature.

a) Scattering in zero field for $Q_z = 0$ and $Q_x = 0.018$ (●), 0.024(▽) and 0.036 Å^{-1} (□).

b) $Q_z = 0$, $Q_x = 0.018$ Å^{-1} and $B_{appl} = 0.05$ Tesla along the z (or c) axis. (o)

low momentum transfers $Q_x \approx 0.02$ Å^{-1} and less for the higher scattering angles.

The measured intensities in Fig. 3.12 obviously cannot be extrapolated to zero momentum transfer to give the susceptibility and the correlation length. If an extrapolation is made on the basis of the data for larger momentum transfers $Q_x > 0.03$ Å^{-1} (the [full line] Lorentzians in the figure), the resulting susceptibilities vary by only a factor of 3 and the correlation length ξ varies only from 16 to 21 Å, in going from 16% to 1.4% in reduced temperature $(T-T_C)/T_C$. A proper correction for the vertical resolution would not change this conclusion significantly.

The scattering was followed as a function of temperature above and below T_C at constant momentum transfers Q_x (Fig. 3.13(a)). A steady increase of intensity was observed even below T_C, no feature marking the transition point. For comparison, a significant peak at T_C was seen in the scattering from $LiHo_{.3}Y_{.7}F_4$ (Fig. 3.3) and $LiTbF_4$ (Ref. 3.31). In $LiTbF_4$, the intensity I(T) was observed to rise again when the temperature was lowered below *ca.* $0.99 \cdot T_c$[3.31]. This effect was attributed to scattering from magnetic domains and was seen to vanish in modest magnetic fields[3.32]. To check whether the observed scattering below T_C could be attributed to magnetic domains, we applied a field along the c-axis of the platelet-shaped sample. For the obtainable fields of 0.05-0.07 Tesla or less, no qualitative change in I(T) was observed, Fig. 3.13b. As this applied field would be sufficient to produce a nonzero internal field for magnetizations of 1 Bohr magneton per magnetic ion present, we may conclude that magnetic domain scattering is not the reason for the rising intensity below T_C.

3.4. Conclusion

The data presented for $LiTb_{.3}Y_{.7}F_4$ point to several anomalies in the physics of this system: The diffuse neutron scattering (Figs. 3.11 and 3.12), although exhibiting the a-symmetry pre-

dicted for a dipolar coupled system, possesses an anomalous component at small momentum transfers. Secondly, no distinct feature in the diffuse scattering marks the transition point (Fig. 3.13). Thirdly, the very slow saturation of the magnetic moment is notable (Fig. 3.4). Finally, the small magnetic moment (3.6-5 μ_B) reached at low temperatures is an interesting feature. It would be useful to confirm this result with greater precision by an independent method.

Theoretically, the observed behaviour cannot be explained at present, although it is plausible to speculate that the split ground state of the Tb ion is responsible in the presence of the dipolar interaction and the random dilution for producing the observed behaviour. The very different behaviour of the Ho system would seem to support this view.

Experimentally, a neutron study of the crossover from the well-understood $LiTbF_4$ scattering to the data presented here would be in order. As noted above, bulk susceptibility studies (Refs. 3.19-3.23) showed a continuously increasing deviation of the critical exponent γ from the mean field value of unity.

Next we consider the results for the $LiHo_{.3}Y_{.7}F_4$ system. Here it is apparent that the critical scattering (Figs. 3.6-3.8) above T_C is very well described by the cross-section (3.43), describing a dipolar coupled system. Also, T_C was marked by a peak in the scattering, as expected. For the parameters derived by fitting the cross-section (3.43) to the data, the correlation length (Fig. 3.9) and the susceptibility (Fig. 3.10), it is noticeable that the scale of the diverging quantities is much larger than predicted by mean field theory or observed for $LiTbF_4$. As discussed, this may be seen as a result of the significantly depressed transition temperature.

The critical exponent for the correlation length, $\nu = 0.59 \pm 0.02$, is quite close to the mean field value of $\nu = 1/2$, and the quality of the data does not permit to rule out the possibility of a mean-field-plus-small-corrections form such as Eqs. (3.26) or (3.30). In contrast, the susceptibility diverges ac-

cording to the power law $t^{-\gamma}$ with $\gamma = 1.38 \pm 0.10$, deviating significantly from any mean-field-like form. Concerning the magnetic moment, an unexpected slow saturation with temperature was observed as well as a reduced low-temperature magnetic moment.

Generally, the $LiHo_{.3}Y_{.7}F_4$ system thus seems to be better understood than its Tb counterpart. Even so, there is room for many more experiments: A basic assumption in the analysis presented here is that the concentrated Tb and Ho systems are equivalent. This seems to be borne out by bulk susceptibility and magnetization measurements, but a neutron diffraction experiment on $LiHoF_4$ would be of value. Also, a study of the $LiHo_pY_{1-p}F_4$ series by a variety of methods could help to complete the understanding of the diluted dipolar coupled Ising magnets.

References

3.1. THOMA, R.E., WEAWER, C.F., FRIEDMAN, H.A., INSLEY, H., HARRIS, L.A. and YAKEL, H.A. (1961) J. Phys. Chem. 65, 1096-99.

3.2. THOMA, R.E., BRUNTON, G.D., PENNEMAN, R.A. and KEENAN, T.K. (1970) Inorg. Chem. 9, 1096-1101.

3.3. ALS-NIELSEN, J., HOLMES, L.M., KREBS LARSEN, F. and GUGGENHEIM, H.J. (1975) Phys. Rev. B: Solid State 12, 191-97.

3.4. This work.

3.5. WYCKOFF, R.W.G. (1965) Crystal structures, 2nd ed., vol. 3, (Interscience, New York) § VIII a13, p. 19.

3.6. HANSEN, P.E., JOHANSSON, T. and NEVALD, R. (1975) Phys. Rev. B: Solid State 12, 5315-24. These authors quote $T_C = 1.30$ K for Ho, in contrast with the value $T_C = 1.50$-1.55 given by most authors.

3.7. LAURSEN, I. and HOLMES, L.M. (1974) J. Phys. C: 7, 3765-69.

3.8 SATTLER, J.P. and NEMARICH, J. (1971) Phys. Rev. B: Solid State 4, 1-5.

3.9. MAGARIÑO, J., TUCHENDLER, J., BEAUVILLAIN, P. and LAURSEN, I. (1980) Phys. Rev. B: Condens. Matter 21, 18-28.

3.10. BEAUVILLAIN, P., RENARD, J.P. and MAGARIÑO, J. (1980) J. Magn. Magn. Mater. 15-18, part 1, 31-32.

3.11. MAGARIÑO, J., TUCHENDLER, J., D'HAENENS, J.P. and LINZ, A. (1976) Phys. Rev. B: Solid State 13, 2805-8.

3.12. HOLMES, L.M., JOHANSSON, T. and GUGGENHEIM, H.J. (1973) Solid State Commun. 12, 993-97.

3.13. HOLMES, L.M., GUGGENHEIM, H.J. and ALS-NIELSEN, J. (1973) in: Trudy mezhdunnarodnoĭ konferentsii po magnetizum MKM-73. Vol. 6, 256-61. (Proceedings on the International Conference of Magnetism ICM-73).

3.14. GRIFFIN, J.A., LITSTER, J.D. and LINZ, A. (1977) Phys. Rev. Lett. 38, 251-54.

3.15. FROWEIN, R., KÖTZLER, J. and ASSMUS, W. (1979) Phys. Rev. Lett. 42, 739-42.

3.16. COOKE, A.H., JONES, D.A., SILVA, J.F.A. and WELLS, M.R. (1975) J. Phys. C: 8, 4083-8.

3.17. BATTISON, J.E., KASTEN, A., LEASK, M.J.M, LOWRY, J.B. and WANKLYN, B.M. (1975) J. Phys. C: 8, 4089-95.

3.18. GRIFFIN, J.A., HUSTER, M. and FOLWEILER, R.J. (1980) Phys. Rev. B: Condens. Matter 22, 4370-78.

3.19. BEAUVILLAIN, P., CHAPPERT, C., RENARD, J.P., GRIFFIN, J.A. and LAURSEN, I. (1980) J. Magn. Magn. Mater. 15-18, part 1, 421-23.

3.20. BEAUVILLAIN, P., CHAPPERT, C., RENARD, J.P. and GRIFFIN, J.A. (1980) J. Phys. C: 13, 395-401.

3.21. BEAUVILLAIN, P., SEIDEN, J. and LAURSEN, I. (1980) Phys. Rev. Lett. 45, 1362-65.

3.22. GRIFFIN, J.A., FOLKINS, J.J. and GABBE, D. (1980) Phys. Rev. Lett. 45, 1887-90.

3.23. FOLKINS, J.J., GRIFFIN, J.A. and GUBSER, D.U. (1982) Phys. Rev. B: Condens. Matter 25, 405-16.

3.24. HOLMES, L.M., ALS-NIELSEN, J. and GUGGENHEIM, H.J. (1975) Phys. Rev. B: Solid State 12, 180-90.

3.25. LORENTZ, H.A. (1916). The theory of electrons. 2nd ed. (Teubner, Leipzig).

3.26. BROWN, W.F. (1953) Rev. Mod. Phys. 25, 131-135.

3.27. GRIFFITHS, R.B. (1968) Phys. Rev. 176, 655-659.

3.28. LEVY, P.M. (1968) Phys. Rev. 170, 595-602.

3.29. COHEN, M.H. and KEFFER, K. (1955) Phys. Rev. 99, 1128-34.

3.30. COHEN, M.H. and KEFFER, K. (1955) Phys. Rev. 99, 1135-40.

3.31. ALS-NIELSEN, J. (1976) Phys. Rev. Lett. 37, 1161-64.

3.32. MØLLENBACH, K. (1980). Studies in small angle scattering techniques. Risø R-396. 99 p.

3.33. MISRA, S.K. and FELSTEINER, J. (1977) Phys. Rev. B: Solid State 15, 4309-12.

3.34. ALS-NIELSEN, J., HOLMES, L.M. and GUGGENHEIM, H.J. (1974) Phys. Rev. Lett. 32, 610-13.

3.35. BEAUVILLAIN, P., CHAPPERT, C. and LAURSEN, I. (1980) J. Phys. C: 13, 1481-91.

3.36. BEAUVILLAIN, P., RENARD, J.-P., LAURSEN, I. and WALKER, P.J. Phys. Rev. B: Condens. Matter 1978, 18, 3360-68 and J. Phys. Colloq. Orsay Fr. 1978, 39, C6, 745-46.

3.37. MARSHALL, W. and LOVESEY, S.W. (1971) Theory of thermal neutron scattering (Oxford University Press, London).

3.38. ALS-NIELSEN, J. (1976). Neutron scattering and spatial correlation near the critical point, in: Phase Transitions and Critical Phenomena, vol. 5. Edited by C. Domb and M.S. Green (Academic, London).

3.39. See, e.g. vol. 6 of Ref. 3.38.

3.40. See, e.g., ALS-NIELSEN, J. and BIRGENEAU, R.J. (1977) Am. J. Phys. 45, 554-560 or ALS-NIELSEN, J. and LAURSEN, I. in: Ordering in strongly fluctuating condensed matter systems. Edited by T. Riste (Plenum Press, New York) p. 222 (Nato Advanced Study Institutes Series: Series B, Physics, 50)
and
Nelson D.R. and Halperin, B.I. (1979). Phys Rev. B: Condens matter 19, 2457-84
and
references quoted in these papers.

3.41. This reproduces the argument given in Ref. 3.40.

3.42. LARKIN, A.I. and KHMEL'NITSKIJ, D.E. (1969) Zh. Eksp. Teor. Fiz. 56, 2087-98 (Engl. transl.: Sov. Phys. JETP 1969, 29, 1123-28).

3.43. AHARONY, A. and FISHER, M.E. (1973) Phys. Rev. B: Solid State 8, 3323-41.

3.44. AHARONY, A. Phys. Rev. B: Solid State, 1973, 8, 3363-70 and Phys. Rev. B: Solid State 1974:9:3946.

3.45. BERVILLIER, C. (1975) J. Phys. Letter Orsay Fr. 36, 225-28.

3.46. BRÉZIN, E. and ZINN-JUSTIN, J. (1976) Phys. Rev. B: Solid State 13, 251-54.

3.47. AHARONY, A. and HALPERIN, B.I. (1975) Phys. Rev. Lett. 35, 1308-10.

3.48. AHLERS, G., KORNBLIT, A. and GUGGENHEIM, H.J. (1975) Phys. Rev. Lett. 34, 1227-30.

3.49. AHARONY, A. (1976) Phys. Rev. B: Solid State 13, 2092-98.

3.50. HARRIS, A.B. (1974) J. Phys. C: 7, 1671-92.

3.51. STEPHEN, M.J. and AHARONY, A. (1980) J. Phys C. 14, 1665-70.

3.52. YOUNGBLOOD, R.W., AEPPLI, G., AXE, J.D. and GRIFFIN, J.A., (1982). Spin dynamics of a model singlet ground state system. BNL 31553.

3.53. SPEDDING, F.H. and DAANE, A.H. (editors) (1961). The rare earths, ch. 6 (Wiley, New York) 641 p.

3.54. Crystal growth attempts were made in collaboration with I. Laursen at the Technical University of Denmark, Lyngby, Denmark using his equipment and under his directions, and by I. Laursen alone. Also, the assistance of technician K. Pedersen and that of G.B. Jensen is gratefully acknowledged.

3.55. 4N (0.9999) purity anhydrous TbF_3 and HoF_3 was purchased from Rare Earth Products Ltd., England.

3.56. 6N purity anhydrous YF_3, same supplier.

3.57. Anhydrous ^7LiF was prepared by O. Jørgensen, Chemistry Dept., Risø Nat. Lab., on the basis of $^7Li_2CO_3$ purchased from Kock-Light Labs., England.

3.58. Purchased from Riedel - de Häen company.

3.59. I thank J. Lindbo and dr. J.B. Bilde-Sørensen, Metallurgy Dept., Risø Nat. Lab., for lending their equipment and expertise to this investigation.

3.60. Absolute quantitative analysis by this method requires a sample of known composition for comparison, as the correction for absorption and cross-section variations gives rise to systematic errors. (J.B. Bilde-Sørensen, private communication)

3.61. Thanks are due to M.H. Nielsen, Aarhus University and Risø, for running the diffractometer, to F. Krebs-Larsen, Aarhus Univ. who collaborated in the data analysis and to Rita Hazel, Aarhus Univ., for helpful discussions.

3.62. The set-up for low-temperature runs was described in: MERISALO, M., NIELSEN, M.H. and HENRIKSEN, K. (1973) Automatic low-temperature system for neutron four-circle diffractometer. Risø-R-279. 18 p.

3.63. LEHMANN, M.S. and LARSEN, F.K. (1974) Acta Crystallogr., Sect. A. 30, 580-84.

3.64. BACON, G.E. (1975) Neutron Diffraction, 3rd ed. table 6 (Clarendon, Oxford). 636 p.

3.65. ROUSE, K.D. and COOPER, H.J., YORK, E.J. and CHAKERA, A. (1970) Acta Crystallogr., Sect. A. 26, 682-91.

3.66. BECKER, P.J. and COPPENS, P. Acta Crystallogr., Sect. A. 1974, 30, 129-53; ibidem, 1975, 31, 417-25.

3.67. KELLER, C. and SCHMUTZ, H. (1965) J. Inorg. Nucl. Chem. 27, 900-01.

3.68. BACON, G.E. (1977) in: The Neutron Diffraction Newsletter. Edited by W.B. Yelon. Oxford University Press, London.

3.69. The dilution refrigerator has been constructed at Risø by John Z. Jensen.

3.70. Ref. 3.64, Chapters 6 & 15.

3.71. STASSIS, C., DECKMAN, H.W. HARMON, B.N., DESCLAUX, J.P., and FREEMAN, A.J. (1977) Phys. Rev. B: Solid State 15, 369-76.

3.72. This is the prediction of mean field theory and was found to apply for $LiTbF_4$ in Ref. 3.24.

3.73. Due to so-called critical slowing down. See, e.g., STANLEY, H.E. (1971) Introduction to phase transitions and critical phenomena, (Oxford University Press, London) 308 p.

3.74. MØLLER, H. BJERRUM, and NIELSEN, M. (1970) in: Instrumentation for neutron inelastic scattering research (IAEA, Vienna) p. 49-71; and Acta Crystallogr. Sect. A. 1969, 25, 547-50.

3.75. KJEMS, J.K., HEILMAN, I.U. and BAUER, R., unpublished.

3.76. LINDGÅRD, P.-A., private communication.

3.77. Thanks are due to dr.s A.M. Glazer, Oxford and Katarzyna Stadnicka, Krakow, for discussions on the Scheelite structure and help with preparation of the drawing.

4. CONCLUSION

Detailed conclusions for each of the two parts of the work reported have been given at the end of the suspective chapters. More generally, a large set of data has been presented for the CF_4 monolayers, demonstrating the existence of four 2D solid phases, including the "stripe" structure. Also, the phase transitions have been characterized.

For the diluted dipolar Ising magnets, neutron-scattering data have been presented for 30% concentration of Terbium and of Holmium ions. However, more data will be needed on tne $Li(Tb:Y)F_4$ and $Li(Ho:Y)F_4$ phase diagrams before a comprehensive understanding can be reached of the interplay of magnetic dipolar forces, randomness, and crystalline electric field in these systems.

ACKNOWLEDGEMENTS

Many people have made valuable contributions to this work. In particular, I should like to thank Dr. J. Als-Nielsen and M. Nielsen, M.Sc., for their guidance and encouragement. Also, thanks are due to other staff members at Risø for help and discussions, as well as to P. Bak and A. Aharony and to staff members at The Technical University of Denmark, at the Chemistry Department, Aarhus University and at the HASYLAB, DESY, Hamburg.

APPENDIX A

ON THE RADIATION FROM ULTRARELATIVISTIC ELECTRONS IN BENDING MAGNETS, WIGGLERS AND ONDULATORS

This appendix treats the radiation emitted by ultrarelativistic electrons in accelerators and storage rings while traversing bending magnets, wigglers and undulators. Detailed derivations are presented of the results given in the literature. Prior to the spectral analysis, the temporal evolution of the fields is studied, the method of calculation being non-quantum. The differences of the characteristics of the devices are emphasized. Perfect electron beam optics are assumed in the analysis.

Table of contents

A.1. Introduction

The synchrotron radiation from particles in accelerators, which was once considered a nuisance to high-energy physics, has now become an important tool of solid state physics. The characteristics - both of the synchrotron radiation proper, emitted from long bending magnets, and of the radiation from wigglers and undulators (arrays of alternating magnets) - are treated extensively in the literature.

This appendix gives derivations of the spectra etc., displaying the details of the calculations for the convenience of the reader. Also, the differences between the devices are addressed.

The following paragraph reviews the electromagnetic theory relevant to the problem, establishing in particular the system of units. Also some general characteristics of the radiation from ultrarelativistic charges are derived. Paragraph 3 is concerned with particles in one bending magnet and emphasizes the distinction between a "long" and "short" magnet. The fourth paragraph considers a wiggler made by an array of such homogeneous magnets and paragraph 5 treats in detail the case where the magnetic field is tapered so as to produce a sinusoidal trajectory.

A.2. The radiation by accelerated charges. General considerations

A.2.1. Units and fundamental equations

MKSA units are employed. In this system, the Maxwell equations read

$$\begin{aligned} \vec{\nabla} \times \vec{E} &= - \dot{\vec{B}} \\ \vec{\nabla} \times \vec{H} &= \vec{J} + \dot{\vec{D}} \\ \vec{\nabla} \cdot \vec{D} &= \rho \\ \vec{\nabla} \cdot \vec{B} &= 0 \end{aligned} \qquad \text{(A.2.1)}$$

$\vec{E}$ being the electric field, $\vec{H}$ the magnetic field, $\vec{D}$ the dielectric displacement density, $\vec{B}$ the magnetic induction density, $\vec{J}$ the density of current and ρ that of charge. In a vacuum the fields are connected by the equations

$$\vec{D} = \varepsilon_o \vec{E} \quad , \quad \vec{B} = \mu_o \vec{H} \quad ,$$

$$\mu_o = 4\pi \cdot 10^{-7} \text{ Vs/Am} \quad , \quad \mu_o \varepsilon_o c^2 = 1 \quad ,$$

c denoting the velocity of light. The Poynting vector, giving the power per unit area transported by the field is

$$\vec{S} = \vec{E} \times \vec{H} = \mu_o^{-1} \vec{E} \times \vec{B} \; .$$

For reference we give also the classical electron radius, the fine-structure constant and the Bohr magneton in these units:

$$r_e = \frac{e^2}{4\pi\varepsilon_o mc^2} \approx 2.82 \cdot 10^{-15} \text{ m} ,$$

$$\alpha_f = \frac{e^2}{4\pi\varepsilon_o \hbar c} \approx (137.04)^{-1} ,$$

$$\mu_B = \frac{e\hbar}{2m} \approx 0.927 \cdot 10^{-23} \text{ Am}^2 ,$$

the electronic charge and mass being (-e) and m.

When the source of the field is a moving point charge q, in terms of the variables defined in Fig. A.2.1 the Liénard-Wiechert solution (Ref. A.1, § 14.1) reads:

$$\vec{E}_{rad}(\vec{r}_o,t) = \frac{q}{4\pi\sqrt{\varepsilon_o/\mu_o}} \left[\frac{\vec{a}}{\kappa^3 R}\right](t') ,$$

$$\vec{B}_{rad}(\vec{r}_o,t) = c^{-1}\, \hat{n}(t') \times \vec{E}(\vec{r}_o,t) , \qquad (A.2.2)$$

with

$$\vec{a}(t') \equiv \left[\hat{n} \times ((\hat{n} - \vec{\beta}) \times \dot{\vec{\beta}})\right](t') . \qquad (A.2.3)$$

Omitted in (A.2.2) are terms of order $1/R^2$, since only the term retained represents a field carrying power away. This is seen from the Poynting vector which falls off only as $1/R^2$:

$$\vec{S}(\vec{r}_o,t) = \frac{1}{c\mu_o} \cdot |\vec{E}(\vec{r}_o,t)|^2 \cdot \hat{n}(t')$$

$$= \frac{q^2}{4\pi c 4\pi\varepsilon_o} \left[\frac{a^2}{\kappa^6 R^2}\right](t') \qquad (A.2.4)$$

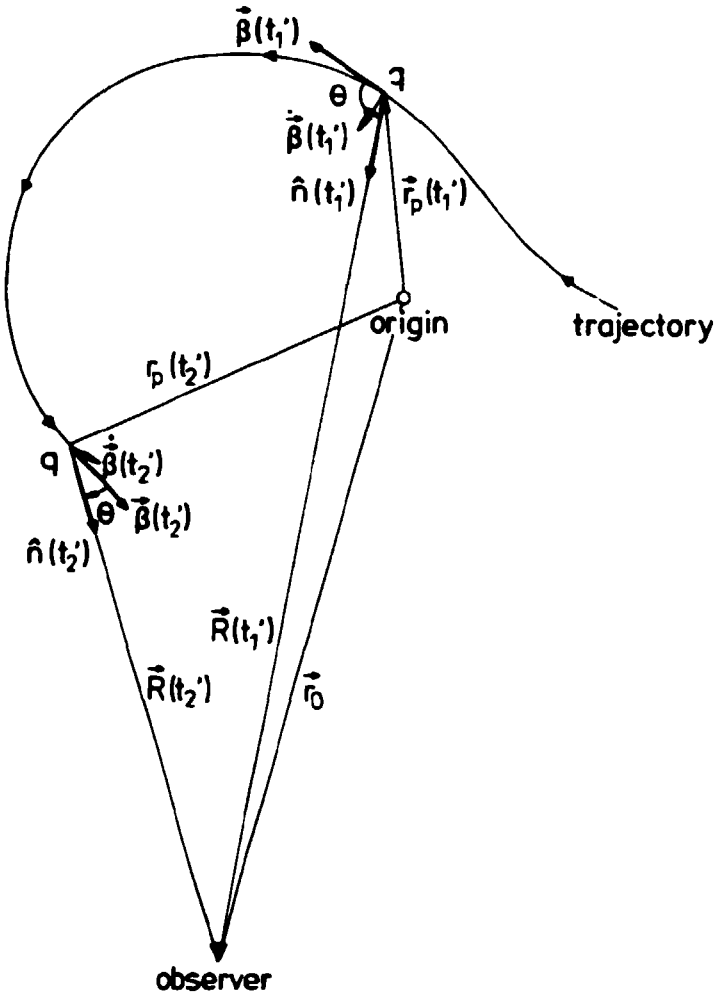

Fig. A.2.1. The geometry of the point charge problem. The variables of the Liénard-Wiechert solution, some of which are shown in the figure, are the following:

Vacuum: Parameters ε_o, μ_o, $c \equiv (\varepsilon_o \mu_o)^{-1/2}$.

Particle: Charge q.

Trajectory	$\vec{r} = \vec{r}_p(t')$.
Normalized velocity	$\vec{\beta}(t') = c^{-1} \cdot (d/dt')\vec{r}_p(t')$.
Normalized acceleration	$\dot{\vec{\beta}}(t') = e^{-1} \cdot (d^2/dt'^2)\vec{r}_p(t')$.

Observer: $\vec{r} = \vec{r}_o$, all t.

(continued on next page)

Text to Fig. A.2.1 continued

Particle to observer: Connecting vector $\vec{R}(t') = \vec{r}_o - \vec{r}_p(t')$.

Distance $R(t') = |\vec{R}(t')|$.

Unit vector $\hat{n}(t') = \vec{R}(t')/R(t')$.

Retardation: Radiation emitted at time t' reaches the observer at the retarded time

$$t = t' + c^{-1} \cdot R(t').$$

The derivative of this is the "slope":

$$\kappa \equiv dt/dt' = 1 - \hat{n}(t') \cdot \beta(t').$$

A.2.2. The field from an ultrarelativistic particle

In terms of the usual normalized velocity

$$\beta = |\vec{\beta}| = \frac{1}{c} |\vec{dr}/dt'| ,$$

the ultrarelativistic case is defined by the inequalities

$$\gamma \equiv (1 - \beta^2)^{-1/2} = \frac{E_e}{mc^2} >> 1 ,$$

$$1 - \beta \cong \frac{1}{2\gamma^2} << 1 .$$

Referring again to Figure A.2.1, we get for the "slope"

$$\kappa = dt/dt' = 1 - \beta\cos\theta \approx \frac{1}{2\gamma^2} (1 + \gamma^2\theta^2) . \qquad (A.2.5)$$

From (A.2.5) two conclusions are drawn:

(i) It is seen from (A.2.4) that the emitted radiation will be sharply peaked in the forward direction. Indeed most of the radiation is emitted in a cone of an angular width of several $\times(1/\gamma)$ around the forward direction.

(ii) If the particle emits radiation during a time $\Delta t'$ without changing its direction very much, ther. the radiation illuminates an observer standing at an angle θ from the forward direction during a time interval of only

$$\Delta t = \kappa \cdot \Delta t' = \frac{\Delta t'}{2\gamma^2}(1 + \gamma^2\theta^2) \ . \qquad (A.2.6)$$

Of course, the frequencies of the signal are shifted by the reciprocal factor:

$$\omega_{typ} = \omega'_{typ}/\kappa = \omega'_{typ} \cdot \frac{2\gamma^2}{1+\gamma^2\theta^2} \ . \qquad (A.2.7)$$

As will be seen in the next paragraph this Doppler-like mechanism is in part responsible for the high frequencies observed in the synchrotron radiation.

It is instructive to rederive the results (i) and (ii) by some elementary reasoning in a frame of reference K^+ in which the particle is momentarily at rest. To be specific, in the laboratory frame K let

$$\vec{r}_p(t' = 0) = \vec{0},$$

$$\vec{\beta}(t' = 0) = \hat{z}\beta^+ \ ,$$

so that

$$x(t'),\ y(t') = 0 + \text{order}((t')^2) \ ,$$
$$z(t') = \beta^+ t' + \text{order}((t')^2) \ ,$$

and let frame K^+ move uniformly with the same velocity $\beta^+\hat{z}$ re-

lative to K. The description in K^+ of the movement of the particle is obtained by a Lorentz transformation:

$$
\begin{aligned}
x^+ &= x,\ y^+ = y\ , \\
z^+ &= \gamma\ (z - \beta^+\ ct'), \\
t'^+ &= \gamma\ (t' - \beta^+\ z/c), \\
\gamma &= (1 - (\beta^+)^2)^{-1/2}\ ,
\end{aligned}
$$

yielding, of course,

$$
\begin{aligned}
x^+ &= x_p(t') = 0 + \text{order}((t'^+)^2), \\
y^+ &= y_p(t') = 0 + \text{order}((t'^+)^2), \\
z^+ &= \quad\ 0 + \text{order}((t'^+)^2), \\
t'^+ &= \quad\ t'/\gamma .
\end{aligned}
$$

Now, in K^+ the movement is momentarily non-relativistic, and the radiation caused by it is well-known (and follows from (A.2.2-4): The power flux is

$$
\vec{S}^+ = \frac{q^2(\dot{\vec{\beta}})^2}{(4\pi R)^2 c\varepsilon_o}\ \sin^2\psi\ \hat{n}\ ,
$$

ψ being the angle between $\hat{n}$ and $\dot{\vec{\beta}}$. This is a simple dipole pattern. The transformation of time intervals and frequencies follows from the Lorentz transformation:

$$
\Delta t'^+ = \Delta t'/\gamma\ ,\quad \omega'^+_{typ} = \omega'_{typ} \cdot \gamma\ , \tag{A.2.7'}
$$

and, since the particle is momentarily unrelativistic in K^+, the same frequencies are seen by an observer here, i.e., $\Delta t^+ = \Delta t'^+ = \Delta t'/\gamma$, $\omega^+_{typ} = \omega'_{typ} \cdot \gamma$. (A.2.7') is the usua time-dilatation. To get back to frame K we must transform both the frequencies and the direction of propagation (the wave-vectors) by a relativistic Doppler-transformation (as derived in § 11.4 of Ref. A.1): The frequencies observed in K are given by

$$
\omega = \frac{1/\gamma}{1-\beta^+\cos\theta}\ \omega^+ = \frac{1/\gamma}{\kappa}\ \omega^+ = \frac{\omega'}{\kappa} \tag{A.2.8}
$$

where θ is still indicated in Fig. (A.2.1). The corresponding angle θ^+ in K^+ is related to θ by the equation

$$\tan\theta = \frac{\sin\theta^+}{\gamma(\cos\theta^+ + \beta^+)} \ . \qquad \text{(A.2.9)}$$

Thus, all directions of propagation in K^+ (except for the "backward cone" $\theta^+ = \pi$) are concentrated - in K - in the "forward cone" $\theta \simeq 0$ of width $\sim 1/\gamma$. In conclusion, by a line of reasoning relying on a knowledge of relativity and not on a detailed study of the Liénard-Wiechert solution (A.2.2-4) we have confirmed the observations (i) and (ii) above.

We conclude the paragraph by noting a few more results which will be needed. The rate of emittance of energy in all directions (the power) is (Ref. A.1, § 14.2)

$$P = \frac{2}{3}\frac{q^2}{4\pi\varepsilon_o}\frac{1}{c^3 m^2}\gamma^2\left(\left(\frac{d\vec{p}}{dt'}\right)^2 - \frac{1}{c^2}\left(\frac{dE_e}{dt'}\right)^2\right) ,$$

$$P = \frac{2}{3}\frac{q^2}{4\pi\varepsilon_o}\frac{1}{c^3 m^2}\frac{dp_\mu}{d\tau}\frac{dp_\mu}{d\tau} \quad \text{(sum over } \mu) \qquad \text{(A.2.10)}$$

in terms of the four-momentun

$$\underset{\sim}{p} = (p_\mu) = (\vec{p},\ iEe/c)$$

and the particle's proper time

$$d\tau = dt'/\gamma \ .$$

This becomes, using frame-dependent quantities,

$$P = \frac{2}{3}\frac{q^2}{4\pi\varepsilon_o}\gamma^6\left(|\dot{\vec{\beta}}|^2 - |\vec{\beta}\times\dot{\vec{\beta}}|^2\right) . \qquad \text{(A.2.11)}$$

Using (A.2.10) or (A.2.11) and Newton's law,

$$\vec{F} = d\vec{p}/dt' = (d/dt')(mc\gamma\vec{\beta}) ,$$

one can express the power in terms of the applied forces along the velocity and perpendicular to it:

$$P = \frac{2}{3}\frac{q^2}{4\pi\varepsilon_o}\frac{1}{m^2c^3}\left(F_{||}^2 + \gamma^2 F_{\perp}^2\right) . \qquad (A.2.12)$$

Thus, for comparable components of force applied to a hyper-relativistic particle, the parallel component may safely be ignored in calculating the radiation. Incidentally, in terms of components of acceleration things look different:

$$P = \frac{2}{3}\frac{q^2}{4\pi\varepsilon_o}\frac{1}{c}\cdot\gamma^4\left((\dot{\beta}_{||})^2\cdot\gamma^2 + (\dot{\beta}_{\perp})^2\right) . \qquad (A.2.13)$$

However, comparable components of force is the more realistic assumption.

A.3. The "synchrotron radiation" from an ultra-relativistic electron in a bending magnet

This is the classical problem, treated by (among others) Refs. A.2 and A.3 and in the text book by Jackson (Ref. A.1). The calculations are given in some detail below.

A.3.1. Preliminary calculations

The most interesting radiator is an electron, of charge q = (-e). In a homogenous magnetic field B, the radius of curvature will be

$$\rho = \frac{mc\gamma}{B\cdot e} = \frac{E_e}{cBe} = 3.33 \text{ meters} \cdot \frac{E_{e/GeV}}{B/Tesla} .$$

Specifically, in terms of orthogonal unit vectors $(\hat{x},\hat{y},\hat{z})$, let the *trajectory* be

$$\vec{r}_p(t') = \hat{x}\rho \sin\frac{c\beta t'}{\rho} + \hat{y}\rho\left(1 - \cos\frac{c\beta t'}{\rho}\right) ,$$

$$\vec{\beta} = \hat{x}\beta \cos\frac{c\beta t'}{\rho} + \hat{y}\beta \sin\frac{c\beta t'}{\rho} ,$$

$$\dot{\vec{\beta}} = -\hat{x}\frac{c\beta^2}{\rho}\sin\frac{c\beta t'}{\rho} + \hat{y}\frac{c\beta^2}{\rho}\cos\frac{c\beta t'}{\rho} ,$$

as shown in Fig. A.3.1; and without loss of generality, let the *observer* be in the x-z plane, at an angle θ from the x-y-plane (orbit plane) - and at a very large distance r_o from the ring.

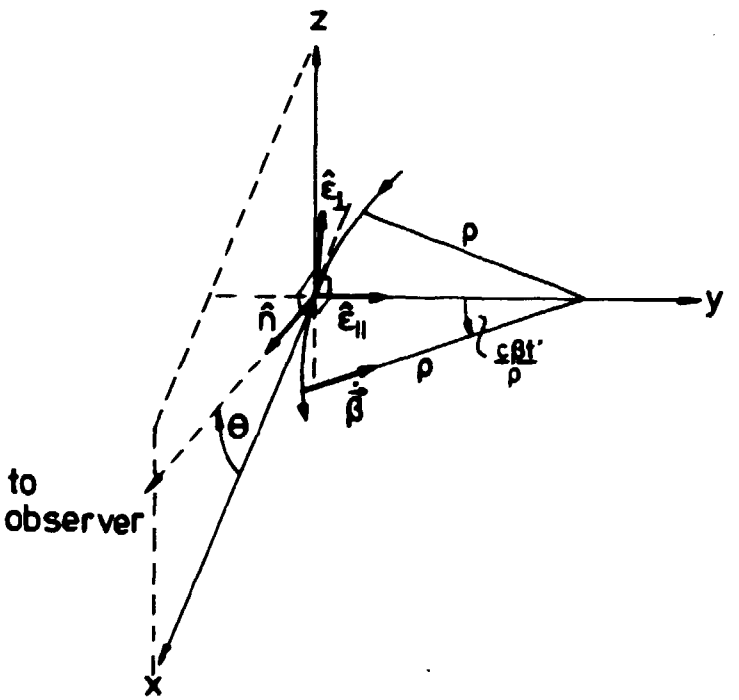

Fig. A.3.1. The geometry of the bending magnet problem. The setting of Ref. A.1 is used.

Then, since the radiation is concentrated in the "forward cone", only angles $\theta \lesssim 1/\gamma$ will be relevant, and likewise, only a segment of the trajectory such that

$$\beta ct'/\rho \lesssim 1/\gamma \qquad \text{(A.3.1)}$$

will contribute to the observed field. This will allow for some approximations.

The *unit vector* from electron to observer is constant (since $r_o >>$ everything),

$$\hat{n} = \hat{x} \cos\vartheta + \hat{z} \sin\vartheta,$$

and the *distance* the light must travel is

$$R(t') = r_o - \hat{n} \cdot \vec{r}_p(t')$$

$$= r_o - \rho \cdot \cos\vartheta \cdot \sin \frac{c\beta t'}{\rho} \qquad \text{(in retardation)}$$

$$= r_o \qquad \text{(in denominator)} .$$

The *retarded time* at which the radiation is observed is

$$t = t' + r_o/c - \rho/c \cos\theta \sin \frac{c\beta t'}{\rho}$$

$$= r_o/c + \frac{1}{2\gamma^2} \left\{ t'(1 + \gamma^2\theta^2) + \frac{1}{3} t'^3 \left(\frac{\gamma c}{\rho}\right)^2 \right\} , \qquad \text{(A.3.2)}$$

to lowest orders in the small parameters $1/\gamma$, ϑ and $(\beta ct'/\rho)$, and the *slope* becomes

$$\kappa = 1 - \beta\cos\theta \cos \frac{c\beta t'}{\rho}$$

$$= \frac{1}{2\gamma^2} \left(1 + \gamma^2\theta^2 + \gamma^2 \left(\frac{ct'}{\rho}\right)^2\right)$$

So far we have followed the approach of Jackson (Ref. A.1), who now proceeds directly to the spectral analysis. Here, we shall

push the investigation as far as possible while operating in the "time domain". The vector $\hat{\alpha}$ appearing in Eqs. (A.2.2-4) is given in terms of its components along a set of orthonormal vectors more convenient than $(\hat{x},\hat{y},\hat{z})$. These are

$$\hat{n},\ \hat{\epsilon}_{||} \equiv \hat{y}\ ,\ \hat{\epsilon}_{\perp} = \hat{n} \times \hat{\epsilon}_{||} = -\hat{x}\sin\vartheta + \hat{z}\cos\vartheta\ .$$

$\hat{\epsilon}_{||}$ is almost parallel to the acceleration and $\hat{\epsilon}_{\perp}$ almost orthogonal to it. The field of course has transverse polarization, $\hat{n}\cdot\hat{\alpha} = 0$, and the remaining two components are calculated to be

$$\hat{\epsilon}_{||} \cdot \hat{\alpha} = \frac{c}{\rho}\left\{\beta\cos\vartheta - \cos\frac{c\beta t'}{\rho}\right\} = -\frac{c}{\rho}\frac{1}{2\gamma^2}\left\{1 + \gamma^2\vartheta^2 - \gamma^2\left(\frac{c\beta t'}{\rho}\right)^2\right\}\ ,$$

$$\hat{\epsilon}_{\perp} \cdot \hat{\alpha} = \frac{c}{\rho} \cdot \sin\vartheta \cdot \sin\frac{c\beta t'}{\rho} = -\frac{c}{\rho}\frac{1}{2\gamma^2} \cdot 2\gamma\vartheta \cdot \gamma\frac{c\beta t'}{\rho}\ .$$

A.3.2. The electric field. Long or short magnet

According to (A.2.2), the two components of the electric field are

$$\hat{\epsilon}_{||}\cdot\vec{E}(\vec{r}_o,t) = \frac{e}{4\pi\epsilon_o r_o \rho}\ \frac{\cos\frac{c\beta t'}{\rho} - \beta\cos\vartheta}{\left(1-\beta\cos\vartheta\cos\frac{c\beta t'}{\rho}\right)^3}$$

$$= E_o \cdot 4\ \frac{1+(\gamma\vartheta)^2-\left(\frac{\gamma c t'}{\rho}\right)^2}{\left(1+(\gamma\vartheta)^2+\left(\frac{\gamma c t'}{\rho}\right)^2\right)^3} \qquad (A.3.3)$$

$$\hat{\varepsilon}_{\perp} \cdot \vec{E}(\vec{r}_o, t) = \frac{e}{4\pi\varepsilon_o r_o \rho} \frac{\sin\theta \sin \frac{c\beta t'}{\rho}}{(1-\beta \cos\theta \cos \frac{c\beta t'}{\rho})^3}$$

$$= E_o \cdot 8 \frac{\gamma\theta \cdot \frac{\gamma c t'}{\rho}}{(1+(\gamma\theta)^2+(\frac{\gamma c t'}{\rho})^2)^3}$$

introducing

$$E_o \equiv \frac{e}{4\pi\varepsilon_o r_o \rho} \cdot \gamma^4 \qquad (A.3.4)$$

as the natural scale of the field.

Equations (A.3.2-4) give the temporal evolution of the classical field at the point of observation. Let us examine the time scales. If the electron machine were perfectly circular, the repetition rate of the electron would be

$$\frac{\omega_o}{2\pi} = f_o = \frac{c}{2\pi\rho} ,$$

and according to (A.3.1), the radiation received at $\vec{r}_o$ is emitted within a time interval of

$$\Delta t' \sim (1/\gamma) \cdot (1/f_o) .$$

Then, according to (A.3.2) and to the general arguments of the preceding chapter, the light is received (at a time $\simeq r_o/c$ later, of course) within a time interval of

$$\Delta t \sim (1/\gamma^2) \cdot \Delta t' \equiv (1/\gamma^3) \cdot (1/f_o) ,$$

and typical frequencies of the signal will be of the order of

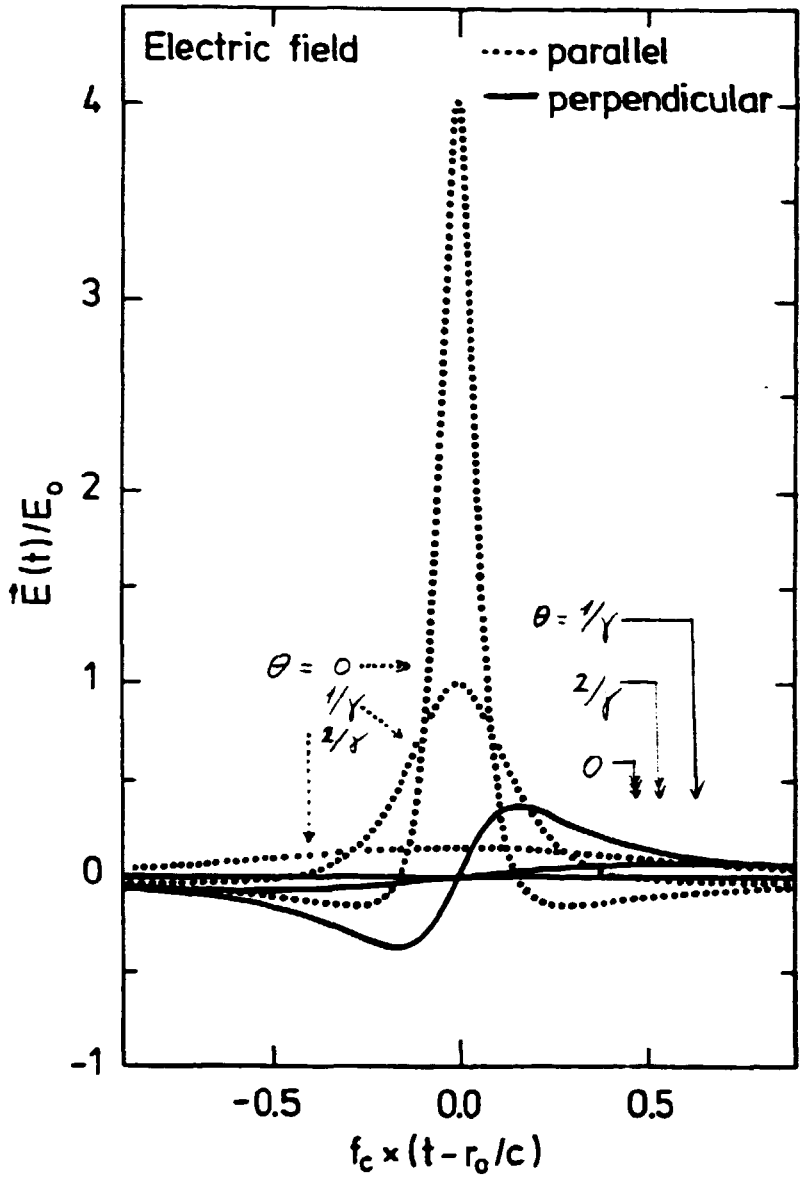

Figure A.3.2. The electric field, versus time, from a long bending magnet, as measured at a large distance r_o at various angles θ from the plane of the orbit. The field is given in terms of

$$E_o = \frac{e\gamma^4}{4\pi\varepsilon_o \cdot \rho \cdot r_o}$$

and the time is given in terms of $1/f_c$, where the critical frequency is

$$f_c = \frac{\omega_c}{2\pi} = \frac{1}{2\pi} \cdot \frac{3}{2} \frac{c}{\rho} \gamma^3 .$$

$$\omega_c \equiv 2\pi f_c \equiv 2\pi \cdot \frac{3}{2} \gamma^3 r_o = \frac{3}{2} \gamma^3 \frac{c}{\rho} , \qquad (A.3.5)$$

the factor (3/2) being introduced for later convenience. A plot of the field versus time is shown in Fig. (A.3.2).

The above calculations pertain to a *long magnet*, i.e. one that bends the path of the electron by more than $(1/\gamma)$ (Ref. A.4). If the magnet is *short*, only a window of the functions in Fig. (A.3.2) will be observed. This is sketched in Fig. (A.3.3).

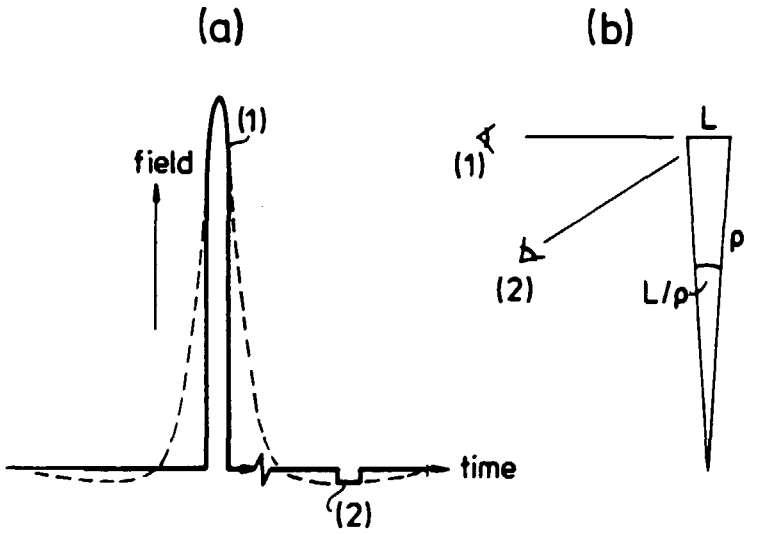

Fig. A.3.3. a: The electric field from a short bending magnet, as seen by an observer viewing the magnet tangentially (1) and off-tangentially (2).
b: The geometry of the problem.

In terms of the length L of the magnet, the condition for a long (short) magnet is

$$L/\rho \gg 1/\gamma \quad (L/\rho \ll 1/\gamma) .$$

For a short magnet, the time of emittance is only

$$\Delta t' = L/c = (\rho/c) \cdot (L/\rho) \ll (\rho/c) \cdot (1/\gamma) ,$$

and the width of the observed spectrum will then be

$$f_{\substack{typ. \\ short \\ magnet}} \sim \gamma^2 f_o \cdot \rho/L >> \frac{3}{2}\gamma^3 f_o = f_c(\text{long magnet})$$

For the rest of this paragraph, we shall consider only long magnets.

A.3.3. Analysis of the field from a long bending magnet

We now proceed to calculate the distribution w. r. to angles and polarization states of the intensity of the field. Two cases are considered, namely

(i) the ring contains only one electron,
(ii) a current I circulates in the ring.

In case (i), the signal (A.3.3) will be repeated at the rate $f_o = c/2\pi\rho$ (if the ring has no straight sections). Thus, a line spectrum of f_o and its harmonics will result. However, for an X-ray machine, $hf_c \approx 10$ keV, and $\gamma \sim 10^4$ ($E_e = \gamma mc^2 = 5$ GeV), so the spacing of the harmonics will be $hf_o \approx 10^{-8}$ eV. This will hardly be resolved by any X-ray experiment. Anyway, to be specific, in the following the *energy* from one electron passing the bending magnet *once* will be calculated. In case (ii), the different electrons will be considered to radiate independently of one another, so that the *power* will be proportional to the current. In case (ii), the imperfect beam optics will certainly cause the line spectrum to be completely smeared. If the energy (angular energy density, etc.) from one electron is ε, then the power P from a current I will be

$$P = (I/e)\varepsilon \ . \qquad \text{(A.3.6)}$$

Also we remark at this point that the two modes of polarization, being orthogonal, will contribute independently to the energy and related quantities:

$$\varepsilon = \varepsilon_{||} + \varepsilon_{\perp} \ .$$

Now for the calculations. A reduced time variable (τ) will be needed:

$$\tau \equiv \frac{\gamma c t'}{\rho\sqrt{1 + \gamma^2\theta^2}} \ , \quad \frac{dt'}{d\tau} = \frac{\rho}{\gamma c}\sqrt{1 + (\gamma\theta)^2} \ ,$$

$$t = r_o/c + \frac{3}{4}\frac{1}{\omega_c}(1 + \gamma^2\theta^2)^{3/2}(\tau + 1/3\ \tau^3) \ ,$$

$$\frac{dt}{d\tau} = \kappa\frac{dt'}{d\tau} + \frac{3}{4}\frac{N}{\omega_c}(1 + \gamma^2\theta^2)^{3/2} \ ,$$

$$N \equiv 1 + \tau^2 .$$

Then

$$\hat{\varepsilon}_{||}\cdot\vec{E} = E_o\frac{1}{(1+\gamma^2\theta^2)^2}\cdot 4\frac{1-\tau^2}{N^3} = E_o\cdot\frac{1}{(1+\gamma^2\theta^2)^2}\cdot 4\frac{N-2\tau^2}{N^3}$$

$$\hat{\varepsilon}_{\perp}\cdot\vec{E} = E_o\frac{\gamma\theta}{(1+\gamma^2\theta^2)^{5/2}}\cdot 8\frac{\tau}{N^3} \ .$$

According to (A.2.4), the two contributions to the Poynting vector are

$$\vec{S}_{||} = \hat{n}\cdot\frac{ce^2\gamma^8}{4\pi\cdot 4\pi\varepsilon_o\rho^2 r_o^2}\cdot\frac{16}{(1+\gamma^2\theta^2)^4}\cdot\left(\frac{1-\tau^2}{N^3}\right)^2 \ ,$$

$$\vec{S}_{\perp} = \hat{n}\cdot\frac{ce^2\gamma^8}{4\pi\cdot 4\pi\varepsilon_o\rho^2 r_o^2}\cdot\frac{64\gamma^2\theta^2}{(1+\gamma^2\theta^2)^5}\cdot\frac{\tau^2}{N^6} \ ,$$

and the energy per solid angle is

$$\frac{d\varepsilon}{d\Omega} = r_o^2 \int_{t=-\infty}^{\infty} S\, dt = \frac{3}{4}\frac{r_o^2}{\omega_c}(1+\gamma^2\theta^2)^{3/2}\int_{-\infty}^{\infty} N\cdot S\cdot d\tau ,$$

$$\left(\frac{d\varepsilon}{d\Omega}\right)_{||} = \frac{ce^2\gamma 8}{16\pi^2\varepsilon_o\rho^2\omega_c}\cdot\frac{3}{4}\frac{1}{(1+\gamma^2\theta^2)^{5/2}}\cdot 16\int\frac{(1-\tau^2)^2}{N^5}\,d\tau$$

$$= \frac{ce^2\gamma 8}{16\pi^2\varepsilon_o\rho^2\omega_c}\,\frac{21\pi}{8(1+\gamma^2\theta^2)^{5/2}} ,$$

(A.3.7)

$$\left(\frac{d\varepsilon}{d\Omega}\right)_{\perp} = \frac{ce^2\gamma 8}{16\pi^2\varepsilon_o\rho^2\omega_c}\,\frac{3}{4}\,\frac{\gamma 2\theta 2}{(1+\gamma^2\theta^2)^{7/2}}\cdot 64\int\frac{\tau 2}{N^5}\,d\tau$$

$$= \frac{ce^2\gamma 8}{16\pi^2\varepsilon_o\rho^2\omega_c}\,\frac{15\pi\gamma 2\theta 2}{8(1+\gamma^2\theta^2)^{7/2}} .$$

The energy per radian of curvature along the electron beam then is

$$\frac{1}{2\pi}\varepsilon_e = \frac{d\varepsilon}{d\phi} = \int_{-\pi/2}^{\pi/2}\frac{d\varepsilon}{d\Omega}\cos\theta d\theta \approx \frac{1}{\gamma}\int_{-\infty}^{\infty}\frac{d\varepsilon}{d\Omega}\,d(\gamma\theta) ,$$

ε_e being the total energy emitted by an electron making one revolution in a machine of constant radius ρ. Integrating (3.7), we get

$$\frac{d\varepsilon}{d\phi} = \frac{ce^2\gamma 7}{16\pi^2\varepsilon_o\rho^2\omega_c}\cdot 4\pi ,$$

$$\left(\frac{d\varepsilon}{d\phi}\right)_{||} = \frac{7}{8}\frac{d\varepsilon}{d\phi} ,$$

$$\left(\frac{d\varepsilon}{d\phi}\right)_{\perp} = \frac{1}{8}\frac{d\varepsilon}{d\phi} \quad .$$

Thus the energy per electron per turn is

$$\varepsilon_e = \frac{4\pi}{3}\frac{e^2\gamma^4}{4\pi\varepsilon_o\rho} = \frac{4\pi}{3}\frac{r_e}{\rho}mc^2\gamma^4$$

$$= \frac{4\pi}{3}\frac{Be^3c\gamma^3}{4\pi\varepsilon_o mc^2} = \frac{4\pi}{3}r_e \cdot B \cdot e \cdot c\gamma^3 \quad , \tag{A.3.8}$$

and the power for current I is

$$P_I = \frac{4\pi}{3}\frac{Ie\gamma^4}{4\pi\varepsilon_o\rho} = \frac{4\pi}{3}\frac{I}{e}\frac{r_e}{\rho}mc^2\gamma^4$$

$$= \frac{4\pi}{3}I\frac{Be^2c\gamma^3}{4\pi\varepsilon_o mc^2} = \frac{4\pi}{3}I \cdot r_e B \cdot c\gamma^3 \quad . \tag{A.3.9}$$

Considering a magnet of length $L \leq 2\pi\rho$ this is reduced to

$$P_I(L) = \frac{L}{2\pi\rho}P_I = L \cdot \frac{2}{3}\frac{Ir_e mc^2}{e\rho^2}\gamma^4 = L \cdot \frac{2}{3}\frac{Ir_e c^2B^2e\gamma^2}{mc^2} \tag{A.3.9'}$$

From general considerations, using (A.2.13) with

$$\dot{\beta}_{||} = 0, \quad \dot{\beta}_{\perp} = \frac{\beta c}{\rho} \approx \frac{c}{\rho}\left(1 - \frac{1}{2\gamma^2}\right) \approx \frac{c}{\rho} \quad ,$$

one gets the energy

$$\varepsilon_e = \frac{1}{f_o}P_e = \frac{2\pi\rho}{c} \cdot \frac{2}{3}\frac{e^2\gamma^4}{4\pi\varepsilon_o c}\left(\frac{c}{\rho}\right)^2$$

in accordance with (A.3.8). Thus, the power is given correctly by the approximations except for errors of the order of $(1/\gamma^2)$. Putting numbers into (A.3.8-9) yields

$$\varepsilon_e = 88.5 \text{ keV} \cdot \frac{(E_e/\text{GeV})^4}{\rho/\text{meters}}$$

$$= 26.8 \text{ keV} \cdot (E_e/\text{GeV})^3 \cdot (B/\text{Tesla}) ,$$

(E_e being the energy of the electron), and this voltage needs to be supplied by the r.f. cavities. The power then becomes

$$P_I = 88.5 \text{ kW} \cdot \frac{I}{\text{Amps}} \cdot \frac{(E_e/\text{GeV})^4}{\rho/\text{meters}}$$

$$= 26.8 \text{ kW} \cdot \frac{I}{A} \cdot \frac{B}{T} \cdot \left(\frac{E_e}{\text{GeV}}\right)^3 ,$$

$$P_I(L) = 1.27 \text{ kW} \cdot \frac{I}{A} \cdot (B/T)^2 \cdot (E_e/\text{GeV})^2 \cdot (L/\text{meters})$$

$$= 14.1 \text{ kW} \cdot \frac{I}{A} \cdot \left(\frac{E_e}{\text{GeV}}\right)^4 \cdot \frac{L/m}{(\rho/m)^2}$$

Going backwards we can express the various differential powers in terms of P_I, noting that the energies will be related to ε_e in exactly the same manner:

$$P_{||} = \frac{7}{8} P_I \quad , \quad P_{\perp} = \frac{1}{8} P_I \ ,$$

$$\left(\frac{dP}{d\phi}\right)_{\substack{(||\\(\perp\\(\text{total}}} = \frac{1}{2\pi} \cdot \begin{matrix}(P_{||}\\(P_{\perp}\\(P_I\end{matrix} ,$$

$$\left(\frac{dP}{d\Omega}\right)_{||} = \gamma \cdot \frac{P_I}{2\pi} \cdot \frac{21}{32} \cdot \frac{1}{(1+\gamma^2\theta^2)^{5/2}} \qquad \text{(A.3.9')}$$

$$\left(\frac{dP}{d\Omega}\right)_{\perp} = \gamma \cdot \frac{P_I}{2\pi} \cdot \frac{15}{32} \cdot \frac{\gamma^2\theta^2}{(1+\gamma^2\theta^2)^{7/2}} \ .$$

The rest of the analysis concerns the frequency domain. We must then consider

$$\vec{E}(\omega) = \frac{1}{\sqrt{2\pi}} \int_{-\infty}^{\infty} e^{i\omega t} \vec{E}(t) dt \ . \qquad \text{(A.3.10)}$$

With this normalization, Parsevals theorem reads

$$\int_{-\infty}^{\infty} |\vec{E}(t)|^2 \, dt = \int_{-\infty}^{\infty} |\vec{E}(\omega)|^2 \, d\omega = 2 \int_{0}^{\infty} |\vec{E}(\omega)|^2 \, d\omega,$$

restricting to positive frequencies. Thus, using (A.2.4), the energy per solid angle is

$$\frac{d\varepsilon}{d\Omega} = \frac{2r_o^2}{c\mu_o} \int_{o}^{\infty} |\vec{E}(\omega)|^2 \, d\omega. \qquad \text{(A.3.9'')}$$

From (A.3.11) we identify the *spectral brightness* (energy per solid angle per absolute bandwidth or photons per solid angle per relative bandwidth):

$$\frac{d\varepsilon}{d\Omega\, d\hbar\omega} = \frac{d\varepsilon/\hbar\omega}{d\Omega\, d\hbar\omega/\hbar\omega} = \frac{2r_o^2}{\hbar c \mu_o} |\vec{E}(\omega)|^2 . \qquad (A.3.12)$$

The Fourier transformation (A.3.10) is difficult, e.g.

$$\vec{E}(\omega) \propto \int_{t=-\infty}^{\infty} \frac{\vec{\mathfrak{A}}(t'(t))}{\kappa(t'(t))^3} e^{i\omega t}\, dt$$

or

$$\vec{E}(\omega) \propto \int_{t'=-\infty}^{\infty} \frac{\vec{\mathfrak{A}}(t')}{\kappa(t')^2} e^{i\omega t(t')}\, dt'$$

A partial integration (Ref. A.1, § 14.5), however, yields

$$\vec{E}(\omega) = \frac{-e(-i\omega)}{4\pi\sqrt{\varepsilon_o/\mu_o}\, r_o} \cdot \frac{1}{\sqrt{2\pi}} \cdot \int_{t'=-\infty}^{\infty} (\hat{n}\times(\hat{n}\times\vec{\beta}(t'))) e^{i\omega\cdot t(t')}\, dt' \qquad (A.3.13)$$

in which the remaining complexity arises mainly from the retarded time in the exponential. Using

$$\hat{\varepsilon}_{||} \cdot (\hat{n}\times(\hat{n}\times\vec{\beta}(t'))) = -\hat{\varepsilon}_{||} \cdot \vec{\beta} = -\beta \sin\frac{ct'}{\rho} \approx -\frac{ct'}{\rho},$$

$$\hat{\varepsilon}_{\perp} \cdot (\hat{n}\times(\hat{n}\times\vec{\beta})) = -\hat{\varepsilon}_{\perp} \cdot \vec{\beta} = -\sin\theta \cdot \beta \cos\frac{ct'}{\rho} \approx -\theta ,$$

and the approximation (A.3.2) for t', this becomes

$$\hat{\varepsilon}_{||} \cdot \vec{E}(\omega) = - \frac{e \cdot i\omega}{4\pi\sqrt{\varepsilon_o/\mu_o}\; r_o\sqrt{2\pi}} e^{\frac{i\omega r_o}{c}} \cdot$$

$$\cdot \int_{-\infty}^{\infty} \frac{ct'}{\rho} \exp\left[\frac{i\omega t'}{2\gamma^2}\{1+\gamma^2\theta^2 + \frac{1}{3}(\frac{\gamma c}{\rho} t')^2\}\right] dt' ,$$

$$\hat{\varepsilon}_{\perp} \cdot \vec{E}(\omega) = -(\text{same fraction}) \cdot e^{\frac{i\omega r_o}{c}} \int_{-\infty}^{\infty} \theta \cdot \exp[\text{same exponent}]\, dt'.$$

Introducing

$$\tau = \frac{\gamma c t'}{\rho\sqrt{1+\gamma^2\theta^2}} \quad , \quad \xi = \frac{\omega}{2\omega_c} (1+\gamma^2\theta^2)^{3/2} ,$$

names are given to the integrals (Ref. A.1, § 14.6):

$$\int \frac{ct'}{\rho} \exp[\;\;] \, dt' = \frac{\rho}{c} \frac{1+\gamma^2\theta^2}{\gamma^2} \int \tau \exp(i \frac{3}{2} \xi\tau \{1 + \frac{\tau^2}{3}\}) d\tau$$

$$= \frac{\rho}{c} \frac{1+\gamma^2\theta^2}{\gamma^2} \cdot \frac{2}{\sqrt{3}} \cdot i \cdot K_{2/3}(\xi) , \qquad (A.3.14)$$

$$\int \theta \cdot \exp[\;\;] dt' = \frac{\rho}{c} \frac{\gamma\theta\sqrt{1+\gamma^2\theta^2}}{\gamma^2} \int \exp(i \frac{3}{2} \xi\tau \{1 + \frac{\tau^2}{3}\}) d\tau$$

(A.3.15)

$$= \frac{\rho}{c} \cdot \frac{\gamma\theta \cdot \sqrt{1+\gamma^2\theta^2}}{\gamma^2} \cdot \frac{2}{\sqrt{3}} K_{1/3}(\xi) ,$$

the K's being modified Bessel functions (Ref. A.1, § 3.7), defined by

$$K_\nu(\xi) = \frac{\pi}{2} i^{\nu+1}(H_\nu^{(1)}(i\xi)) = \frac{\pi}{2} i^{\nu+1} \{J_\nu(i\xi) + iN_\nu(i\xi)\}$$

$$= \frac{\pi}{2\sin\pi\nu} (I_{-\nu}(\xi) - I_\nu(\xi)) \ , \ I_\nu(\xi) = i^{-\nu} J_\nu(i\xi) \ ,$$

in terms of Hankel ($H^{(1)}$), Bessel (J) and Neumann (N) functions. Thus the fields are

$$\hat{\varepsilon}_{||} \cdot \vec{E}(\omega) = \frac{e \cdot \omega}{4\pi\sqrt{2\pi}\ \sqrt{\varepsilon_o/\mu_o}\ r_o} \frac{\rho}{c} \frac{1+\gamma^2\theta^2}{\gamma^2} \frac{2}{\sqrt{3}} K_{2/3}(\xi) \ ,$$

(A.3.16)

$$\hat{\varepsilon}_{\perp} \cdot \vec{E}(\omega) = \frac{1}{i} \frac{e \cdot \omega}{4\pi\sqrt{2\pi}\ \sqrt{\varepsilon_o/\mu_o}\ r_o} \frac{\rho}{c} \frac{\gamma\theta\sqrt{1+\gamma^2\theta^2}}{\gamma^2} \frac{2}{\sqrt{3}} K_{1/3}(\xi) \ ,$$

and insertion into (A.3.12) yields the spectral brightness for current I, being the power per solid angle per absolute photon energy bandwidth or photon rate per solid angle per relative bandwidth:

$$\frac{dP}{d\Omega\ d\hbar\omega} = \frac{dP/\hbar\omega}{d\Omega\ d\hbar\omega/\hbar\omega} = \frac{P_I \cdot \gamma}{\hbar\omega_c} \cdot \left(\frac{3}{2\pi}\right)^3 \cdot F_S(\xi, \gamma\theta) \ . \qquad \text{(A.3.17)}$$

Here following Ref. A.4, the universal brightness function in (A.3.17) is

$$F_S(\xi, \gamma\theta) = \frac{\xi^2}{1+\gamma^2\theta^2} \{K^2_{2/3}(\xi) + \frac{\gamma^2\theta^2}{1+\gamma^2\theta^2} K^2_{1/3}(\xi)\} \ ,$$
$$(||) \qquad\qquad (\perp)$$

(A.3.18)

where the contribution from each polarization state is indicated. Integration over angles gives the result (Ref. A.1)

$$\frac{dP}{d\hbar\omega} = \frac{dP/\hbar\omega}{d\hbar\omega/\hbar\omega} = \frac{P_I}{\hbar\omega_c} \cdot S(\omega/\omega_c) \ , \qquad \text{(A.3.19)}$$

where the universal spectral function is (Ref. A.4)

$$S(\omega/\omega_c) = \frac{9\sqrt{3}}{8\pi} \int_{\omega/\omega_c}^{\infty} K_{5/3}(\eta)d\eta \ . \qquad (A.3.20)$$

The functions $F_S(\xi,0)$ and $S(\omega/\omega_c)$ are plotted in Fig. A.3.4 and tabulated in Table A.3.5.

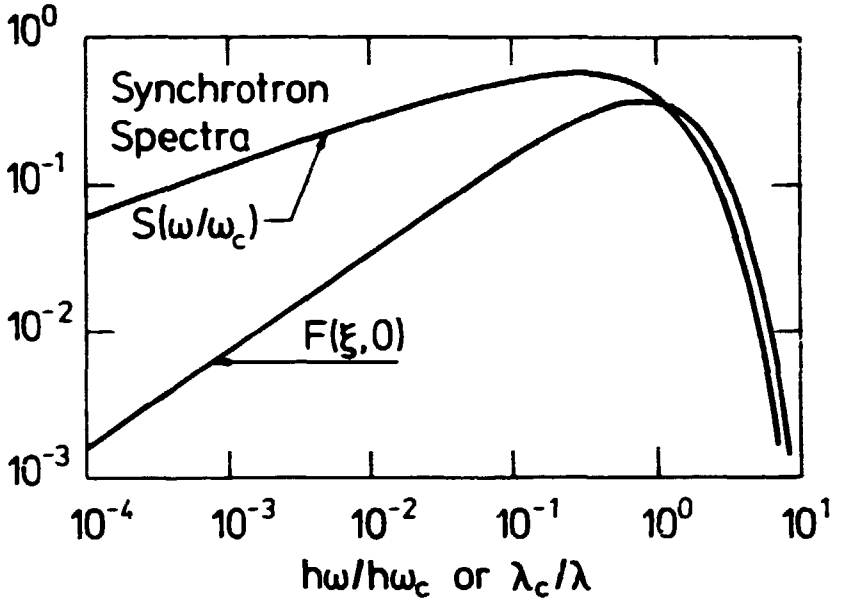

Fig. A.3.4. The universal functions describing synchrotron radiation,

$$F_S(\xi,0) = \xi^2 K_{2/3}^2(\xi) = \left(\frac{\omega}{2\omega_c}\right)^2 K_{2/3}^2\left(\frac{\omega}{2\omega_c}\right) ,$$

$$S(\omega/\omega_c) = \frac{9\sqrt{3}}{8\pi} \int_{\omega/\omega_c}^{\infty} K_{5/3}(\eta)d\eta$$

plotted versus the normalized frequency ω/ω_c. The plots were prepared on the basis of a table of Bessel functions in Ref. A.7.

Table A.3.5. The universal functions

$$S(\omega/\omega_c) = \frac{9\sqrt{3}}{8\pi} \int_y^\infty K_{5/3}(\eta)d\eta \ ,$$

$$F_s(\xi,0) = \xi^2 K_{2/3}^2(\xi) = \frac{1}{4} y^2 K_{2/3}^2(y/2) \ ,$$

$$y \equiv \omega/\omega_c \ .$$

The table was prepared on the basis of a table of Bessel functions in Ref. A.8.

$y=\omega/\omega_c$	$S(\omega/\omega_c) = \frac{9\sqrt{3}}{8\pi}\int_y^\infty K_{5/3}(\eta)d\eta$	$F_s(\xi,0) = \frac{y^2}{4}K_{2/3}^2(y/2)$	y	$S(\omega/\omega_c)$	$F_s(\xi,0)$
0.0001	1.035E-01	1.533E-01	1.0000	4.048E-01	1.415E-01
0.0010	1.313E-01	1.377E-01	1.2500	3.130E-01	1.421E-01
0.0020	1.457E-01	1.355E-01	1.5000	2.445E-01	1.416E-01
0.0040	1.671E-01	1.331E-01	1.7500	1.934E-01	1.398E-01
0.0060	1.815E-01	1.309E-01	2.0000	1.537E-01	1.367E-01
0.0080	1.930E-01	1.287E-01	2.2500	1.225E-01	1.326E-01
0.0100	2.028E-01	1.265E-01	2.5000	9.814E-02	1.279E-01
0.0200	2.394E-01	1.175E-01	2.7500	7.912E-02	1.228E-01
0.0300	2.605E-01	1.096E-01	3.0000	6.417E-02	1.176E-01
0.0400	2.111E-01	1.028E-01	3.2500	5.230E-02	1.124E-01
0.0500	2.351E-01	9.719E-02	3.5000	4.277E-02	1.073E-01
0.0600	2.543E-01	1.023E-01	3.7500	3.503E-02	1.024E-01
0.0700	2.711E-01	1.205E-01	4.0000	2.877E-02	9.772E-02
0.0800	2.861E-01	1.311E-01	4.2500	2.374E-02	9.330E-02
0.0900	2.971E-01	1.411E-01	4.5000	1.962E-02	8.911E-02
0.1000	3.075E-01	1.506E-01	4.7500	1.628E-02	8.454E-02
0.1500	3.426E-01	1.921E-01	5.0000	1.353E-02	8.117E-02
0.2000	3.603E-01	2.259E-01	5.5000	1.130E-02	7.777E-02
0.2500	3.710E-01	2.541E-01	6.0000	9.425E-03	7.474E-02
0.3000	3.693E-01	2.777E-01	6.5000	7.879E-03	7.206E-02
0.3500	3.859E-01	2.975E-01	7.0000	6.595E-03	6.966E-02
0.4000	3.910E-01	3.140E-01	7.5000	5.538E-03	6.751E-02
0.4500	3.947E-01	3.277E-01	8.0000	4.677E-03	6.560E-02
0.5000	3.972E-01	3.390E-01	8.5000	3.976E-03	6.391E-02
0.5500	3.984E-01	3.480E-01	9.0000	3.394E-03	6.241E-02
0.6000	3.988E-01	3.552E-01	9.5000	1.922E-03	5.774E-02
0.6500	3.983E-01	3.606E-01	10.0000	1.191E-03	3.645E-02
0.7000	4.000E-01	3.644E-01			
0.7500	4.745E-01	3.670E-01			
0.8000	4.605E-01	3.683E-01			
0.8500	4.463E-01	3.685E-01			
0.9000	4.321E-01	3.677E-01			

Putting numbers into the formulae of this chapter, we get the critical parameters:

$$\hbar\omega_c = \frac{3}{2}\frac{\hbar c}{\rho}\gamma^3 = 2.219\ \text{keV} \cdot \frac{(E_e/\text{GeV})^3}{\rho/\text{meters}}$$

$$= \frac{3}{4\pi}\frac{hc^2Be}{mc^2}\gamma^2 = 0.663\ \text{keV} \cdot (B/\text{Tesla}) \cdot (E_e/\text{GeV})^2 \ , \qquad \text{(A.3.5')}$$

$$\lambda_c = \frac{4\pi}{3}\rho/\gamma^3 = 5.589\ \text{Å} \cdot \frac{\rho/\text{meters}}{(E_e/\text{GeV})^3}$$

$$= \frac{4\pi}{3}\frac{mc^2}{cBe}\gamma^{-2} = 18.64\ \text{Å} \cdot (E_e/\text{GeV})^{-2} \cdot (B/\text{Tesla})^{-1} \ .$$

The (frequency integrated) brightness (A.3.9"), the spectral brightness (A.3.17) and the spectrum (A.3.19) give:

$$\frac{dP}{d\Omega}_{|\vartheta=0} = \frac{P_I \cdot \gamma}{2\pi} \cdot \frac{21}{32} = 18.1\ \frac{\text{MW}}{\text{sterad}} \cdot \left(\frac{E_e}{\text{GeV}}\right)^5 \cdot \left(\frac{I}{\text{A}}\right)^1 \cdot \left(\frac{\rho}{\text{m}}\right)^{-1} \qquad \text{(A.3.9''')}$$

$$= 5.48\ \frac{\text{MW}}{\text{sterad}} \cdot \left(\frac{E_e}{\text{GeV}}\right)^4 \cdot \left(\frac{I}{\text{A}}\right)^1 \cdot \left(\frac{B}{\text{T}}\right)^1$$

$$\frac{dP}{d\Omega\ d\hbar\omega} = 8.50\ \frac{\text{kW}}{\text{eV}\cdot\text{sterad}} \cdot F_s(\xi, \gamma\vartheta) \cdot \left(\frac{E_e}{\text{GeV}}\right)^2 \cdot \frac{I}{\text{A}} \qquad \text{(A.3.17')}$$

$$= \frac{dP/\hbar\omega}{d\Omega\ d(\ln(\hbar\omega))} = 5.30 \cdot 10^{22}\ \frac{\text{Photons}}{\text{sterad}\cdot\text{sec}} \cdot F_s \cdot \left(\frac{E_e}{\text{GeV}}\right)^2 \cdot \frac{I}{\text{A}}$$

(per unit relative bandwidth).

$$\left.\frac{dP}{d\Omega\, d\hbar\omega}\right|_{\substack{\omega=\omega_c \\ \vartheta=0}} = 3.09\ \frac{kW}{eV\cdot sterad}\cdot (E/GeV)^2 \cdot (I/A)$$

$$= \left.\frac{dP/\hbar\omega}{d\Omega\, d(\ln(\hbar\omega))}\right|_{\substack{\omega=\omega_c \\ \vartheta=0}} = 1.93 \cdot 10^{22}\ \frac{Photons}{sterad\cdot sec}\cdot (E/GeV)^2 \cdot (I/A)$$

(per unit relative bandwidth).

$$\frac{dP}{d\hbar\omega} = 39.3\ \frac{W}{eV}\cdot S(\omega/\omega_c)\cdot \left(\frac{E}{GeV}\right)^1 \cdot \left(\frac{I}{Amp}\right)$$

(A.3.19')

$$= \frac{dP/\hbar\omega}{d(\ln(\hbar\omega))} = 2.49 \cdot 10^{20}\ \frac{Photons}{second}\cdot S(\omega/\omega_c)\cdot (E/GeV)^1 \cdot (I/A)$$

(per unit relative bandwidth).

$$\left.\frac{dP}{d\hbar\omega}\right|_{\omega=\omega_c} = 16.1\ \frac{W}{eV}\cdot (E/GeV)^1 \cdot (I/Amp)$$

$$= \left.\frac{dP/\hbar\omega}{d(\ln(\hbar\omega))}\right|_{\omega=\omega_c} = 1.01 \cdot 10^{20}\ \frac{Photons}{second}\cdot (E/GeV)^1 \cdot (I/Amp)$$

(per unit relative bandwidth).

Concerning the polarization, we note that according to (A.3.16), the two components of linear polarization are in quadrature, so that the radiation is elliptically polarized (and horizontally linearly polarized in the plane of the orbit), as shown in Fig. A.3.6. This result may be derived as well by a symmetry argument.

In conclusion, this paragraph in some detail has reviewed the theory of synchrotron radiation to provide a firm basis for comparison with the radiation sources described in the next paragraphs.

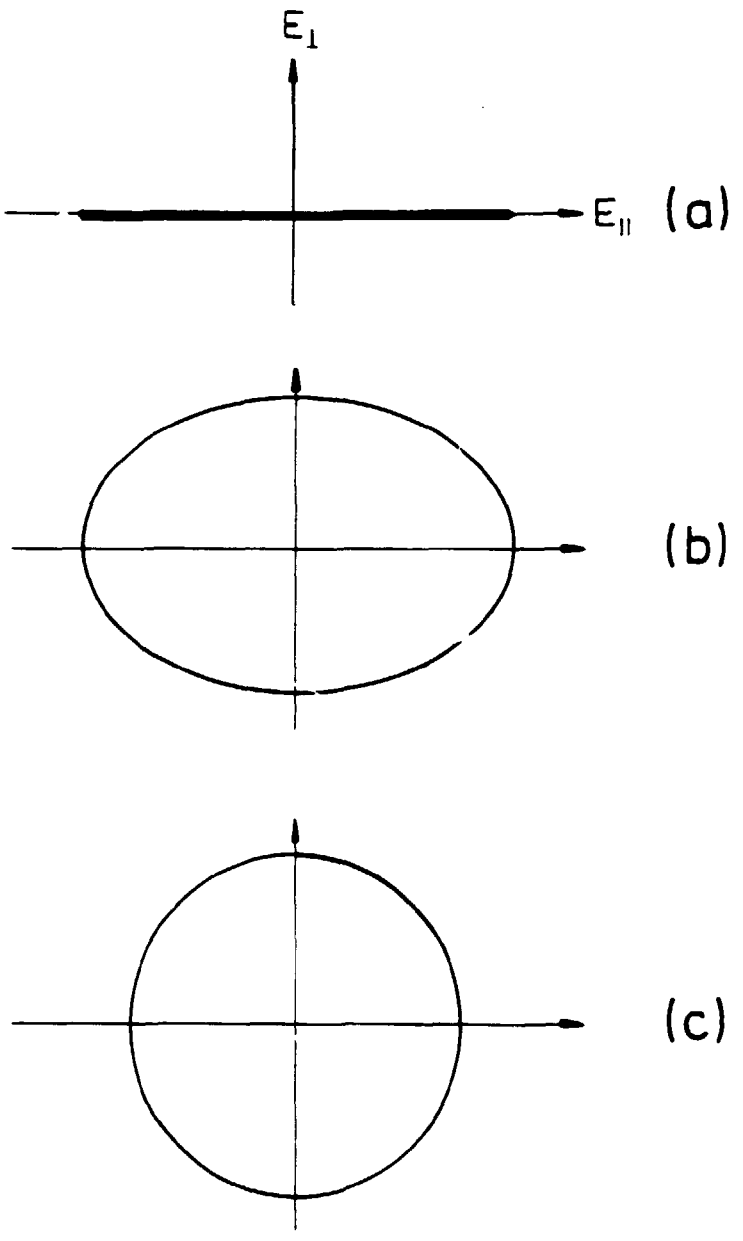

Fig. A.3.6. Ellipses of polarization for the synchrotron radiation at $\omega=\omega_c$ and at various angles from the plane.
a: $\theta=0$, $E_\perp/E_{||} = 0$, linear polarization.
b: $\gamma\theta=1$, $\xi(\omega_c,\theta) = \sqrt{2}$,

$$E_\perp/E_{||} = \frac{\sqrt{2}\, K_{1/3}\,(\sqrt{2})}{2\, K_{2/3}\,(\sqrt{2})} \approx 0.65, \text{ elliptical polarization.}$$

c: $\gamma\theta \gg 1$, $\xi \gg 1$,

$$E_\perp/E_{||} = \frac{K_{1/3}\,(\xi)}{K_{2/3}\,(\xi)} \to 1, \text{ circular polarization.}$$

A.4. The radiation from a wiggler or ondulator

The idea of bending the electron path more than the general curvature of the machine leads to the concept of a wiggler, as shown in Fig. A.4.1a.

The power, according to (A.2.13), will then be

$$P_{I,w} = \frac{I}{e} \cdot \frac{2}{3} \frac{e^2\gamma^4}{4\pi\varepsilon_o c} \int_o^{L/c} (\dot{\beta}_\perp)^2 \, dt' \, .$$

In terms of the radius of curvature, the acceleration is

$$\dot{\beta}_\perp = c^2/\rho$$

$$P_{I,w} = \frac{2}{3} \frac{Ie\gamma^4}{4\pi\varepsilon_o} \int_o^L \rho^{-2} \, ds = \frac{2}{3} \frac{mc^2 r_e \gamma^4 I}{e} \int_o^L \rho^{-2} \, ds \qquad (A.4.1)$$

integrating along the wiggler. For constant ρ this reduces to (A.3.9), and generally the radiation power of the wiggler is the same as for a constantly curved device of the same integrated squared curvature. Nevertheless, interference effects may cause the *spectrum* to be very much different from the synchrotron radiation spectrum (A.3.18). Seemingly, the term ondulator is used for a device in which interference effects are important, whereas a wiggler is defined as having a spectrum more like the incoherent superposition of the spectra from the constituent bending magnets. Of course, the number of elements is a crucial quantity in this connection. For a perfectly regular array of 2N magnets *and for ideal optical properties of the electron beam*, the power spectrum will be shifted into a fundamental frequency ω_1 and its harmonics, the width of the peaks being $\Delta\omega \sim (1/N)\cdot\omega_1$. Thus, for more than a few elements, the interference will be very important in this case. We consider in more detail such an ondulator:

The two cases (as in Section A.3.2) of long and short magnets must be distinguished. Figure A.4.1b1 shows an electron path consisting of alternating circular segments. In terms of the variables defined in the figure,

$$\psi_o \approx \frac{a}{\lambda_w/4} = \frac{\lambda_w/4}{\rho - a} \approx \frac{\lambda_w/4}{\rho} >> 1/\gamma \ , \qquad (A.4.2)$$

the inequality expressing the condition for a long magnet. Each half-period will produce a synchrotron radiation pulse of duration $\sim \rho/(c\gamma^3)$ (as in Fig. A.3.2), and an observer in the forward direction according to Eq. (A.2.6) will receive the pulses from adjacent magnets a time $(\lambda_w/2c)\cdot(1/2\gamma^2)$ apart. This is shown in Fig. A.4.1b2. The spectrum (A.3.17) will thus be split into harmonics of the frequency

$$\omega_1 = \frac{2\pi}{(\lambda_w/c)\cdot(1/2\gamma^2)} = \frac{2\pi c}{\lambda_w} \cdot 2\gamma^2 \qquad (A.4.3)$$

The number of harmonics of appreciable magnitude is

$$\#\text{harmonics} \cong \frac{\omega_c}{\omega_1} = \frac{3}{2\pi} \cdot \frac{\lambda_w/4}{\rho} \cdot \gamma >> 1 \qquad (A.4.4)$$

This is shown in Fig. A.4.1b3.

The case of an ondulator built from short magnets is characterized by

$$\psi_o = \frac{L/2}{\rho} << 1/\gamma$$

as in Fig. A.4.1c1. Reasoning as above, we see that each bent section contributes a truncated synchrotron pulse (as in Fig. A.3.3a), these arriving $(\lambda_w/2c)(1/2\gamma^2)$ apart. The spectrum thus consists of harmonics of (A.4.3), filling the white spectrum from a short magnet which extends to

$$\omega_{typ} = 2\gamma^2 \cdot \frac{c}{L/2} \ .$$

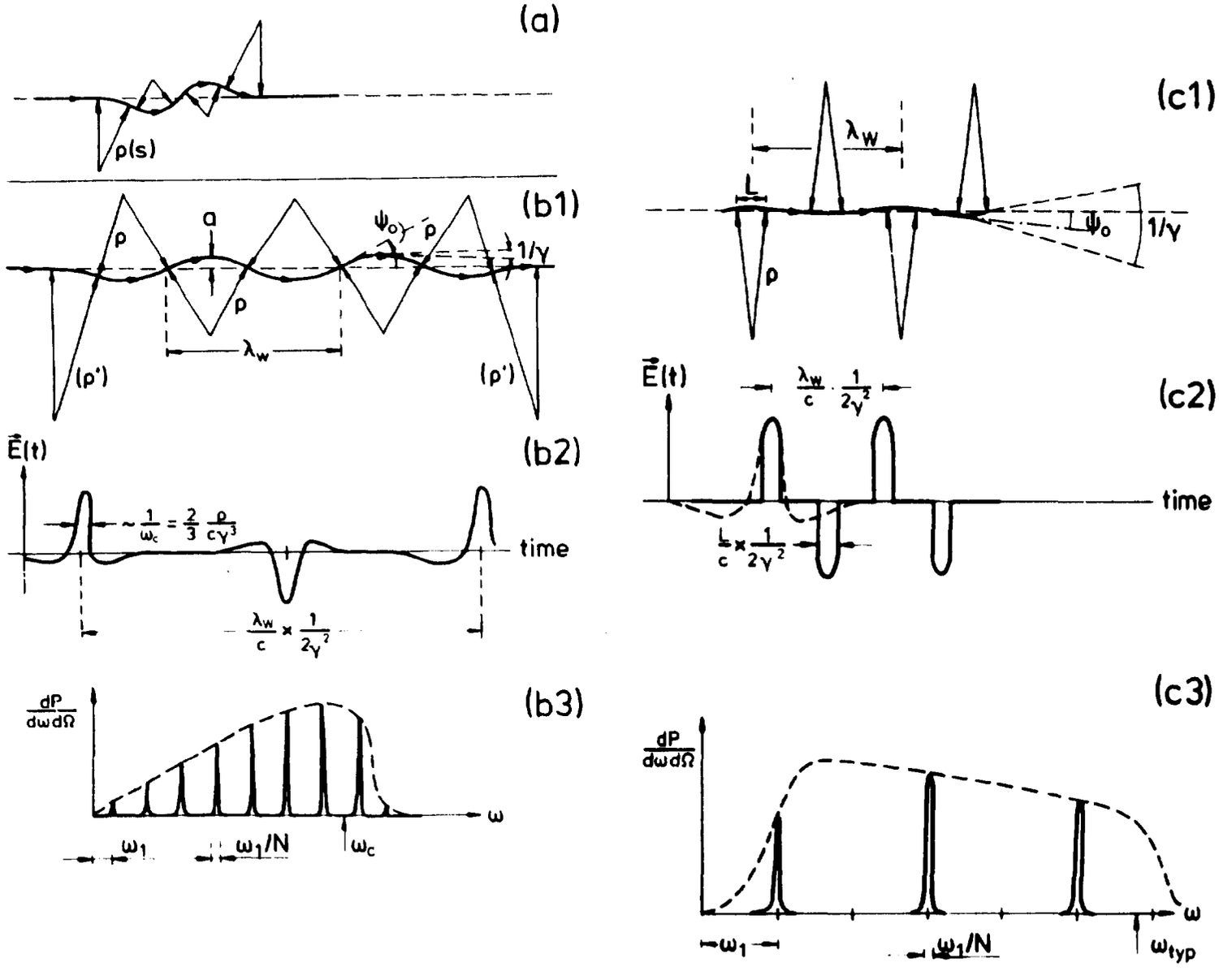
(a)
ρ(s)
(b1)
ρ
a
ψo
ρ
1/γ
ρ
λw
(ρ')
(ρ')
(b2)
Ē(t)
~1/ωc = 2/3 ρ/cγ³
time
λw/c × 1/2γ²
(b3)
dP/dωdΩ
ω
ω1
ω1/N
ωc
(c1)
λw
L
ψo
1/γ
ρ
Ē(t)
λw/c · 1/2γ²
(c2)
time
L/c × 1/2γ²
(c3)
dP/dωdΩ
ω
ω1
ω1/N
ωtyp

Fig. A.4.1.
a: A general wiggler: A juxtaposition of several (possibly different) bending magnets.
b: An undulator consisting of long, homogeneous magnets.
b1: The geometry. Transverse oscillations are shown exaggerated.
b2: The electric field versus time, as seen by an observer in the forward direction.
b3: The spectral brightness in the forward direction. As shown, for $\theta=0$ only odd harmonics are present. This is so because the field is odd-half-periodic,

$$E(t + \frac{1}{2}(\lambda_w/c)/(2\gamma^2)) = -E(t) .$$

c: An ondulator built from short magnets.
c1: The geometry. Transverse oscillations are shown exaggerated.
c2: $\vec{E}(t)$ vs. t.
c3: Spectral brightness.

Thus the number of harmonics is

$$\#\text{harmonics} \sim \frac{\omega_{typ}}{\omega_1} = \pi \frac{\lambda_w}{L} . \qquad (A.4.5)$$

This is shown in Fig. A.4.1c2-3. If $\lambda_w = 2L$, as will usually be the case, (A.4.5) shows that only the first few harmonics will be present.

The frequencies observed at an angle θ off-axis may also be derived, applying the conditions for constructive interference (Ref. A.5) as in Fig. A.4.2. For the radiation emitted from $z = 0$ at $t' = 0$ to be in phase with the radiation emitted from $z = \lambda_w$ at $t' = \lambda_w/\beta c$,

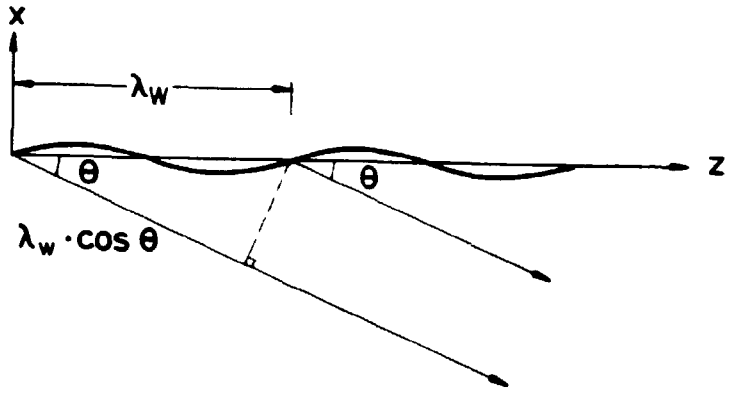

Fig. A.4.2. Geometry for the derivation (Motz (Ref. A.5, 1977)) of the ondulator frequency off-axis.

$$\frac{\lambda_w}{\beta c} - \frac{\lambda_w \cos\theta}{c} = n \cdot \frac{2\pi}{\omega} = n \cdot \frac{\lambda}{c} ;$$

$$\lambda \cong \frac{1}{n} \cdot \frac{\lambda_w}{2\gamma^2} (1+\gamma^2\theta^2)$$

in accordance with (A.2.7) and (A.2.8).

In terms of numbers, the first harmonic will be

$$\hbar\omega_1 = 9.5 \text{ eV} \cdot (E/\text{GeV})^2 \cdot (\lambda_w/\text{meters})^{-1} ,$$

$$\lambda_1 = 1300 \text{ Å} \cdot (E/\text{GeV})^{-2} \cdot (\lambda_w/\text{meters})^{1} .$$

Thus at 5 GeV, to get $\lambda_1 = 1.54$ Å, $\lambda_w = 3.0$ cm would be needed.

In the next paragraph the case of a sinusoidal ondulator is treated, being exactly soluble. The result is a detailed knowledge of the intensities, polarization etc., as well as some details concerning the frequencies which the above qualitative treatment has missed.

A.5. The radiation from a sinusoidal ondulator

If a line spectrum is desired, one may wish to get rid of the higher harmonics. Plausibly, this is achieved by wiggling the electrons along a sinusoidal path. Equally plausible, a magnetic field varying like a sine-function along the beam would seem to furnish such a trajectory. As will be seen from the following sections, the above statements are true for the case of a "weak" magnetic field.

The sinusoidal ondulator has been treated by Ref. A.6 (see also Ref. A.4) by the introduction of a comoving frame K* as in Section A.2.2. Below, we treat the problem from the lab. frame, analogously to the methcd in paragraph A.3.

A.5.1. The equation of motion

Firstly, Newton's law must be integrated. Taking (Fig. A.5.1)

$$\vec{B}(z) = \hat{y}\, B_o \cos \frac{2\pi z}{\lambda_w} \quad , \quad 0 < z < N \cdot \lambda_w$$

and zero elsewhere, this becomes

$$(-e) \cdot \frac{\vec{dr}_p}{dt'} \times \vec{B} = \frac{d}{dt'} \left(m\gamma \frac{\vec{dr}_p}{dt'}\right) = m\gamma \frac{d^2}{dt'^2} \vec{r}_p(t') \; ;$$

$$\ddot{x} = -\frac{eB_o}{m\gamma} \cdot \dot{z} \cos \frac{2\pi z}{\lambda_w} \quad ,$$

$$\ddot{z} = -\frac{eB_o}{m\gamma} \cdot \dot{x} \cos \frac{2\pi z}{\lambda_w} \quad , \quad 0 < z < N \cdot \lambda_w \qquad \text{(A.5.1)}$$

We have used the concept that as the field does no work, the normalized energy γ is constant. At $t' = 0$, the electron is incident on the ondulator with velocity $\dot{x} = 0$, $\dot{z} = c\beta$ (see Fig. A.5.1). The general character of the movement is obvious: The electron will drift down the ondulator with a mean velocity $c\beta^*$ and wiggle around this mean path. Thus we put

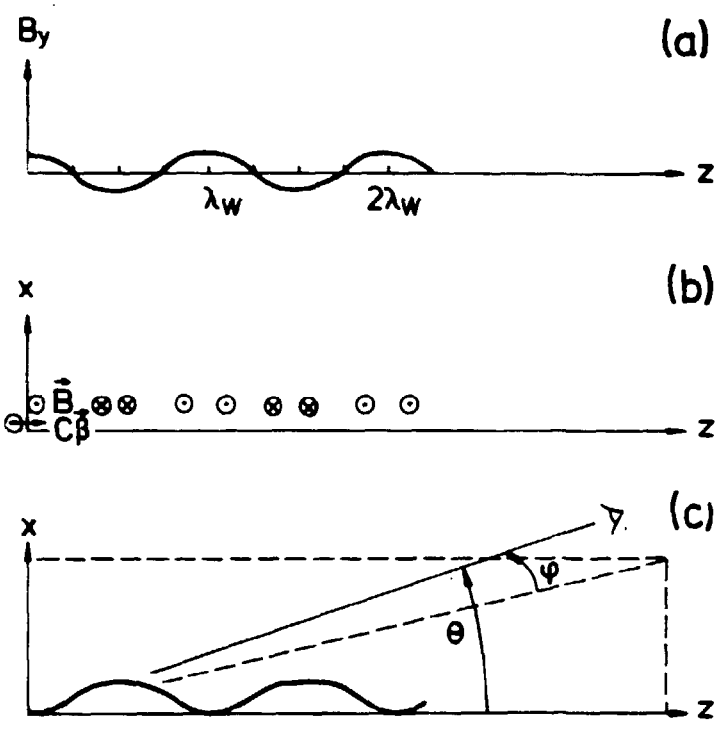

Fig. A.5.a.
a: Variation of the magnetic field.
b: Scenario at t' = 0.
c: Definition of angles θ,φ.

$$x = f_x(t') \quad , \quad z = c\beta^* t' + f_z(t') \; , \tag{A.5.2}$$

where the f's and their derivatives are small, and in particular,

$$\langle \dot{f}_x \rangle = \langle \dot{f}_z \rangle = 0 \; . \tag{A.5.3}$$

Substituting (A.5.2) in (A.5.1) and taking lowest orders of the f's we get for f_x, using the initial values $f_x(0) = 0$, $\dot{f}_x(0) = 0$ and (A.5.3):

$$\ddot{f}_x = \frac{eB_o}{m\gamma}\, c\beta^* \cos\frac{2\pi c\beta^* t'}{\lambda_w} \quad ;$$

$$\dot{f}_x = \frac{eB_o}{m\gamma}\,\frac{\lambda_w}{2\pi}\sin\frac{2\pi c\beta^* t'}{\lambda_w} = c\cdot\frac{K}{\gamma}\sin\frac{2\pi c\beta^* t'}{\lambda_w} \qquad \text{(A.5.4)}$$

$$f_x = -\frac{K}{\beta^*\gamma}\,\frac{\lambda_w}{2\pi}\left(\cos\frac{2\pi c\beta^* t'}{\lambda_w} - 1\right) ,$$

where

$$K \equiv \frac{eB_o c}{mc^2}\,\frac{\lambda_w}{2\pi} = 93\cdot(B_o/T)\cdot(\lambda_w/m)$$

$$K/\gamma = 0.048\cdot(B_o/T)\cdot(\lambda_w/m)\cdot(E_e/GeV)^{-1} . \qquad \text{(A.5.5)}$$

For f_z we get in the same way

$$\ddot{f}_z = -\frac{eB_o}{m\gamma}\,\dot{f}_x\cos\frac{2\pi c\beta^* t'}{\lambda_w} = -\frac{1}{2}\left(\frac{K}{\gamma}\right)^2 c^2\,\frac{2\pi}{\lambda_w}\sin 2\,\frac{2\pi c\beta^* t'}{\lambda_w}$$

$$\dot{f}_z = \frac{1}{4}\left(\frac{K}{\gamma}\right)^2\frac{c}{\beta^*}\cos 2\,\frac{2\pi c\beta^* t'}{\lambda_w}\;(+\,\delta v_o) \qquad \text{(A.5.6)}$$

$$f_z = \frac{1}{8}\left(\frac{K}{\gamma}\right)^2\frac{\lambda_w}{2\pi}(\beta^*)^{-2}\sin 2\,\frac{2\pi c\beta^* t'}{\lambda_w}$$

By (A.5.3), $\delta v_o = 0$, and the condition $\dot{z}(o) = c\beta$ then determines β^*:

$$\beta^* = \beta - \frac{1}{4}\left(\frac{K}{\gamma}\right)^2(\beta^*)^{-1} \approx \beta - \frac{1}{4}\left(\frac{K}{\gamma}\right)^2 ,$$

$$\gamma^* \equiv (1-(\beta^*)^2)^{-1/2} \cong \gamma/\sqrt{1+\frac{1}{2}K^2} , \qquad \text{(A.5.7)}$$

to lowest order in (K/γ). In the same approximation, energy is conserved by this solution:

$$\dot{x}^2 + \dot{z}^2 = \dot{f}_x^2 + (c\beta^* + \dot{f}_z)^2$$

$$\equiv (\beta^* c)^2 + \dot{f}_x^2 + 2\, c\beta^*\, \dot{f}_z$$

$$= c^2 \left\{ (\beta^*)^2 + \frac{1}{2} \left(\frac{K}{\gamma}\right)^2 \right.$$

$$\left. + \left(\frac{K}{\gamma}\right)^2 (1 - \beta^*) \left(\sin^2 \left(\frac{2\pi c\beta^* t'}{\lambda_w}\right) - 1/2\right) \right\}$$

$$= (c\beta)^2 \,,$$

plus terms higher than $(K/\gamma)^2$. The solution describes a uniform movement $c\beta^* t'$ and superimposed on this the (f_x, f_z)-movement describing a figure-eight of

$$\text{half-height } a = \frac{K}{\gamma} \frac{\lambda_w}{2\pi} \,, \qquad \text{(A.5.8)}$$

$$\text{half-width } w = \frac{1}{8} \left(\frac{K}{\gamma}\right)^2 \frac{\lambda_w}{2\pi} \,, \quad w/a = \frac{1}{8} \left(\frac{K}{\gamma}\right) .$$

(See Fig. A.5.2a). The figure-eight arises because the transverse motion takes energy away from the longitudinal motion, reducing the average velocity to $c\beta^*$ and making the z-velocity oscillate around this value.

The comoving frame K* of Purcell (Ref. A.6, 1977) moves with constant velocity $\hat{z}c\beta^*$ with respect to the lab. frame K, thus keeping up with the electron *on the average*. A Lorentz transformation (as in Section A.2.2) yields the motion as seen from K*. The electron describes a figure-eight (see Fig. A.5.2b) of

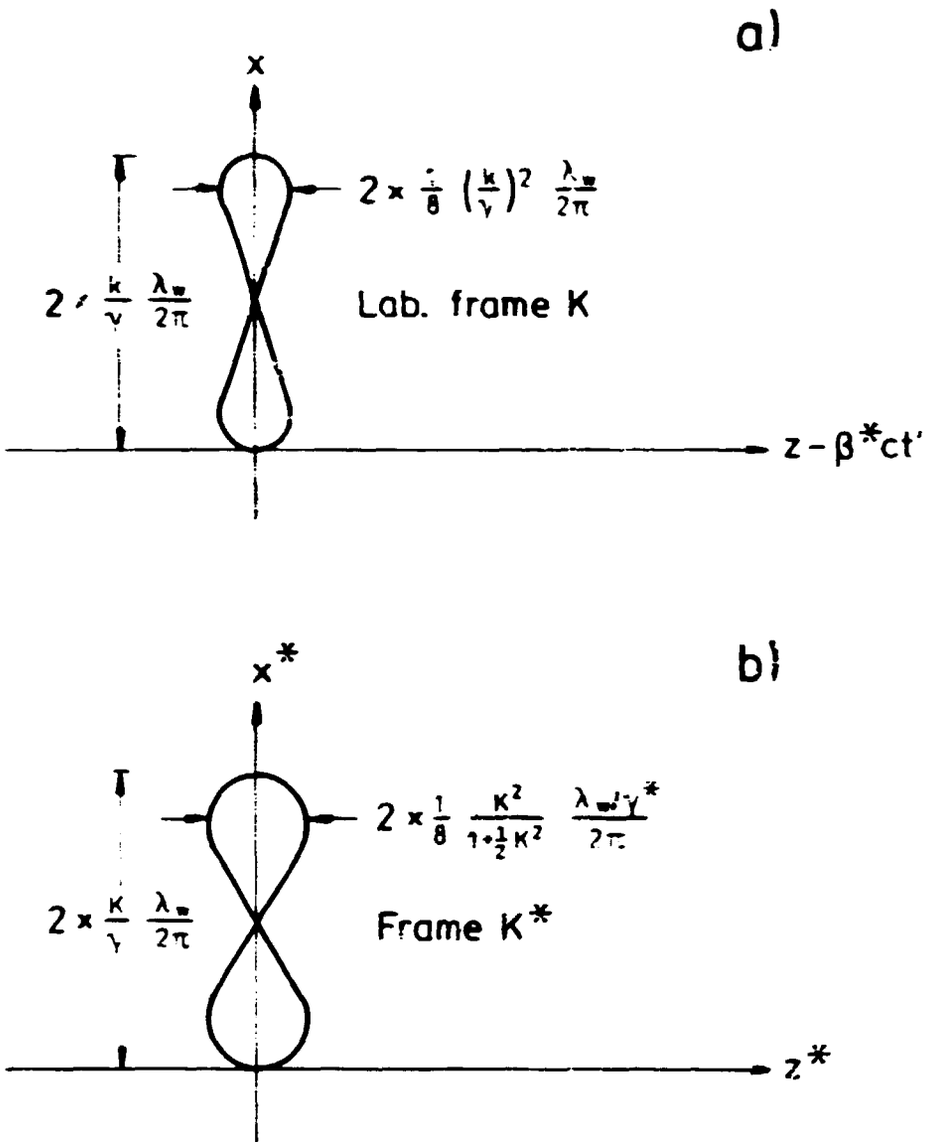

Fig. A.5.2. The motion of the electron in the ondulator,
a: As seen from the laboratory.
b: As seen from the comoving frame K*.

$$\text{half-height } a^* = \frac{K}{\gamma} \frac{\lambda_w}{2\pi} = a \ ,$$

$$\text{half-width } \quad w^* = \gamma^* \cdot w = \frac{1}{8} \frac{K^2}{1 + \frac{1}{2} K^2} \frac{\lambda_w/\gamma^*}{2\pi} \ , \qquad \text{(A.5.9)}$$

$$w^*/a^* = \gamma^* \cdot (w/a) = \frac{1}{8} K / \sqrt{1 + \frac{1}{2} K^2} \ .$$

Of course, a Lorentz contraction of (A.5.9) gives (A.5.8). For $K << 1$ the particle oscillates in K* like a Hertz dipole, giving the desired monochromatic radiation. Going back to the Lab. frame, the maximum deflection angle is seen to be

$$\psi_o = K/\gamma \ .$$

Thus the condition $K << 1$ for no harmonics is also the condition for "short" bending magnets. (And $K << 1$ means that the transverse motion is non-relativistic). We shall restrict the calculations to this case.

A.5.2. The radiation from a weak-field sinusoidal ondulator

The problem is treated in a manner analogous to the treatment of the synchrotron radiation. However, as the motion is linear, the calculations are simpler.

The motion of the electron is

$$\vec{r}_p(t') = \hat{x}\, a\, (1 - \cos \omega_o t') + \hat{z}\, c\beta^* t' \ ,$$

$$\vec{\beta}(t') = \hat{x}\, \frac{K}{\gamma} \sin \omega_o t' + \hat{z}\, \beta^* \ ,$$

$$\dot{\vec{\beta}}(t') = \hat{x}\, \frac{K}{\gamma}\, \omega_o \cos\omega_o t' \ ,$$

$$a \equiv \frac{K}{\gamma}\frac{\lambda_w}{2\pi} = \frac{eB_o c}{mc^2}\left(\frac{\lambda_w}{2\pi}\right)^2 \ ,$$

$$\omega_o \equiv \frac{2\pi c}{\lambda_w} \ .$$

The *observer* is at a (large) distance r_o, at angle ϑ from the z-axis and angle ϕ from the x-z-plane. Thus, (θ, ϕ) are the usual polar coordinates. The *unit vector* is then

$$\hat{n} = \hat{x}\sin\vartheta\cos\varphi + \hat{y}\sin\vartheta\sin\varphi + \hat{z}\cos\vartheta$$

$$\equiv \hat{z}\, n_x + \hat{y}\, n_y + \hat{z}\, n_z \ .$$

and is constant for a distant observer. The *distance* is

$$R(t') = r_o - \hat{n}\cdot\vec{r}_p(t')$$

$$= r_o - n_z \cdot c\beta^* t'$$

$$= r_o \ ,$$

the *retarded time* is

$$t = r_o/c + t'(1 - \beta^* n_z) = r_o/c + \kappa t' \qquad \text{(A.5.10)}$$

and the "*slope*" is

$$\kappa = 1 - \hat{n}\cdot\vec{\beta} = 1 - n_z\beta^* = \frac{1+(\gamma^*\vartheta)^2}{2(\gamma^*)^2} \ . \qquad \text{(A.5.11)}$$

We need also to calculate the vector $\vec{\alpha}$ of (A.2.3). We use the unit vectors $\hat{n}$ (longitudinal),

$$\hat{\varepsilon}_{||} = \frac{\hat{x}-(\hat{x}\cdot\hat{n})\hat{n}}{\sqrt{1-(\hat{x}\cdot\hat{n})^2}} = \frac{\hat{n}\times(\hat{x}\times\hat{n})}{\sqrt{1-n_x^2}} \ , \quad \text{and}$$

$$\hat{\varepsilon}_{\perp} = \hat{n}\times\hat{\varepsilon}_{||} = \frac{\hat{n}\times\hat{x}}{\sqrt{1-n_x^2}} \ ,$$

analogous to the ones used in § A.3. $\hat{\varepsilon}_{||}$ is almost parallel - and $\hat{\varepsilon}_{\perp}$ is perpendicular - to the acceleration. Of course, $\hat{n}\cdot\vec{\alpha} = 0$, and the remaining components after some calculations become:

$$\vec{\alpha}(t') = \frac{K}{\gamma}\,\omega_o\cos\omega_o t'\cdot\vec{\alpha}_o \ , \qquad \text{(A.5.12)}$$

$$\hat{\varepsilon}_{||} \cdot \hat{\alpha}_o = \frac{-n_y^2 - n_z(n_z-\beta^*)}{\sqrt{1-n_x^2}} = -\frac{1}{2\gamma^{*2}}\left\{1+(\gamma^*\vartheta)^2(1-2\cos^2\phi)\right\},$$

$$\hat{\varepsilon}_{\perp} \cdot \hat{\alpha}_o = n_x n_y \beta^*/\sqrt{1-n_x^2} = \frac{1}{2\gamma^{*2}}\left\{2(\gamma^*\vartheta)^2 \cos\phi \sin\phi\right\}. \qquad (A.5.13)$$

Inserting (A.5.10) in (A.5.12), the time dependence becomes

$$\cos\omega_o t' = \cos\left\{\omega_1(\vartheta) \cdot (t - r_o/c)\right\},$$

$$\omega_1(\vartheta) = \omega_o/< = \omega_o \cdot 2(\gamma^*)^2/(1 + (\gamma^*\vartheta)^2), \qquad (A.5.13')$$

and according to (A.2.2) either component of the electric field is

$$\hat{\varepsilon} \cdot \vec{E}(\vec{r}_o,t) = \frac{-e}{4\pi\sqrt{\varepsilon_o/\mu_o}\, r_o} \cdot (\hat{\varepsilon} \cdot \hat{\alpha}_o) \cdot \frac{\frac{K}{\gamma}\omega_o \cos\omega_1(t-r_o/c)}{\left(\frac{1}{2\gamma^{*2}}\left(1+(\gamma^*\vartheta)^2\right)\right)^3},$$

$$\begin{pmatrix} \hat{\varepsilon}_{||} \\ \\ \hat{\varepsilon}_{\perp} \end{pmatrix} \cdot \vec{E}(\vec{r}_o,t) =$$

$$\frac{-e\omega_o}{4\pi\sqrt{\varepsilon_o/\mu_o}\, r_o} \frac{K}{\sqrt{1+\frac{1}{2}K^2}} \frac{4(\gamma^*)^3 \cos\omega_1(t-r_o/c)}{\left(1+(\gamma^*\vartheta)^2\right)^3} \cdot \begin{pmatrix} -\left(1+(\gamma^*\vartheta)^2(1-2\cos^2\phi)\right) \\ \\ 2(\gamma^*\vartheta)^2 \cos\phi \sin\phi \end{pmatrix}$$

A Fourier transformation

$$\vec{E}(\omega) = \frac{1}{\sqrt{2\pi}} \int_{r_o/c}^{(r_o/c) + < \frac{N\lambda_w}{c}} e^{i\omega t} \cdot \vec{E}(t)dt$$

gives

$$\begin{pmatrix} \hat{\varepsilon}_{\parallel} \\ \\ \hat{\varepsilon}_{\perp} \end{pmatrix} \cdot \vec{E}(\omega) =$$

$$\frac{-e\omega_o}{4\pi\sqrt{2\pi}\sqrt{\varepsilon_o/\mu_o}\, r_o} \frac{K}{\sqrt{1+\frac{1}{2}K^2}} \frac{4(\gamma^*)^3}{(1+(\gamma^*\theta)^2)^3} \cdot \begin{pmatrix} (-(1+(\gamma^*\theta)^2(1-2\cos^2\phi)) \cdot \\ (\\ (\\ (2(\gamma^*\theta)^2 \cos\phi \sin\phi \end{pmatrix} \cdot$$

$$\cdot e^{i\omega r_o/c} \left\{ e^{i\frac{\omega+\omega_1}{\omega_1}N\pi} \cdot \frac{\sin\frac{\omega+\omega_1}{\omega_1}N\pi}{\omega+\omega_1} + e^{i\frac{\omega-\omega_1}{\omega_1}N\pi} \cdot \frac{\sin\frac{\omega-\omega_1}{\omega_1}N\pi}{\omega-\omega_1} \right\} \qquad (A.5.14)$$

It is seen that, the two components being in phase, the radiation is linearly polarized for all directions and frequencies. The polarization is along $\hat{\varepsilon}_{\parallel}$ for the special directions $\theta = 0$, $(\theta,\phi) = (\theta,0)$ and $(\theta, \pi/2)$, as can be understood from the symmetry; and along $(\hat{\varepsilon}_{\parallel} \pm \hat{\varepsilon}_{\perp})$ for the directions $(\theta,\phi) = (1/\gamma, \pm \pi/4)$. Restricting attention to positive frequencies, we ignore in (A.5.14) the term which is large only for $\omega \approx -\omega_1$. Defining the function

$$\Delta_N(\hbar\omega-\hbar\omega_1) \equiv \frac{N}{\hbar\omega_1} \left[\frac{\sin N\pi \cdot \frac{\hbar\omega-\hbar\omega_1}{\hbar\omega_1}}{N\pi \cdot \frac{\hbar\omega-\hbar\omega_1}{\hbar\omega_1}} \right]^2 ,$$

$$\int \Delta_N(\hbar\omega-\hbar\omega)d(\hbar\omega_1) = 1 \ , \ \Delta_N(\hbar\omega-\hbar\omega_1) \to \delta(\hbar\omega-\hbar\omega_1) \text{ as } N \to \infty \ ,$$

of width

$$\Delta(\hbar\omega) \approx \hbar\omega_1/N \ ,$$

the spectral brightness (energy per absolute bandwidth per steradian per electron) becomes

$$\frac{d\varepsilon}{d\Omega\ d\hbar\omega} = \frac{2\ r_o^2}{\hbar c \mu_o} |\vec{E}(\omega)|^2 = \frac{d\varepsilon}{d\Omega} \cdot \Delta_N(\hbar\omega - \hbar\omega_1(\theta)) \ , \qquad \text{(A.5.15)}$$

where

$$\frac{d\varepsilon}{d\Omega} = N \cdot \frac{e^2}{4\pi\varepsilon_o} \cdot \frac{K^2}{(1+\frac{1}{2}K^2)^3} \gamma^4 \cdot \frac{4\pi}{\lambda_w} (1+(\gamma^*\theta)^2)^{-5} \ .$$

$$\cdot \begin{cases} (1+2(\gamma^*\theta)^2(1-2\cos^2\phi+(\gamma^*\theta)^4(1-2\cos^2\phi)^2 & (\|) \\ (4(\gamma^*\theta)^4\cos^2\theta \sin^2\phi & (\perp) \\ \dfrac{}{(1+2(\gamma^*\theta)^2(1-2\cos^2\phi)+(\gamma^*\theta)^4} & \text{(total)}. \end{cases}$$

The total energy in the solution is

$$\varepsilon_{e1} = \int_0^\infty d(\hbar\omega) \int_{4\pi} d\Omega \frac{d\varepsilon}{d\Omega\ d\hbar\omega} = \left(\frac{1}{\gamma^*}\right)^2 \int_0^{2\pi} d\phi \int_0^\infty (\gamma^*\theta) d(\gamma^*\theta) \cdot \frac{d\varepsilon}{d\Omega} \ ,$$

$$\varepsilon_{e1} = N \cdot \frac{4\pi^2}{3} \frac{e^2\gamma^2}{4\pi\varepsilon_o} \frac{1}{\lambda_w} \cdot \frac{K^2}{(1+\frac{1}{2}K^2)^2} \cdot \begin{cases} 7/8 & (\|) \\ 1/8 & (\perp) \\ 1 & \text{(total)} \end{cases}$$

From general considerations, using (A.2.13), the energy must be

$$\frac{N\lambda_w}{c} \cdot \frac{2}{3} \frac{e^2\gamma^4}{4\pi\varepsilon_o c} \langle(\dot{\beta}_\perp)^2\rangle \ ,$$

$$\langle(\dot{\beta}_\perp)^2\rangle = \frac{1}{2}\left(\frac{K}{\gamma}\right)^2 \omega_o^2 = \frac{e^2c^2}{(mc^2)^2\gamma^2} c^2 \cdot \frac{1}{2} B_o^2 = \frac{e^2c^4}{(E_e)^2} \cdot \langle B^2\rangle \ ,$$

$$\varepsilon_e = N \frac{4\pi^2}{3} \frac{e^2\gamma^2}{4\pi\varepsilon_o} \frac{K^2}{\lambda_w} = N\lambda_w \cdot \frac{2}{3} r_e \frac{\gamma^2 e^2 c^2}{mc^2} \langle B^2\rangle \qquad \text{(A.5.16)}$$

Thus

$$\varepsilon_{e1} = \varepsilon_e/(1 + \frac{1}{2} K^2)^2 \ .$$

As Hofmann (Ref. A.4, 1980) remarks, a more rigorous treatment will probably show the lacking energy to be found in the higher harmonics, and in our approximation, $K \ll 1$, the difference is negligible.

The power for current I becomes

$$P_I = \frac{2}{3} \frac{r_e e c^2 \gamma^2}{mc^2} \langle B^2 \rangle \cdot I \cdot N\lambda_w \qquad (A.5.17)$$

as in (A.3.9'). We express the remaining quantities in terms of the power in the 1st harmonic:

$$P_{I1} = P_I/(1 + \frac{1}{2} K^2)^2 \ . \qquad (A.5.18)$$

$$P_{||} = (7/8)\ P_{I1} \quad , \quad P_\perp = (1/8)\ P_{I1} \ , \qquad (A.5.19)$$

$$\frac{dP}{d\Omega} = P_{I1} \cdot \frac{3\gamma^{*2}}{\pi} \cdot \frac{1}{(1+(\gamma^*\theta)^2)^5} \ \cdot$$

$$\cdot \left(\frac{\begin{matrix} (1+2(\gamma^*\theta)^2(1-2\cos^2\phi)+(\gamma^*\theta)^4(1-2\cos^2\phi)^2 & (||) \\ (4(\gamma^*\theta)^4\cos^2\phi\ \sin^2\phi & (\perp) \end{matrix}}{1+2(\gamma^*\theta)^2(1-2\cos^2\phi)+(\gamma^*\theta)^4} \right. \quad \begin{matrix} \\ \\ \left. \right) \ (\text{total}) \end{matrix}$$

$$\frac{dP}{d\Omega\ d\hbar\omega} = \frac{dP/\hbar\omega}{d\Omega\ d(\ln\hbar\omega)} = \frac{dP}{d\Omega} \times \Delta_N(\hbar\omega - \hbar\omega_1(\theta)) \qquad (A.5.21)$$

The (angle integrated) spectrum might also be of interest. The case $N \to \infty$ is simple and gives the result

$$\frac{dP}{d\hbar\omega} = \frac{dP/\hbar\omega}{d(\ln\hbar\omega)} = \frac{3P_{I1}}{\hbar\omega_1(o)} \cdot$$

$$\cdot \begin{pmatrix} \frac{3}{2}\left(\frac{\omega}{\omega_1(o)}\right)^3 - \left(\frac{\omega}{\omega_1(o)}\right)^2 + \frac{1}{2}\left(\frac{\omega}{\omega_1(o)}\right) & (\perp\perp) \\ \\ \frac{1}{2}\left(\frac{\omega}{\omega_1(o)}\right)^3 - \left(\frac{\omega}{\omega_1(o)}\right)^2 + \frac{1}{2}\left(\frac{\omega}{\omega_1(o)}\right) & (\perp) \\ \hline \\ 2\left(\frac{\omega}{\omega_1(o)}\right)^3 - 2\left(\frac{\omega}{\omega_1(o)}\right)^2 + \left(\frac{\omega}{\omega_1(o)}\right) & (\text{total}) \end{pmatrix} \qquad (A.5.22)$$

The spectrum is zero beyond the frequency

$$\hbar\omega_1(\theta=0) = \frac{hc \cdot 2\gamma^2}{\lambda_w(1+1/2\ K^2)}$$

In terms of numbers the above formulae give (using $K << 1$).

$$P_I = 1.27\ \text{kW} \cdot \langle\left(\frac{B}{T}\right)^2\rangle \cdot (I/\text{Amps}) \cdot E_e/\text{GeV})^2 \cdot (N\lambda_w/m)\ ,$$

(A.5.17')

$$\left.\frac{dP}{d\Omega}\right|_{\theta=o} = 4.64\ \frac{GW}{\text{sterad}} \cdot \langle(B/T)^2\rangle \cdot (I/A) \cdot (E_e/\text{GeV})^4 \cdot (N\lambda_w/m)$$

(A.5.20')

$$\left.\frac{dP}{d\Omega\ d\hbar\omega}\right|_{\substack{\theta=o \\ \omega=\omega_1(o)}} = \left.\frac{dP/\hbar\omega_1(o)}{d\Omega\ d(\ln\hbar\omega)}\right|_{\substack{\theta=o \\ \omega=\omega_1(o)}} = \frac{N}{\hbar\omega_1} \cdot \frac{3\gamma^{*2}}{\pi} \cdot P_I$$

(A.5.21')

$$= 3.05 \cdot 10^{27}\ \frac{\text{Photons}}{\text{sec}\cdot\text{sterad}} \cdot \langle(B/T)^2\rangle \cdot (I/A) \cdot (E_e/\text{GeV})^2 \cdot$$

$$\cdot\ (N\lambda_w/\text{meters})^2 \quad \text{(per unit relative bandwidth)}\ ,$$

$$\left.\frac{dP}{d\hbar\omega}\right|_{\omega=\omega_1(o)} = \left.\frac{dP/\hbar\omega_1(o)}{d(\ln\hbar\omega)}\right|_{\omega=\omega_1(o)} = \frac{3P_{I1}}{\hbar\omega_1(o)} \qquad \text{(A.5.22')}$$

$$= 2.51\cdot10^{21}\ \frac{\text{Photons}}{\text{second}} \cdot \langle(B/T)^2\rangle \cdot (I/A)\cdot\left(\frac{N\lambda_w}{\text{meters}}\right) \cdot (\lambda_w/\text{meters})$$

(per unit relative bandwidth) .

The power, (A.5.17), of course agrees with (A.3.9'), and since this power is radiated into a cone ($d\Omega \sim 1/\gamma^2$) instead of a sheet ($d\Omega \sim 2\pi/\gamma$), the coefficient in (A.5.20') is much larger than the corresponding (A.3.9'''). Also, comparing (A.5.21') and (A.3.17'), and putting in reasonable numbers it is seen that if the desired wavelength can be reached, and if the interference is not smeared out by imperfect electron beam optics, a much larger spectral brightness is obtained from the ondulator than from the bending magnet.

To conclude the paragraph, the results for the sinusoidal undulator agree in general with the reasoning in § A.4. The reduction of the γ by the factor $(1 + \frac{1}{2} K^2)^{-1/2}$ (Eq. (A.5.7)) was derived, and although the detailed treatment assumed this effect to be negligible, Eq. (A.5.11), being general, shows that the resonance frequency ω_1 and its harmonics can be tuned by varying the magnetic field.

A.6. Conclusion

The theory of synchrotron and ondulator radiation has been reviewed together with the relevant electrodynamics.

One-electron interference effects have been seen to be important for wigglers/ondulators for the ideal electron beams considered.

The question, to which extend this conclusion is modified when beam imperfections are taken into account, has not been addressed. Also, the far field approximations employed may need to be reconsidered: Certainly, for a realistic geometry, the near and far end of an ondulator may be seen (off axis) under different angles, mixing the spectrum up. However, one would not expect to get just the usual smooth synchrotron radiation spectrum from a wiggler with more than a few turns.

To get X-ray wavelengths from the first harmonic of an undulator would seem to be difficult. If strong, non-sinusoidal fields and higher harmonics are used, this, however, may be feasible.

References

A.1. JACKSON, J.D. (1962) Classical electrodynamics. (Wiley, New York) 641 p. (This author defines ω_c differently from us.)

A.2. SCHOTT, O.A. (1912). Electromagnetic radiation p. 109-10 (Cambridge University Press, Cambridge) as cited by Ref. A.3.

A.3. SCHWINGER, J. (1949). Phys. Rev. 75, 1912-25.

A.4. HOFMANN, A. (1980). Phys. Rep. 64, 253-81.

A.5. MOTZ, H. (1977). SSRP Rep. No. 77/05, p. II-162.

A.6. PURCELL, E.M. (1977). SSRP Rep. No. 77/05, p. IV-18.

A.7. SOKOLOV, A.A. and TERNOV, I.M. (1968). Synchrotron Radiation (Akademie-Verlag, Berlin) 202 p.

A.8. BLEWETT, J.P. (Ed.) (1977). Reference Documents for the Proposal for a National Synchrotron Light Source. BNL-50595 Vol. 2.

APPENDIX B

SINGLET-SINGLET MAGNETISM

This appendix develops the theory for a magnet with two singlets as the lowest lying states, these being well isolated from the higher excited states. Section 1 derives the single ion polarisability and Section 2 and 3 are concerned with a mean field description of the paramagnetic and ferromagnetic states. We follow the exposition in Ref. B.1. A review of the literature is given in Ref. B.2.

B.1. Single ion theory

For a single ion in the crystalline electric field (CEF) and in an applied magnetic field H_z, (Fig. B.1) the Schrödinger equation reads

$$(\hat{H}_{CEF} + \hat{H}_Z)\ |n\rangle = E_n\ |n\rangle\ ,\ n = 0,1 \qquad (B.1)$$

where the Zeeman hamiltonian is

$$\hat{H}_Z = -\mu_o g_J \mu_B J_z H_z\ .$$

We take $|0\rangle_c$, $|1\rangle_c$ to be the eigenstates of $\hat{H}_{CEF}$, and use these states as a basis,

$$|n\rangle = |0\rangle_c\ C_{0n} + |1\rangle_c\ C_{1n},\ n = 0,1\ . \qquad (B.2)$$

$\hat{H}_{CEF}$ is diagonal in this basis,

$$\underline{\underline{H}}_{CEF} = \Delta \cdot \begin{pmatrix} -1/2 & 0 \\ 0 & 1/2 \end{pmatrix}\ , \qquad (B.3)$$

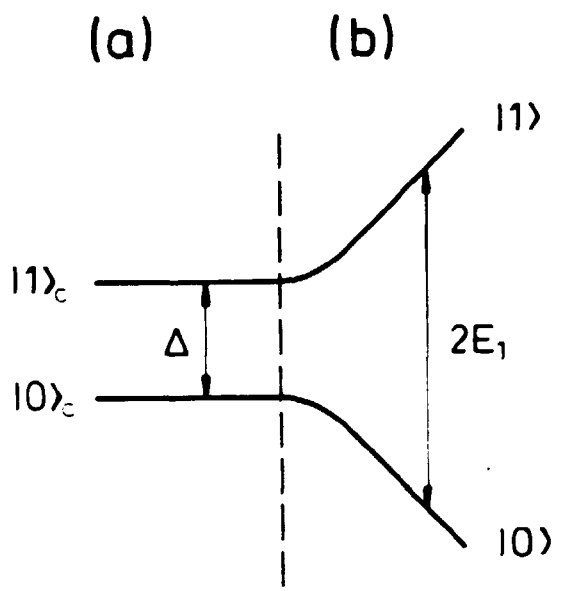

Fig. B.1. Single ion with split ground state in an applied magnetic field $\vec{H}$. a: $\vec{H} = 0$, b: Increasing $\vec{H}$.

The diagonal matrix elements $\langle n|\hat{\vec{J}}|n\rangle_c$ are zero on account of time reversal symmetry. Then, the Zeeman term is

$$\underline{\underline{H}}_Z = - \mu_o \cdot {}_{ss}g \cdot \mu_B \cdot H_z \cdot \begin{pmatrix} 0 & 1/2 \\ 1/2 & 0 \end{pmatrix} , \qquad (B.4)$$

where the g-factor of the two close-lying singlets,

$${}_{ss}g = 2 \langle 1|_c \, g_J \hat{J}_z |0\rangle_c \qquad (B.5)$$

parametrizes the surviving matrix element of $\hat{\vec{J}}$. We note in passing that if we describe the two singlets by an effective spin $s_{eff} = 1/2$,

$$|0\rangle_c = |s_z = +1/2\rangle \quad , \quad |1\rangle_c = |s_z = -1/2\rangle \quad ,$$

it is seen from (B.3) and (B.4) that

$$\hat{H}_{CEF} \propto \hat{s}_z \text{ and } \hat{H}_Z \propto \hat{s}_x \ .$$

Thus, in the s_{eff} formalism we may treat the crystalline electric field as a magnetic field transversal to the real magnetic field $\vec{H}$. However, this idea will not be pursued.

Solving (B.1) we now easily get the energies

$$E_1 = - E_o = ((\frac{\Delta}{2})^2 + E_Z^2)^{1/2}$$

and the perturbed states

$$|0> = \frac{\frac{\Delta}{2} + E_1}{N} |0>_c - \frac{E_Z}{N} |1>_c$$

$$|1> = \frac{E_Z}{N} |0>_c + \frac{\frac{\Delta}{2} + E_1}{N} |1>_c \ ,$$

where

$$E_Z \equiv \frac{1}{2} \mu_o \cdot ss^g \cdot \mu_B \cdot H_z$$

is the Zeemann-only energy, and the denominator

$$N \equiv (2 \cdot E_1 \cdot (\frac{\Delta}{2} + E_1))1/2 \ .$$

[Some authors prefer the rather elegant parametrisation

$$|0> = \cos\phi \ |0>_c - \sin\phi \ |1>_c$$

$$|1> = \sin\phi \ |0>_c + \cos\phi \ |1_c> \ ,$$

where

$$\tan 2\phi = \frac{E_Z}{\Delta/2} \quad .$$

Now we introduce the temperature T. The partition function is

$$Z = 2 \cosh \frac{E_1}{kT}$$

and the induced moment at thermal equilibrium is

$$\langle \mu \rangle = \sum_{n=0,1} \langle n | - g_J \mu_B \hat{J}_z | n \rangle \cdot \frac{e^{-E_n/kT}}{Z}$$

$$= \tanh \frac{E_1}{kT} \cdot \langle 0 | \; g_J \mu_B \hat{J}_z | 0 \rangle \quad ,$$

$$\langle \mu \rangle_{\substack{\text{single} \\ \text{ion}}} = \tanh \frac{E_1}{kT} \cdot \frac{1}{2} \, {}_{ss}g \cdot \mu_B \cdot \frac{E_Z}{E_1} \quad , \qquad \text{(B.6)}$$

where the magnetic field enters through E_Z and E_1. The zero field polarizability of the singlet-singlet ion then is

$${}_{ss}\chi_T^o = \mu_o \frac{({}_{ss}g\mu_B)^2}{4} \frac{\tanh \frac{\Delta/2}{kT}}{\Delta/2} \quad .$$

In the limit $\Delta \to 0$ or $T \to \infty$, this expression gives the usual Curie law

$$\chi_T^o = \mu_o \frac{(g\mu_B)^2}{4kT} \quad ,$$

while the limit $T \to 0$ or $\Delta \to \infty$ gives

$${}_{ss}\chi_o^o = 2 \mu_o \frac{|\langle 1 |_c \; \hat{\mu} \; | 0 \rangle_c|^2}{\Delta} \, ,$$

describing temperature-independent Van Vleck paramagnetism.

B.2. Susceptibility

We next include the interactions between the spins and treat them in the mean-field approximation. A homogenous magnetization $\langle\mu\rangle$ leads to a molecular field $(s/4\pi) \cdot \langle\mu\rangle$, where the molecular field parameter is given here for dipolar interactions, in terms of the lattice sum defined in (3.13) or (3.18). Hence

$$\langle\mu\rangle = {}_{ss}\chi_T^o(H + \frac{s}{4\pi} \cdot \langle\mu\rangle) \quad ;$$

with the result

$$\frac{{}_{ss}\chi_T^o}{\chi_T} = 1 - {}_{ss}\chi_T^o \cdot \frac{s}{4\pi} \quad ;$$

$$\chi_T = \mu_o \frac{({}_{ss}g\mu_B)^2}{4} \frac{1}{\Delta/2} \left(\coth \frac{\Delta/2}{kT} - \frac{k_B\vartheta}{\Delta/2}\right)^{-1} \quad , \qquad (B.7)$$

Here,

$$\theta = \frac{1}{k_B} \cdot \mu_o \cdot \frac{({}_{ss}g\mu_B)^2}{4} \cdot \frac{s}{4\pi}$$

is the Curie-Weiss temperature as defined in (3.12) or (3.19) for the case $\Delta = 0$. Inserting $\Delta = 0$, the familiar Curie-Weiss law is retrieved.

From (B.7) the transition point T_C is determined as the temperature giving infinite susceptibility,

$$\coth \frac{\Delta/2}{kT_C} = \frac{k_B\theta}{\Delta/2} \quad . \qquad (B.8)$$

T_C is depressed below the value θ by a factor which depends critically on the ratio $k_B\vartheta/(\Delta/2)$ (see Fig. B.2). T_C goes to zero as $k_B\vartheta/(\Delta/2)$ approaches one, and for smaller values the system never orders.

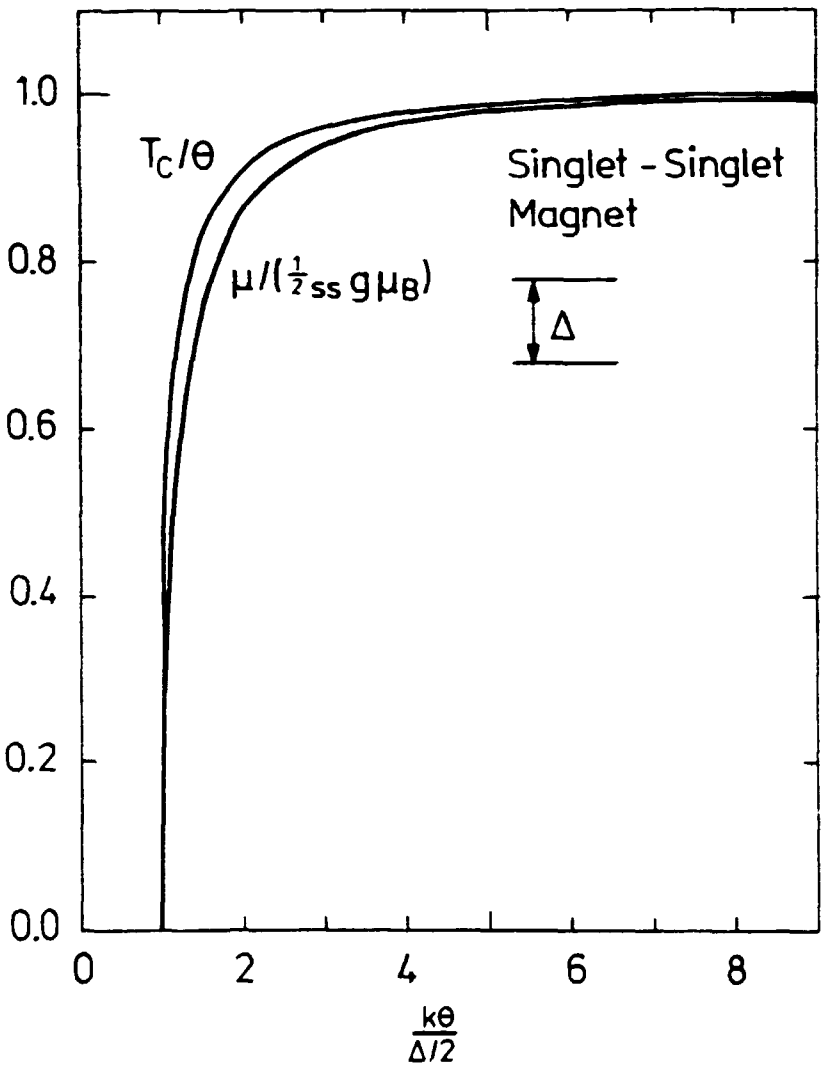

Fig. B.2. As calculated in the mean field approximation, the figure shows the reduced transition point, T_C/θ and reduced zero-temperature magnetic moment, $\mu(T=0)/(1/2\ {}_{ss}g\mu_B)$, versus the ratio between the cooperative and crystal field energies, $k\theta/(\Delta/2)$.

B.3. Spontaneous magnetization

The spontaneous magnetization curve is derived by a self-consistent reasoning well-known from the case of degenerate states. That is, an assumed spontaneous magnetic moment $\langle\mu\rangle_{spont}$ gives rise to a molecular field $(s/4\pi) \cdot \langle\mu\rangle_{spont}$ which in turn must stabilize the assumed moment in accordance with the magnetization curve given in (B.6), i.e.,

$$\langle\mu\rangle_{spont}(T) = \langle\mu\rangle_{\substack{single \\ ion}} \left(H = \frac{s}{4\pi} \cdot \langle\mu\rangle_{spont}, T\right) \quad , \qquad (B.9)$$

Introducing the molecular field in B.6 and defining the scaled magnetization

$$\mu' \equiv \langle\mu\rangle / \left(\frac{1}{2} ss^g \mu_B\right) \quad ,$$

we can cast (B.9) in the form

$$\mu' \cdot \left((\mu')^2 + \left(\frac{\Delta/2}{k\theta}\right)^2\right)^{1/2} \qquad (B.10)$$

$$= \mu' \cdot \tanh\left(\left(\frac{\theta}{T} \cdot (\mu')^2 + \left(\frac{\Delta/2}{k\theta}\right)^2\right)^{1/2}\right)$$

The zero-temperature magnetization is reduced below the value for a true doublet:

$$\langle\mu\rangle_{spont}\ (T=o) = \frac{1}{2} ss^g \mu_B \cdot \left(1 - \left(\frac{\Delta/2}{k\theta}\right)^2\right)^{1/2} \quad , \qquad (B.11)$$

and zero if $k\theta/(\Delta/2)$ is less than one (see Fig. B.2).

For $T \geq T_C$, the transition temperature given in (B.8) above, only $\langle\mu\rangle = 0$ solves Eq. (B.10). Below T_C the stable solution $\mu' \neq 0$ to (B.10) gives the spontaneous magnetization curve. The solution can be found either graphically (Ref. B.1) or simply by choosing μ' and solving for T. Doing so, one arrives at the

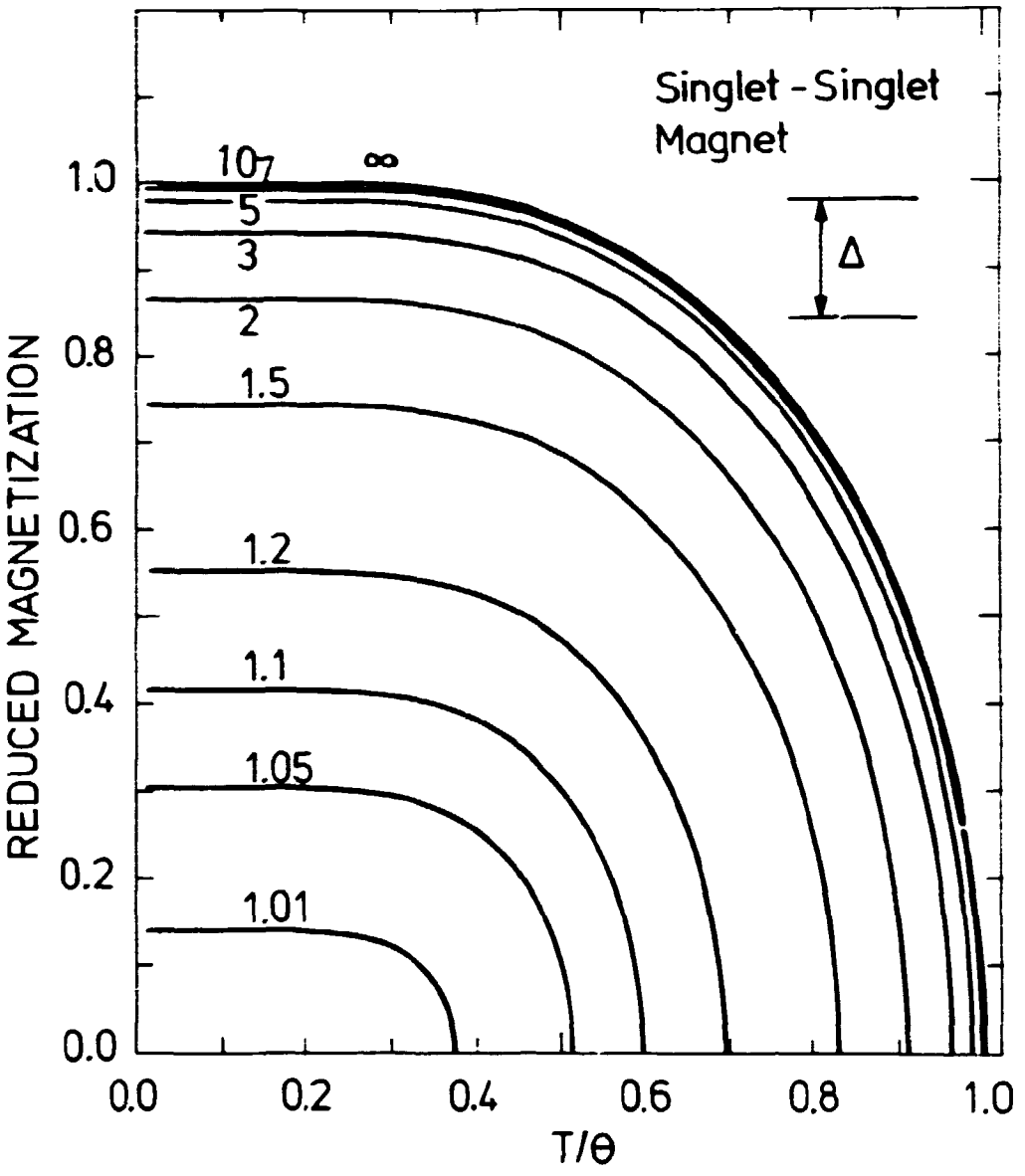

Fig. B.3. Spontaneous magnetization for singlet-singlet magnet. The reduced magnetic moment, $\langle\mu\rangle/(1/2\ g\mu_B)$, as calculated in mean field theory, is plotted versus the reduced temperature T/θ for $\theta/(\Delta/2) = \infty$, 10, 5, 3, 2, 1.5, 1.2, 1.1, 1.05 and 1.01.

magnetization curves shown in Fig. B.3. For $k\theta/(\Delta/2) > 5$, say, the effect of the ground level splitting is seen to be very small.

References

B.1. BLEANEY, B. (1963) Proc. R. Soc. London, Ser. A 276, 19-38.

B.2. BIRGENEAU, R.J. (1973) in: Magnetism and magnetic materials 1972. Edited by C.D. Graham and J.J. Rhyne (American Institute of Physics, New York) vol. 2, p. 1664-88. (AIP Conference Proceedings, 10).

Sales distributors:
G.E.C. Gad Strøget
Vimmelskaftet 32
DK-1161 Copenhagen K, Denmark

Available on exchange from:
Risø Library, Risø National Laboratory,
P.O.Box 49, DK-4000 Roskilde, Denmark

ISBN 87-550-1016-4
ISSN 0106-2840